

THERMOPHYSICAL AND CHEMICAL CHARACTERIZATION OF CHARRING ABLATIVE MATERIALS

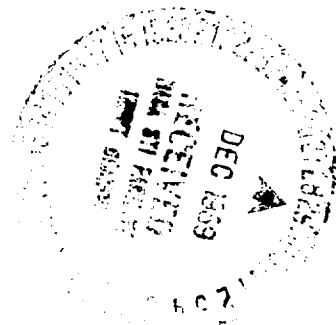
by

J. F. Lagedrost, T. J. Fabish, E. A. Eldridge,
H. W. Deem, and H. H. Krause

prepared for
NATIONAL AERONAUTICS AND SPACE ADMINISTRATION

Contract NAS 7-342

FACILITY FORM 602	N70-14131	
	(ACCESSION NUMBER)	(THRU)
	92	1
	(PAGES)	(CODE)
	CR-73399	33
	(NASA CR OR TMX OR AD NUMBER)	(CATEGORY)



BATTELLE MEMORIAL INSTITUTE
Columbus Laboratories

SUMMARY REPORT

on

THERMOPHYSICAL AND CHEMICAL
CHARACTERIZATION OF CHARRING
ABLATIVE MATERIALS

to

NASA-AMES RESEARCH CENTER

December 31, 1968

by

J. F. Lagedrost, T. J. Fabish, E. A. Eldridge,
H. W. Deem, H. H. Krause, and D. A. Vaughan

Contract NAS 7-342

BATTELLE MEMORIAL INSTITUTE
Columbus Laboratories
505 King Avenue
Columbus, Ohio 43201

June 13, 1969

NASA-Ames Research Center
Gas Dynamics Branch
Moffett Field, California 94035

Attention Dr. John A. Parker

Gentlemen:

NAS 7-342
Final Report

Enclosed are 7 copies and one reproducible copy of the final report on "Thermophysical and Chemical Characterization of Charring Ablative Materials". The approval of this report for distribution completes the program carried out during the period 1965-1968 on the samples of ablative polymer materials supplied by NASA-Ames Research Center.

We were pleased to have been able to work with you on this program, and hope that there will be occasion to do so again in the future.

Very truly yours,

Arthur Levy, Chief
Physical Chemistry and Solid State
Materials Division

AL/dc
Enc. (7 + 1 repro)

cc: NASA-Ames Research Center,
Moffett Field, California 94035
Attention: Mr. Robert Dolan, Contract Administrator

TABLE OF CONTENTS

	<u>Page</u>
INTRODUCTION	1
SUMMARY	1
MATERIALS	2
Composition of Specimens	2
Thermal Stability	5
Anhydride-Cured Epoxy Novolacs	5
Polybenzimidazoles	7
Phenolic-Novolac Nylon	7
Phenolic-Nylon Chars	11
Density	11
THERMOPHYSICAL-PROPERTY MEASUREMENTS	13
Thermal Conductivity	13
Methods and Apparatus	13
Anhydride-Cured Epoxy Novolacs	13
Polybenzimidazoles	15
Phenolic-Novolac Nylons	15
Phenolic-Nylon Chars	18
Influence of Pore Structure on Thermal Conductivity of Polybenzimidazole Char Material	18
X-Ray Diffraction and Electron-Microscope Studies of Phenolic-Nylon Char	20
Enthalpy, Specific Heat	21
Anhydride-Cured Epoxy Novolacs	26
Polybenzimidazoles	28
Phenolic-Novolac Nylons	28
Linear Thermal Expansion	31
Anhydride-Cured Epoxy Novolacs	31
Polybenzimidazoles	31
Phenolic-Novolac Nylons	33
Thermal Diffusivity	33
Calculated Thermal-Diffusivity Values	33
Measured Thermal Diffusivity of PNHD-Hughes No. 5 Precharred at 400 C	35

APPENDIX A

THERMAL CONDUCTIVITY MEASUREMENTS	A-1
---	-----

APPENDIX B

EFFECTS OF POROSITY ON THE THERMAL CONDUCTIVITY OF A POLYBENZIMIDAZOLE CHAR MATERIAL	B-1
---	-----

TABLE OF CONTENTS
(Continued)

	<u>Page</u>
APPENDIX C	
ENTHALPY MEASUREMENTS FOR USE IN CALCULATING SPECIFIC HEAT	C-1
APPENDIX D	
LINEAR-THERMAL-EXPANSION MEASUREMENTS	D-1
APPENDIX E	
APPARATUS AND METHODS FOR MAKING THERMOPHYSICAL-PROPERTY MEASUREMENTS	E-1

THERMOPHYSICAL AND CHEMICAL CHARACTERIZATION OF CHARRING ABLATIVE MATERIALS

by

J. F. Lagedrost, T. J. Fabish, E. A. Eldridge,
H. W. Deem, H. H. Krause, and D. A. Vaughan

INTRODUCTION

Ablation is a complex set of phenomena in which heat is transferred to a specimen and absorbed within the structure, dependent upon the physical and chemical properties of the specimen. It is, therefore, important that the various thermal and chemical properties of ablative materials be known, in order to set up a model of the ablation process and to predict quantitatively the behavior of the material.

Attempts have been made to evaluate the behavior of ablative materials by subjecting them to natural or artificially induced reentry conditions. Such evaluations have left questions unanswered that would be helpful in predicting the behavior of other ablative materials. Another approach to a study of the ablative process is to measure separately the various factors entering into the process and to predict total behavior by properly combining the individual properties. The work described in this report was directed toward this second approach, through the measurement of the thermophysical and chemical properties of model virgin polymeric materials, composites, and preformed chars.

This report summarizes the results obtained during the period 1965-1968 and concludes work on the program.

SUMMARY

Thermophysical-property measurements were made on anhydride-cured epoxy novolac, polybenzimidazole, phenolic-novolac nylon, and charred phenolic-nylon materials. These materials were measured in virgin or preformed char conditions. Most of the materials measured were composites containing density-lowering components such as chopped glass (silica) fibers and glass microballoons.

Properties measured comprised thermal conductivity, enthalpy, and expansion. From these properties, specific heat, thermal diffusivity, and density were calculated. Some pyrolysis studies were made preliminary to the thermophysical-property measurements to facilitate proper handling of the specimens and to assist in the interpretation and evaluation of the measurements.

Thermal conductivities were measured in argon, helium, and vacuum atmospheres. The conductivities of materials with porous phases permeable to gas, such as the polybenzimidazoles and phenolic-novolac nylons, were influenced significantly by the gas in

which the specimens were measured. A study of the influence of pore structure on conductivity showed a quantitative agreement of total porosity (when pores are large enough in diameter to support helium-gas conduction) with conductivity.

Thermal conductivities ranged from about 0.9 to 4 mw/(cm)(C) at 100 C and from 1.2 to 5 mw/(cm)(C) at 400 C. Specific heats ranged from 0.15 to 0.3 cal/(g)(C) at 0 C and from 0.3 to 0.7 cal/(g)(C) at 250 C. Expansions from room temperature to 300 C ranged from about 0.1 to over 3 percent. Calculated thermal diffusivities ranged from about 0.8 to 2.8×10^3 cm²/sec at 200 C. Table 1 shows a breakdown of materials measured, temperature ranges and ranges of thermophysical properties.

From the viewpoint of classes of materials, the epoxy novolacs had the highest thermal conductivities and thermal expansions. The polybenzimidazoles had the highest thermal diffusivities, while the phenolic nylons had the highest specific heats. The ranking of these materials with respect to the thermophysical properties measured is shown below.

	<u>Epoxy Novolacs</u>	<u>Polybenzimidazoles</u>	<u>Phenolic Nylons</u>
Thermal Conductivity	High	Medium	Low
Thermal Diffusivity	Medium	High	Low
Specific Heat	Medium	Low	High
Thermal Expansion	High	Low	Medium

On the basis of arc-imaging furnace experiments performed at NASA-Ames, the ablative performance of epoxy novolacs containing chopped glass fibers was rated good. Thus it appears that medium-to-high values of these thermophysical properties are important for charring ablative polymer materials.

MATERIALS

H. H. Krause

The materials studied during this program were supplied by the NASA-Ames Research Center. They were based on three types of polymers: (1) anhydride-cured epoxy novolacs, (2) polybenzimidazoles, and (3) hexa-cured phenolic novolacs. The actual specimens were composites formed by combinations of the above resins with appropriate vapor-producing and density-lowering materials.

Composition of Specimens

The compositions of the specimens used in this program are shown in Table 2. The anhydride-cured epoxy-novolac resins, designated by the Dow Chemical Company as DEN-438, were studied as the virgin polymer and as composites containing either chopped glass fibers or glass microballons.

TABLE 1. SUMMARY OF THERMOPHYSICAL MEASUREMENTS ON ABLATIVE POLYMER MATERIALS

	Thermal Conductivity, mw/(cm)(C)	Heat Capacity, cal/(g)(C)	Linear Thermal Expansion, percent	Density, g/cc	Thermal Diffusivity, $10^3 \text{ cm}^2/\text{sec}$	Thermal Stability, Incipient Degradation Temperature, C (Vacuum)
Anhydride-Cured Epoxy Novolacs	(50-350 C)	(0-350 C)	(25-300 C)	(20-300 C)	(50-350 C)	--
DEN-438	2.2-2.0	0.28-0.56	3.2	1.24-1.13	1.3-0.8	350
DEN-438 + chopped glass	2.2-2.8	0.26-0.57	3.2	1.33-1.20	1.5-1.0	350
DEN-438 + glass microballoons	1.5	0.23-0.48	1.6	0.61-0.58	2.1-0.9	350
Polybenzimidazoles	(50-500 C)	(0-500 C)	(25-500 C)	(20-400 C)	(50-400 C)	--
DXH-31	1.5-1.3	0.26-0.46	0.5	0.50-0.49	2.3-1.6	550
DXH-32 (pyrolyzed at 650 C)	1.5-2.0	0.14-0.34	0.1	0.50	3.1	--
EXEH-31	0.8-1.3	0.11-0.45	0.8	0.50-0.47	1.4	--
Phenolic Nylons	(25-250 C)	(0-250 C)	(25-300 C)	(20-300 C)	(50-250 C)	--
PNHD-Hughes No. 4	1.0-1.1	0.24-0.71	1.5	0.52-0.49	1.4-0.6	400
PNHD-Hughes No. 5	1.4-1.0	0.24-0.62	1.4	0.56-0.53	1.4-2.2	--
PNLD-Langley	0.8-1.2	0.21-0.65	1.1	0.55-0.52	1.0-0.7	350
PNHD-Hughes No. 5 (pyrolyzed at 400 C)	0.8-2.0 (400 C)	0.26-0.58 (400 C)	1.3	--	1.4-2.2 (400 C)	--
Phenolic-Nylon Chars	(50-500 C)	--	--	--	--	500
NA-12	2.2-3.5	--	--	--	--	800
NA-13	3.6-5.3	--	--	--	--	800
NA-14	3.5-5.0	--	--	--	--	800
NA-15	2.7-4.3	--	--	--	--	500

TABLE 2. COMPOSITION OF MATERIALS

Components	Specimen Composition, weight percent			
	DEN-438	DEN-438 + Chopped Glass	DEN-438 + Glass Microballoons	
<u>Epoxy Novolacs, Anhydride Cured</u> (Dow Chemical Co.)				
Epoxy novolac	53.6	45.6	53.6	
Nadic methyl anhydride	45.6	38.7	45.6	Resin
DMP-30 catalyst	0.8	0.7	0.8	composition
Chopped glass(a)	--	15.0	--	
Glass microballoons	--	--	Undetermined	
<u>Polybenzimidazoles</u> (NARMCO Division, Whittaker Corp.)				
PBI (I-2801, unadvanced)	DXH-30	DXH-31	DXH-32(b)	EXEH-31
Silica microballoons (Eccospheres S1)	65	65	65	65
Alumina - silica fibers (Kaowool)	20	20	20	--
Phenolic microballoons	15	15	15	15
	--	--	--	20
<u>Phenolic - Novolac Nylons</u> (Hughes Aircraft and Langley Research Center)				
	PNHD-Hughes No. 4	PNHD-Hughes No. 5	PNLD-Langley	
Phenolic novolac resin	37	37	25	
Nylon (6-6)	40	40	40	
Phenolic microspheres	23	23	35	
<u>Phenolic Nylon Chars</u> (NASA-Ames)				
	NA-12, -13, -14, -15	PNHD-Hughes No. 5		
Phenolic novolac resin	25	37	Charred	
Nylon (6-6)	40	40	at	
Phenolic microspheres	35	23	1000 C	

(a) 1/32 inch hammer-milled glass fibers.

(b) Specimens pyrolyzed at 650 C.

All of the polybenzimidazole specimens, which were manufactured by the NARMCO Division of the Whittaker Corporation, were filled polymers. These composites all contained alumina-silica fibers (Kaowool) and either silica or phenolic microballons. The series of specimens designated as DXH-32 had been pyrolyzed at 650 C prior to delivery.

The hexa-cured phenolic-novolac resins were made into composites with Nylon 6-6 and phenolic microspheres. Specimens of relatively high density, containing more resin and less of the microspheres, were prepared by the Hughes Aircraft Corporation, and specimens of relatively low density, containing a large amount of microspheres, were supplied by the Langley Research Center.

A fourth type of specimen constituted char samples which were pyrolyzed at NASA-Ames Research Center. These specimens included several low-density phenolic-nylon composites which had been heated to 1000 C via different cycles and one high-density phenolic nylon which was charred to 400 C.

Thermal Stability

In order to assist in the interpretation of the thermophysical-property data, some knowledge of the decomposition behavior of the specimens was necessary. In addition, it was important to determine the extent of pressure buildup that would occur in the encapsulated specimens during the enthalpy measurements. The likelihood of contamination of the experimental equipment with condensed decomposition products needed to be established also, in order to determine what changes in experimental procedure might be necessary. Consequently, pyrolysis studies were made on representative samples of the materials used in the program.

For the pyrolysis studies, the samples were placed in a quartz tube which was then attached to a vacuum line. The system was pumped down to 10^{-5} torr at room temperature, and the specimen was then heated at a controlled rate, usually 3 C per minute. Total pressure in the system was recorded as a function of temperature, and at the end of the run, the number of cc-atm of gaseous products obtained per gram of sample was calculated. The percentage of char formed also was noted.

Anhydride-Cured Epoxy Novolacs

A specimen of the virgin polymer, DEN-438, was used for the pyrolysis experiments on this material. Stepwise heating was used in the first run, in order to simulate the thermal program of the enthalpy measurements, and continuous heating was employed in a subsequent run. The results are shown in Figure 1.

In the stepwise heating of the DEN-438 polymer, there was a gradual pressure increase above 280 C with a steep rise from 340 C, as shown in the upper curve of Figure 1. The gaseous products from a sample weighing 0.6176 gram amounted to 124 cc-atm/g at 425 C. The char remaining represented 49.5 percent of the sample weight. The weight loss which occurred below 350 C was primarily the result of the formation of high-boiling brownish liquids which condensed near the pyrolysis furnace. Infrared-spectrum indications were that these liquids were phenolic polymer materials.

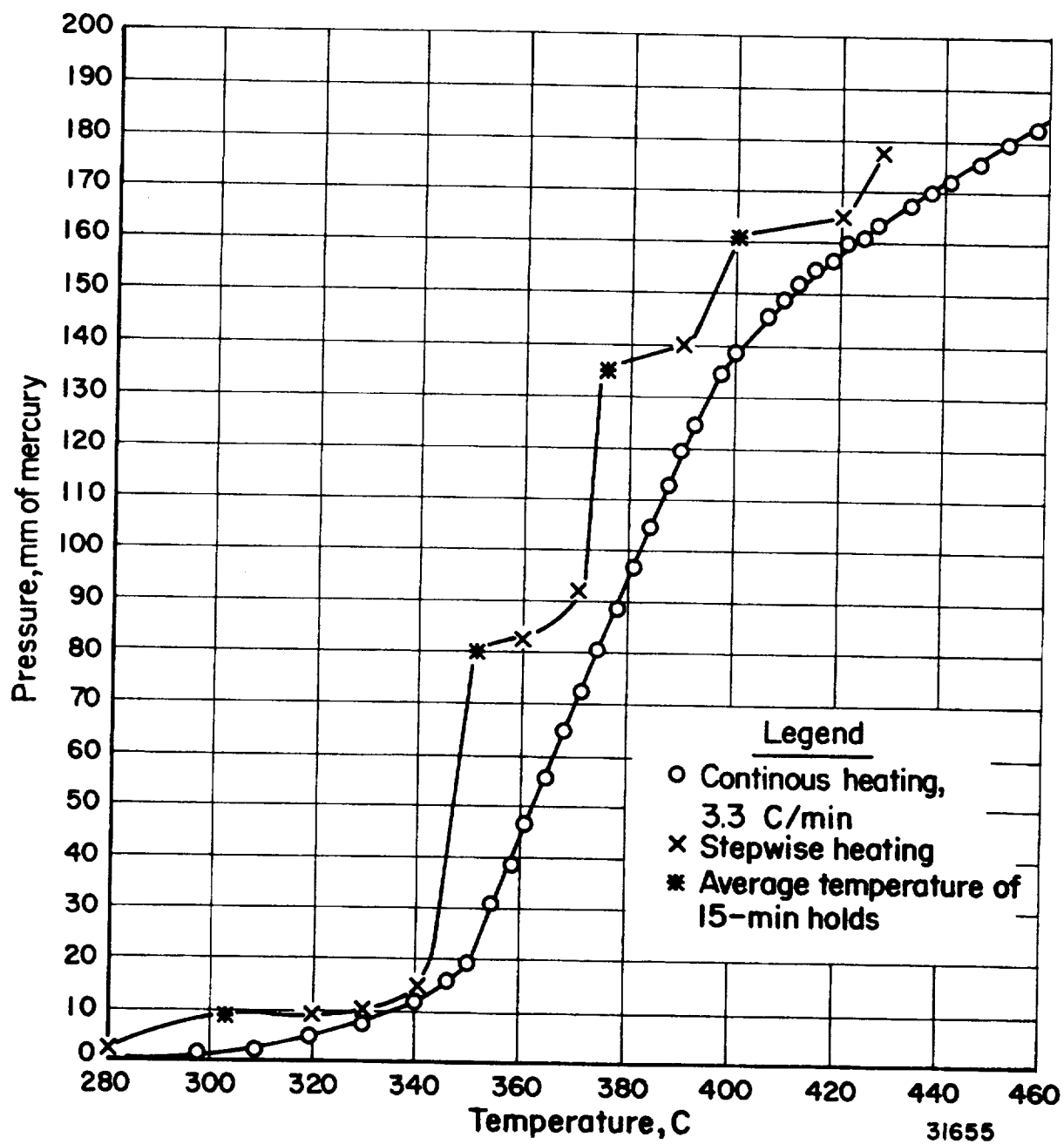


FIGURE 1. PRESSURE BUILDUP DURING PYROLYSIS OF DEN-438 POLYMER

Continuous heating was carried out at 3.3 C/min, and there was no observable gas pressure until a temperature of 280 C was reached. The anticipated rapid increase in pressure occurred between 350 and 400 C, and was accompanied by condensation of polymeric liquids, as before. The general pattern of rising pressure was found to be much the same as with the stepwise heating. In this case, the gaseous products from the same sample weight were only 110 cc-atm/g when the temperature reached 425 C. The char weight was 37.8 percent of the original sample weight.

It was concluded that the enthalpy capsules should be vented for measurements above 300 C, and that sleeves for collecting condensate would be provided in the thermal-expansion experiments to protect the equipment from decomposition products of the epoxy-novolac materials.

Polybenzimidazoles

A DXH-30 sample was used for pyrolysis experiments on this material. When subjected to stepwise heating, a 518-mg sample experienced a weight loss of 5.8 percent during the course of the experiment. The volatiles generated totaled 58 cc-atm/g. Data for this experiment are plotted in Figure 2.

The curves of Figure 2 show that between 100 and 530 C water is apparently the only product evolved from the material, as exemplified by the long horizontal section of the curve. At 530 C a rapid rise in pressure occurred, reaching 130 mm at 650 C.

The continuous heating curve for the DXH-30-2 specimen was almost the same as that observed with stepwise heating, as shown in the lower curve of Figure 2. However, the pressure reached at 650 C was only 95 mm, reflecting the much shorter time of this experiment. The weight loss after this treatment amounted to 7.8 percent and the volatiles totaled 65 cc-atm/g, which is in reasonable agreement with the stepwise-heating result. It was concluded that no special precautions were necessary in the handling of the polybenzimidazole samples during the thermophysical measurements.

Phenolic-Novolac Nylon

The thermal stability of the high-density phenolic nylon specimen PNHD-Hughes No. 4 was measured by continuous heating only, because previous experiments had shown that there was no significant difference in results with the stepwise and the continuous heating. The pressure of the gaseous-decomposition products obtained up to 800 C is shown in Figure 3. The char amounted to 30.4 percent of the original weight, and 237 cc-atm/g of gaseous products was obtained.

The PNLD-Langley material was used as representative of a low-density phenolic-nylon material. Results of the pyrolysis are shown in Figure 4. The amount of gaseous decomposition products obtained at any given temperature was almost twice that obtained with the high-density phenolic nylon, which reflects the relatively large amount of nylon as compared to phenolic novolac in the low-density material. The amount of gaseous products accumulated at 620 C was 204 cc-atm/g. A char weight of 37.0 percent resulted.

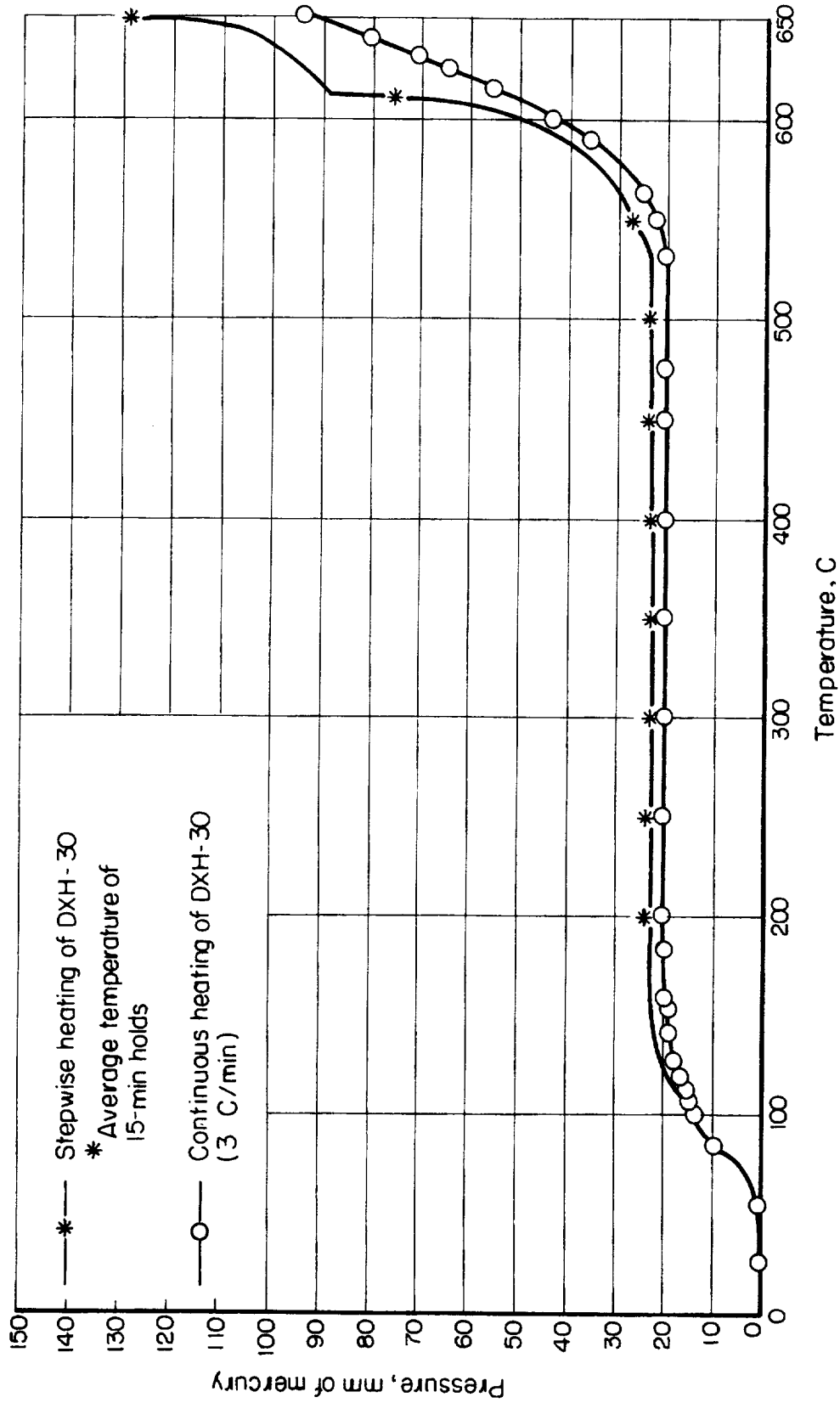


FIGURE 2. PRESSURE BUILDUP DURING PYROLYSIS OF DXH-30 MATERIAL

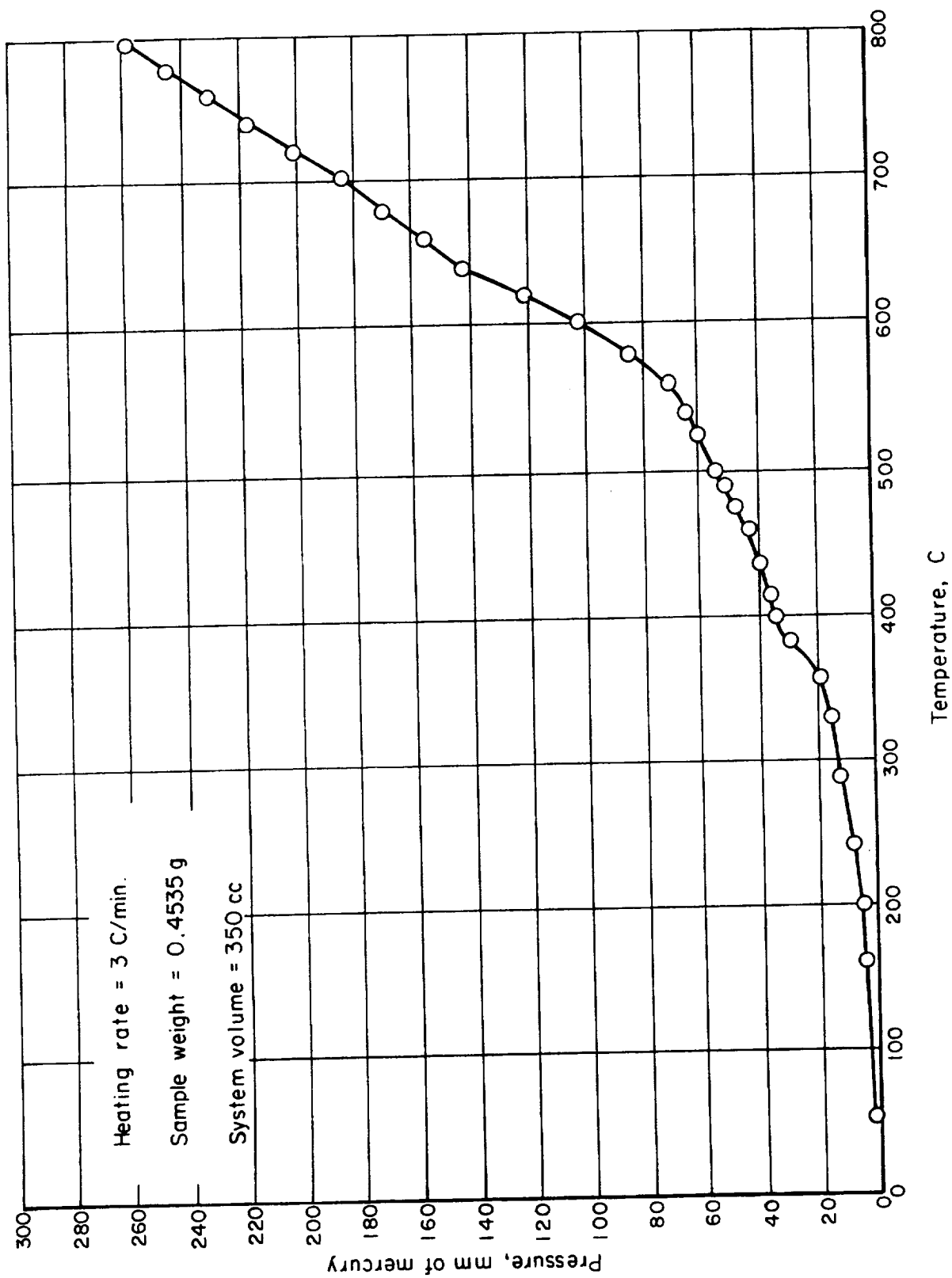


FIGURE 3. PRESSURE BUILDUP DURING PYROLYSIS OF PNHD-HUGHES-4 SPECIMEN

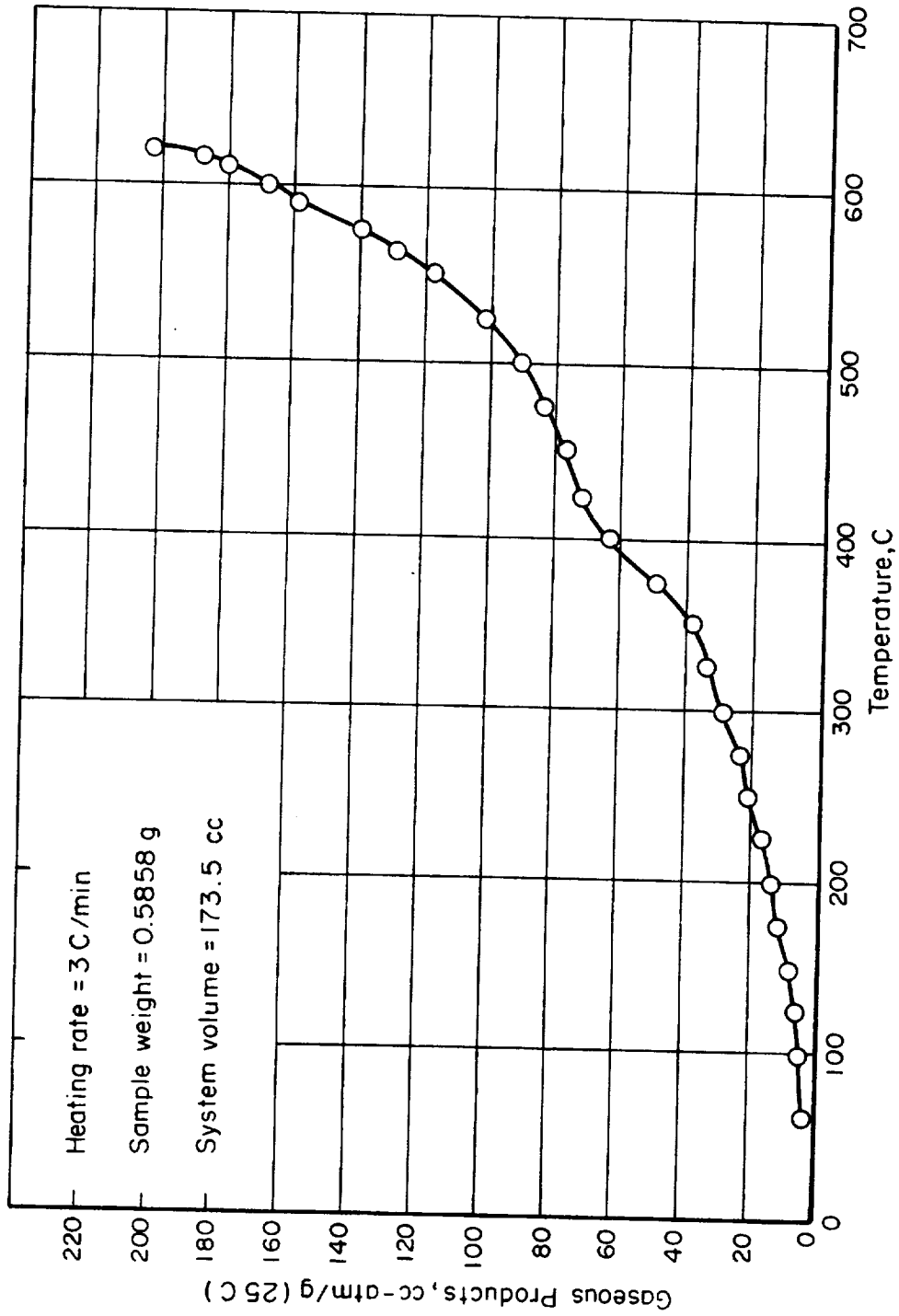


FIGURE 4. PYROLYSIS CURVE FOR PNLD-LANGLEY SPECIMEN

Phenolic-Nylon Chars

Four phenolic nylon samples which had been charred at 1000 C by NASA-Ames were reheated to that temperature in the pyrolysis experiments. The results are presented in Figure 5. In spite of the fact that these samples had been heated to 1000 C previously, the NA-12 and NA-15 specimens produced a significant amount of volatiles above 600 C during the pyrolysis treatment. A total of 97 cc-atm/g of gaseous products was obtained from NA-12 and 69 cc-atm/g from NA-15. The other two specimens, NA-13 and NA-14 yielded a very small amount of gaseous decomposition products, only 17 and 19 cc-atm/g respectively.

It should be noted that inflection points were observed in the pyrolysis curves for samples NA-12 and NA-14. When plotted on a larger scale, an inflection point for NA-12 was noted at 250 C, with a much more pronounced one at approximately 500 C. There was also an inflection point for NA-14 at 250 C. The change in decomposition behavior at these temperatures was found to have an effect on the thermal conductivity of these materials at the above-mentioned temperatures, and this is discussed later in this report.

Density

In order to calculate the thermal diffusivity of the materials, it was necessary to have accurate measurements of the density of the samples before they were subjected to thermal treatment. The densities of the various materials at room temperature were determined from weight and dimensional measurements on cubical or cylindrical specimens. To obtain values of the density above room temperature, linear-thermal-expansion data were also employed. It was assumed in these calculations that the materials were isotropic. Density values for the materials are shown in Table 3.

TABLE 3. DENSITIES OF ABLATIVE POLYMER MATERIALS

Material Temperature, C	Density, g/cc ^(a)				
	20	100	200	300	400
DEN-438	1.24	1.22	1.19	1.13	----
DEN-438 + chopped glass	1.33	1.31	1.27	1.20	----
DEN-438 + glass microballoons	0.61	0.61	0.60	0.58	----
DXH-30	0.49	0.49	0.49	0.48	0.48
DXH-31	0.50	0.50	0.50	0.49	0.49
DXH-32	0.50	0.50	0.50	0.50	0.50
EXEH-31	0.50	0.49	0.49	0.48	0.47
PNHD-Hughes No. 4	0.52	0.51	0.50	0.49	----
PNHD-Hughes No. 5	0.56	0.55	0.54	0.53	----
PNLD-Langley	0.55	0.54	0.53	0.52	----

(a) Based on room-temperature density and linear-thermal-expansion data.

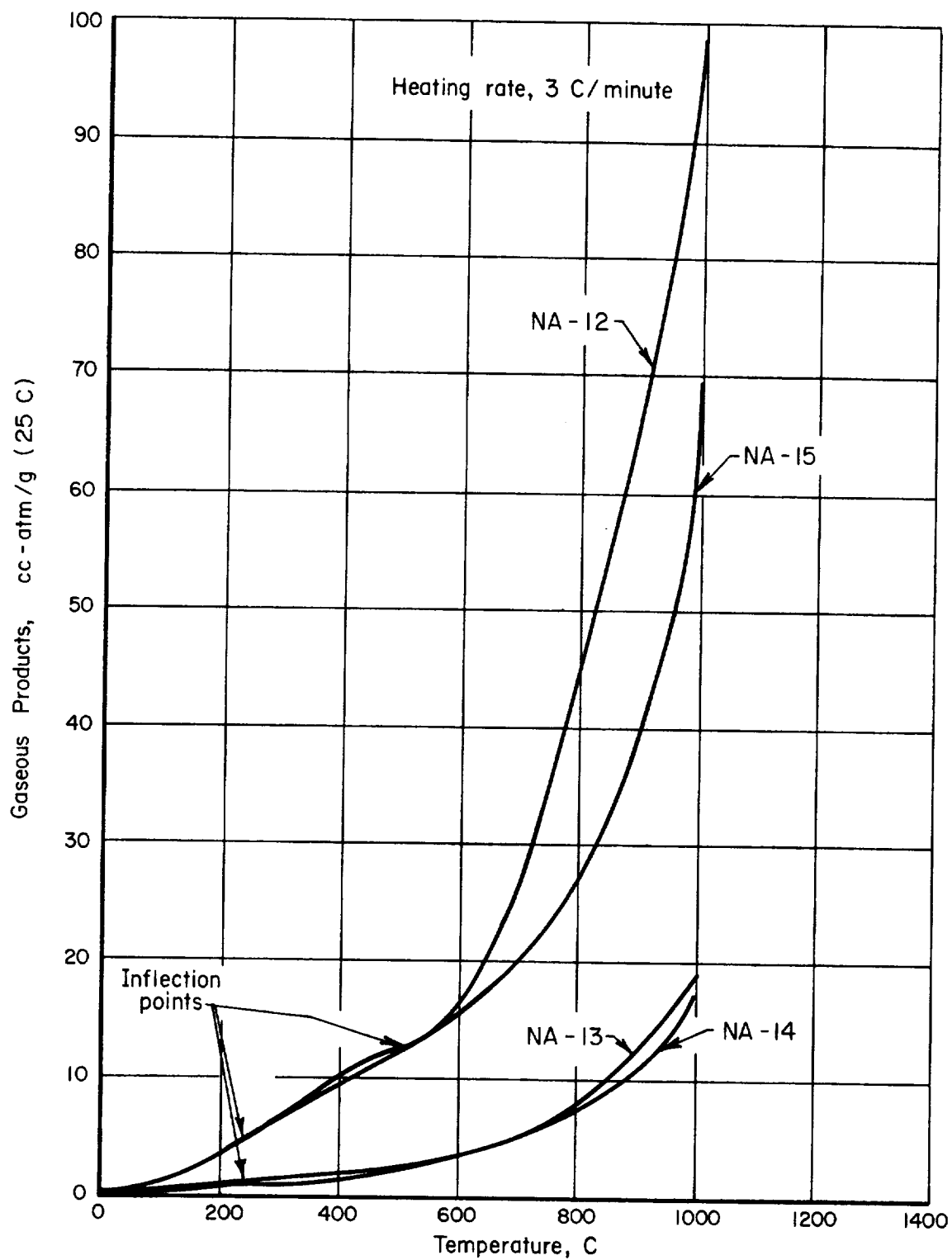


FIGURE 5. PYROLYSIS CURVES FOR PHENOLIC NYLON CHARs

THERMOPHYSICAL-PROPERTY MEASUREMENTS

The measurements made on the various materials and nominal temperature ranges covered are shown in Table 1 of the Summary. Measurements chosen for this phase of materials characterizations included thermal conductivity, enthalpy, and linear thermal expansion. Specific heat was calculated from enthalpy, and density at temperature was estimated from room-density values and expansion with temperature. Thermal diffusivity was calculated as the ratio of thermal conductivity to the product of density and specific heat.

Thermal Conductivity

J. F. Lagedrost and T. J. Fabish

Methods and Apparatus

The thermal-conductivity measurements were made in the self-guarding disk apparatus described in Appendix E. The nominal specimen dimensions for this apparatus are 3 inches in diameter by 1/2 inch thick. Heat is introduced to one surface of the disk and its flow through the disk is measured by a heat-flow meter on the opposite face. Temperature differences which occur at specific locations in the disk for various heat flows are indicated by thermocouples in the specimen.

Thermal-conductivity measurements were made in different atmospheres, including argon, helium, and vacuum.

Anhydride-Cured Epoxy Novolacs

Thermal-conductivity measurements of the epoxy-novolac (DEN-438) materials were carried out for the most part under helium. Checking of selected points under an atmosphere of argon showed that there was no difference in thermal conductivity as measured in the two gases. Specimens of this group that were measured comprised:

DEN-438

DEN-438 + chopped glass

DEN-438 + glass microballoons.

Experimental data points and visually fitted curves are shown in Figures A-1, A-2, and A-3 in Appendix A.

Figure 6 is a composite showing smoothed curves of thermal conductivity versus temperature for the DEN materials.

The epoxy-novolac materials evidently have a low, continuous porous phase because there was no measurable difference in thermal conductivity when the material was measured in argon and then in a helium atmosphere.

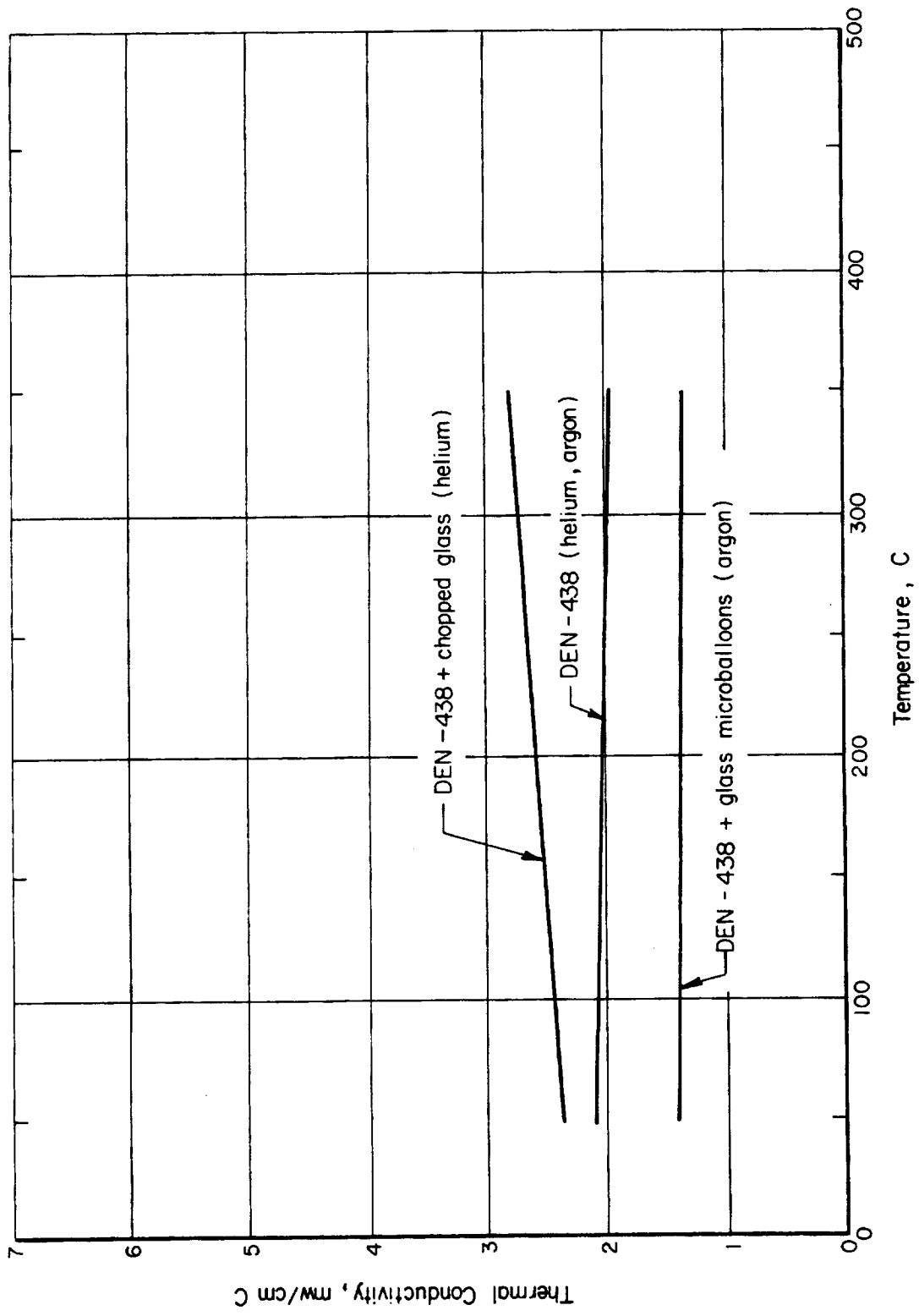


FIGURE 6. THERMAL CONDUCTIVITIES OF ANHYDRIDE-CURED EPOXY NOVOLAC MATERIALS

Polybenzimidazoles

Thermal-conductivity measurements of the polybenzimidazoles were made in argon, helium, and vacuum. The atmosphere used had a greater influence on the thermal conductivity of these specimens than on that of the epoxy-novolac materials because the polybenzimidazole materials were more porous. The effect of the various atmospheres on conductivity is discussed in the next section.

Specimens of the polybenzimidazole group that were measured included the following:

DXH-31

DXH-32

EXEH-31.

Curves of thermal conductivity versus temperature, along with comments concerning the individual measurements, are included in Figures A-4, A-5, and A-6 in Appendix A. The curves were visually fitted to the plotted experimental data points. The smoothed curves for these specimens are shown in Figure 7.

It is noted that the thermal conductivity of Specimen EXEH-31 containing 15 percent alumina fibers plus 20 percent phenolic microballons is lower than that of Specimen DXH-31 which contains 15 percent alumina fibers plus 20 percent silica microballons. Both specimens were measured in argon. Near room temperature, the thermal conductivity of the EXEH-31 specimen is about half as great as that observed under the same conditions for DXH-31, which reportedly differs only in the nature of the PBI used. The thermal conductivity of the EXEH-31 increased with temperature, becoming approximately equal to that of the DXH-31 at 450 C.

Phenolic-Novolac Nylons

Thermal-conductivity measurements were made on the following specimens of the phenolic-novolac nylon group:

PNHD-Hughes No. 4

PNHD-Hughes No. 5

PNLD-Langley.

Experimental data points and visually fitted curves are shown in Figures A-7, A-8, and A-9 in Appendix A.

Figure 8 shows smoothed curves of thermal conductivity versus temperature for these specimens.

A calculated thermal-conductivity curve for Specimen PNHD-Hughes No. 5 is also included in Figure 8. Appendix E gives details of thermal-diffusivity measurements made on this specimen in order to permit calculation of thermal conductivity as the product of thermal diffusivity, density, and specific heat.

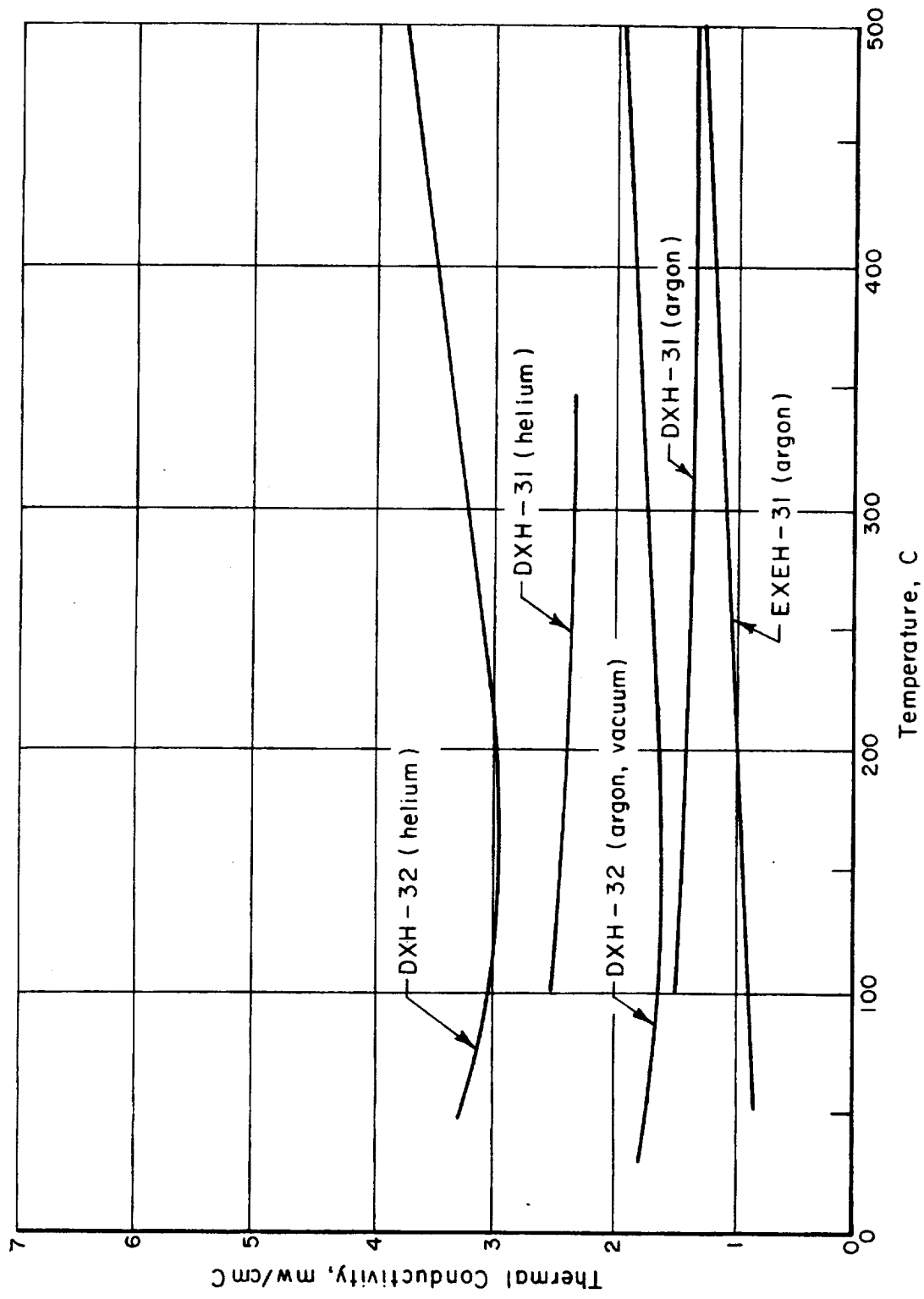


FIGURE 7. THERMAL CONDUCTIVITIES OF POLYBENZIMIDAZOLE MATERIALS

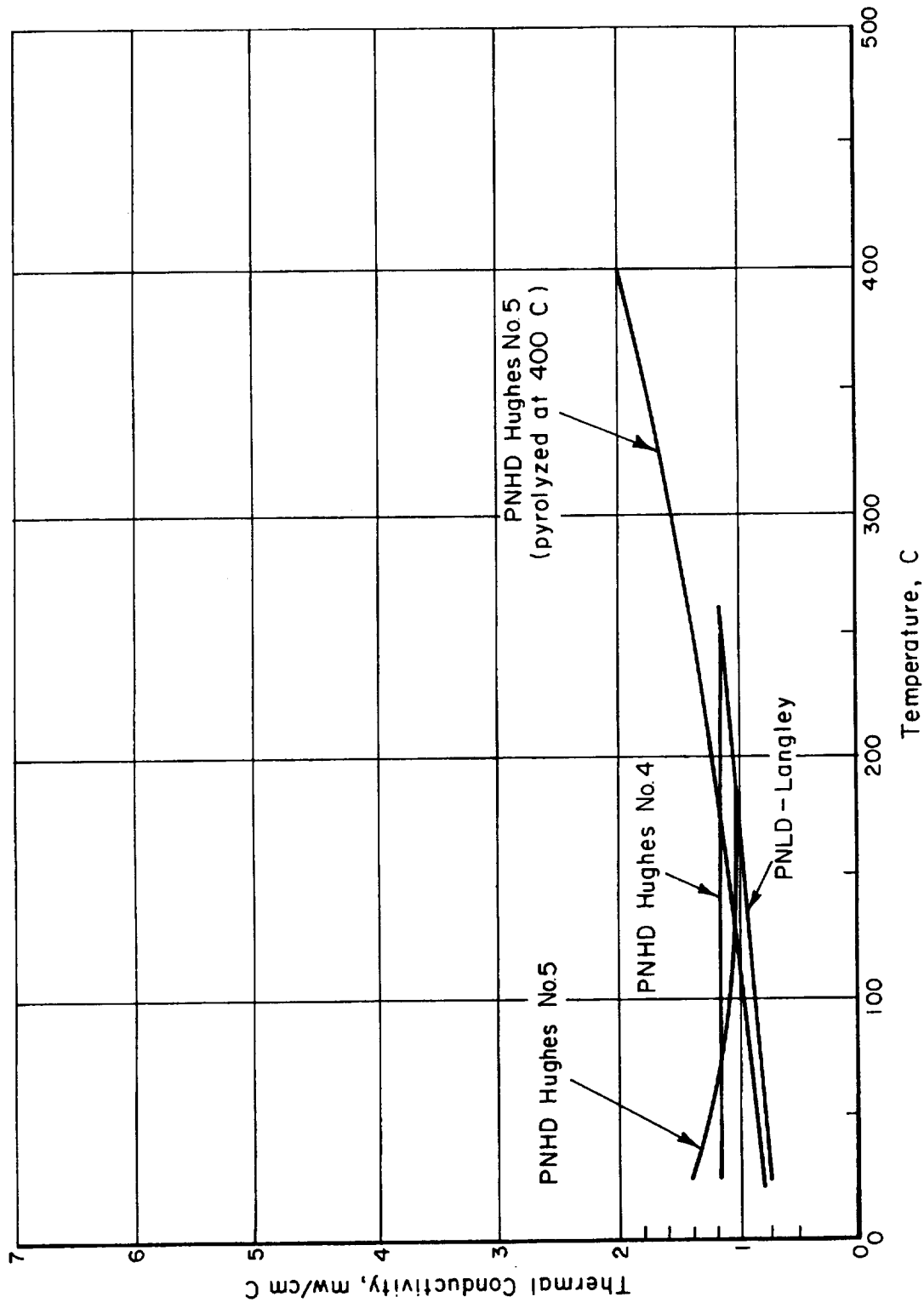


FIGURE 8. THERMAL CONDUCTIVITIES OF PHENOLIC NYLONS

Phenolic-Nylon Chars

Thermal-conductivity measurements were made on the following phenolic-nylon char specimens:

NA-12

NA-13

NA-14

NA-15.

Experimental data and visually fitted curves for the individual specimens are shown in Figures A-10 through A-13 in Appendix A.

Figure 9 shows smoothed curves of thermal conductivity versus temperature for the four specimens. The measurements were made with the specimens in a vacuum of about 20 microns.

Influence of Pore Structure on Thermal Conductivity of Polybenzimidazole Char Material

T. J. Fabish

A study was made to determine the feasibility of arriving at the effective porosity of a material from the results of thermal-conductivity measurements performed in various gaseous environments. The polybenzimidazole specimen DXH-32 which had been pyrolyzed at 650 C was chosen as the focus for the study. Preliminary thermal-conductivity measurements had given different values in argon and in helium.

Experimental work performed on this specimen included mercury-porosimeter measurements of open-porosity pore-size distribution, helium pycnometer and bulk-density measurements (total porosity), and thermal-conductivity measurements in vacuum, argon, and helium environments over the temperature range 0 to 450 C.

Analytical efforts included applying three of the numerous available theories concerning the effects of porosity on thermal conductivity to the experimental results to correlate the thermal-conductivity data with pore structure. The three theories applied in the study included the two theoretically sound theories due to Rayleigh* and Eücken**, and the phenomenological theory of Loeb***.

The measurements and analysis are fully described in Appendix B. Several of the results are summarized here.

*Rayleigh, L., "On the Influence of Obstacles Arranged in Rectangular Order Upon the Properties of a Medium", Philosophical Magazine, 34, 481-503 (1892).

**Eücken, A., "Heat Conductivities of Ceramic-Refractory. Calculations of Heat Conductivity From the Constituents", Forsch. Gebiete Ingenieurw., 3 (353), 1-16 (1932).

***Loeb, A. L., "Thermal Conductivity: VIII, A Theory of Thermal Conductivity of Porous Materials", Journal of the American Ceramic Society, 37, 96-99 (1954).

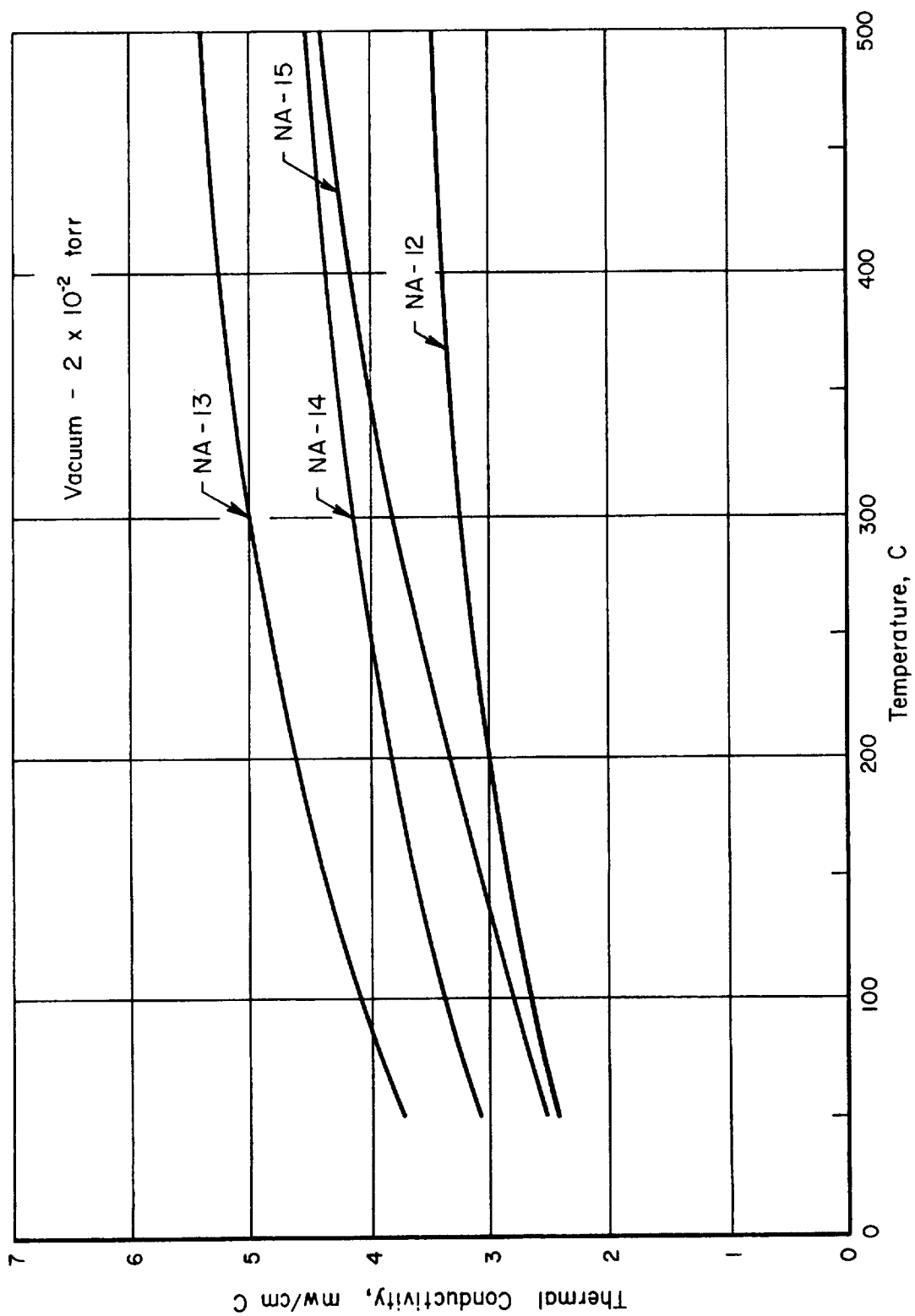


FIGURE 9. THERMAL CONDUCTIVITIES OF PHENOLIC NYLON CHARS

- (1) The pore structure had to be extensive enough to produce significant differences (at least 10 percent in these measurements) between the thermal conductivities determined in vacuum and helium environments to permit calculation of the void fraction.
- (2) The results of the total porosity and pore-size-distribution determinations, along with molecular theory, suggested a two-phase model for an analytical description of the void volume, the first phase being comprised of pores large enough in size to support ordinary gas conduction, the second containing the remainder of the discrete pores.
- (3) The average void fractions calculated from the vacuum and helium thermal-conductivity data for DXH-32 by means of the Eücken and Loeb equations were in quantitative agreement with that fraction of the measured total porosity comprised of pores large enough in diameter to support ordinary helium-gas conduction. This conclusion applied over the temperature range 100 C to 400 C wherein the slopes of the conductivity-temperature curves were defined most precisely by the experimental data.

The analytical description of the effects of voids on the thermal conductivity necessitated the construction of specific models for the porous material. The various predictions derived from these models for the influence of gas conduction within the discrete pores on the net thermal conductivity are discussed in Appendix B. The experimental data were not extensive enough to fully test the models developed in this study. Appendix B also contains recommendations for a more extensive investigation of the effects of pore structure on thermal conductivity.

X-Ray Diffraction and Electron-Microscope Studies of Phenolic-Nylon Char

D. A. Vaughan

The phenolic-nylon-char specimen NA-13 was selected for examination by X-ray diffraction and electron microscopy. This specimen had the highest thermal conductivity of the set of four phenolic-nylon chars, and should exhibit the largest amount of crystallinity. The NA-13 sample was charred at 1000 C at Ames and held at temperatures from 100 to 600 C for about 1 week during the thermal-conductivity measurements at Battelle. Samples from the upper and lower face of the specimen were taken for the X-ray and electron-microscope investigation.

X-ray diffraction analyses showed both surfaces to contain carbon plus a small amount of KBr, which would not be unusual in phenolic nylons. The presence of bromine was confirmed by X-ray fluorescence. As the experimental technique employed was not capable of detecting radiation from elements with atomic numbers less than about 22, the presence of potassium was not confirmed by fluorescence, but the X-ray diffraction data were sufficient proof. Crystallite-size measurements were obtained from X-ray line-broadening analyses and were found to be 10 Å and 15 Å for the lower face and upper face specimens, respectively. This difference is not considered to be significant, as the precision in the determination is probably of the order of ± 10 Å. However, the low

pyrolysis temperature (1000 C) contributed to the crystallite size of the specimens being smaller than the 20 to 40 A observed in other studies* for pyrolytic carbon produced from C_2H_2 or CH_4 at 1250 C.

The internal structure of the carbon produced by the pyrolysis treatment was investigated on microtomed thin sections. Typical electron micrographs of specimens from the upper and lower face are shown in Figures 10 to 13. The scalloped effect seen in Figures 10 and 11 is a result of the brittle nature of the material or of the orientation of the specimen relative to the cutting knife. Scattered throughout both micrographs are high-density (black) areas which are particularly evident as stringers in Figure 11. These high-density areas may represent high-density carbon or KBr particles which would also appear more dense than the carbon matrix. The grains in both of these materials are too fine to be resolved to 75,000X, an observation which is also true for carbon formed by decomposition of C_2H_2 at 1250 C.⁽¹⁾ At 372,000X, the carbon grain structure is now visible in the form of dots (Figures 12 and 13). High-density zones previously described are still observed. The lower face specimen (Figure 12) also exhibits small, dense, circular regions not seen in the upper face specimen (Figure 13). These regions may represent higher density carbon or an impurity phase even though additional phases were not observed by electron diffraction.

The extremely small crystallite size and fine grain structure of carbon produced by decomposition of phenolic nylon is similar to that observed in carbon formed from the decomposition of C_2H_2 or CH_4 . However, the presence of KBr in both specimens and the small high-density regions in the lower face specimen suggest some differences in structure between phenolic-nylon carbon and that obtained from C_2H_2 or CH_4 . It is possible that the fracture characteristics of the phenolic-nylon carbon are related to the polymer chain in the precursor; however, there is no evidence for a preferred orientation of the carbon grains. The inability to detect a preferred orientation may be due to the small crystallite size of the resulting carbon.

In relating these results to the thermal conductivity measured for Sample NA-13, no significance can be attached to the designation of properties of the upper and lower face specimens because measurements were made with heat flow in both directions. Figures 12 and 13 offer some evidence that the structure may not be uniform across the thickness of the specimen. Such a condition could explain the scatter observed in some of the data points for thermal conductivity of NA-13, which showed greater deviation from the mean than could be explained by experimental error. The pyrolysis curve showed the material to be stable in the temperature range of interest, so the deviations could not be attributed to pyrolysis reactions influencing the measured temperature gradient in the specimen.

Enthalpy, Specific Heat

E. A. Eldridge and H. W. Deem

Enthalpy measurements were made using a Bunsen ice calorimeter as described in Appendix E.

*Browning, M. F., et al., "Characterization of Pyrolytic Carbon Fuel-Particle Coatings Prepared With Acetylene", USAEC Report BMI-1735, July 19, 1965.



75,000X

J16238

FIGURE 10. ELECTRON MICROGRAPH OF A THIN SECTION FROM
THE COLD FACE SPECIMEN

NOT REPRODUCIBLE

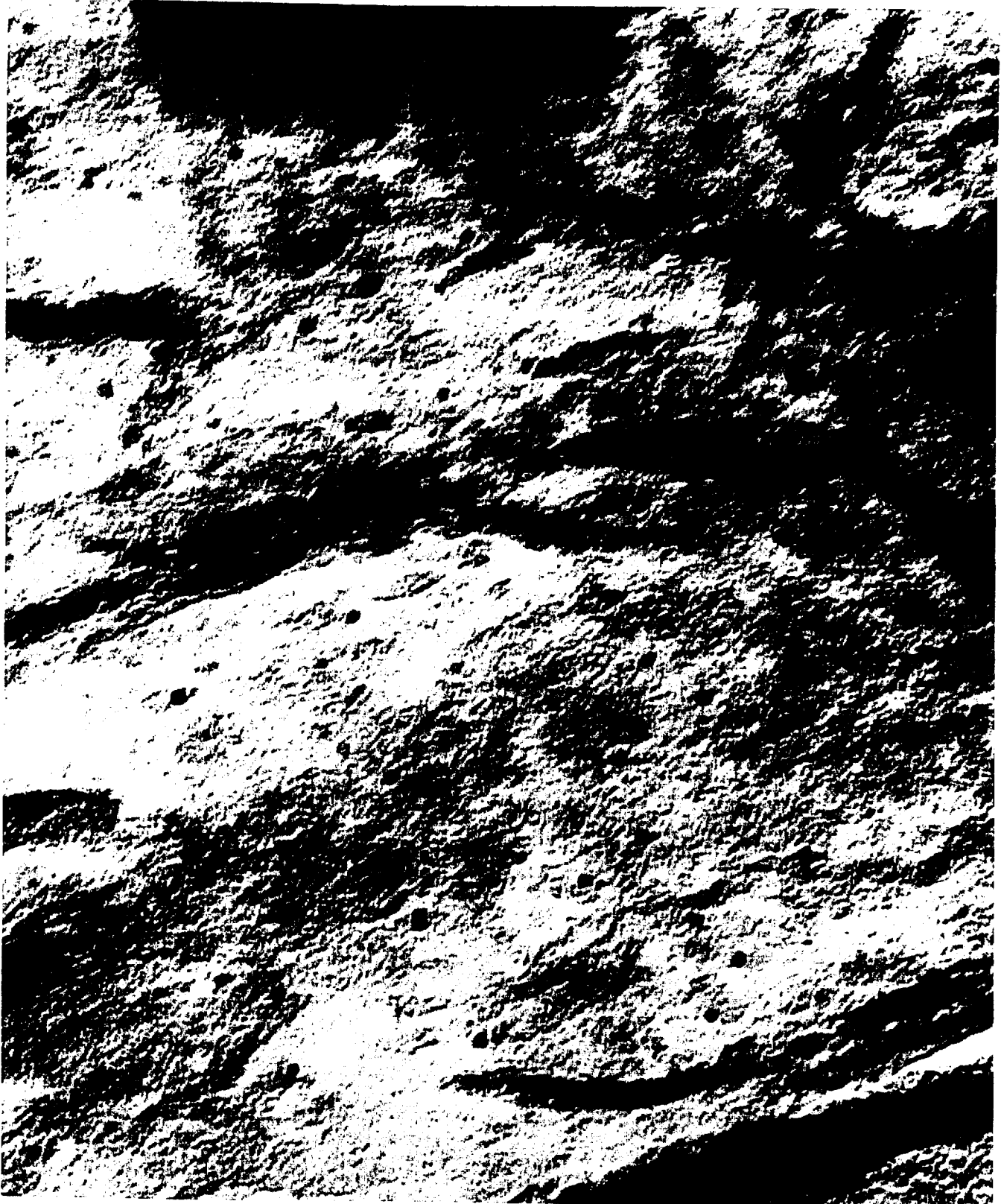


75,000X

J16241

FIGURE 11. ELECTRON MICROGRAPH OF A THIN SECTION FROM
THE HOT FACE SPECIMEN

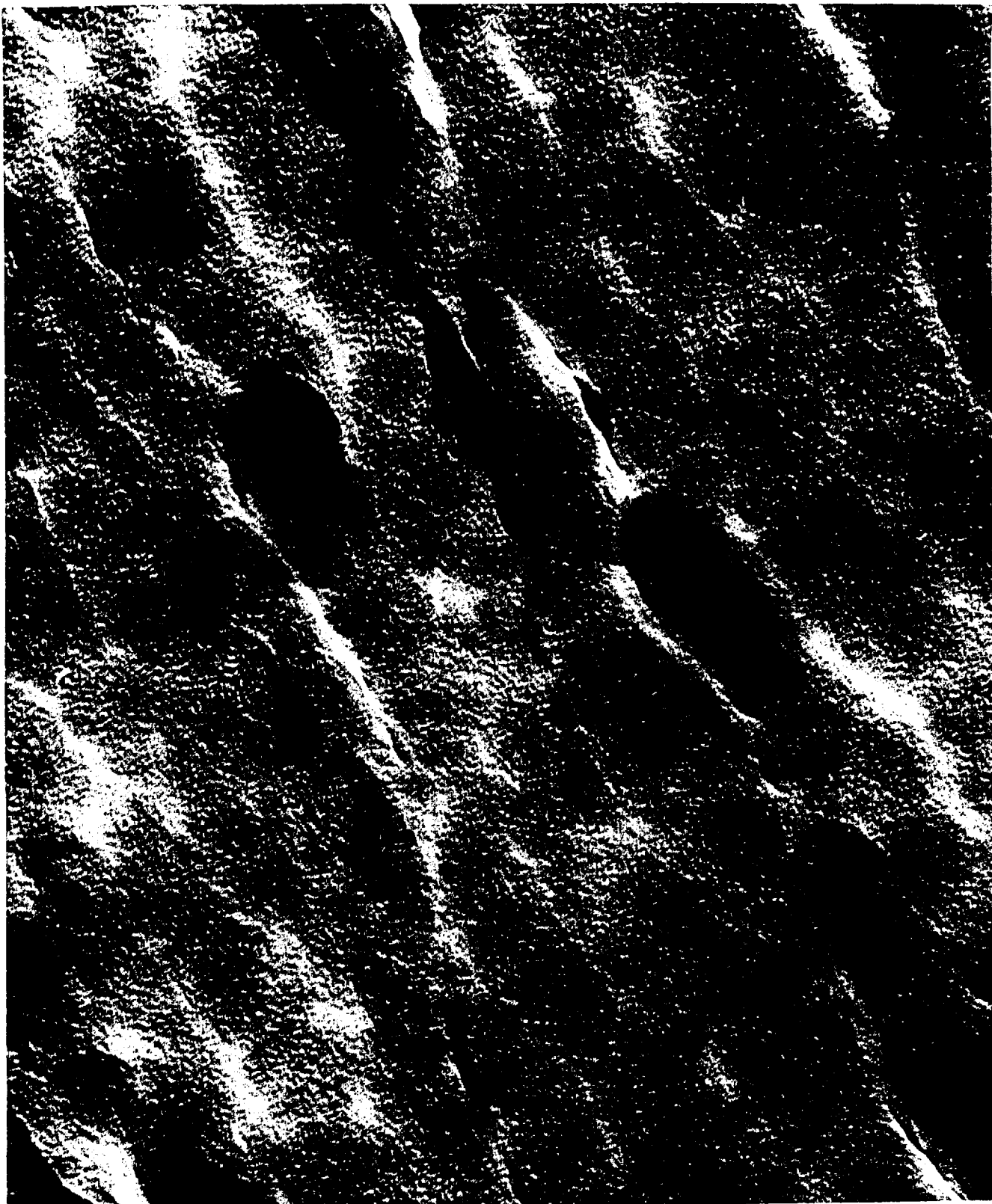
NOT REPRODUCIBLE



372,000X

J16240

FIGURE 12. ELECTRON MICROGRAPH OF A THIN SECTION FROM
THE COLD FACE SPECIMEN



372,000X

J16244

FIGURE 13. ELECTRON MICROGRAPH OF A THIN SECTION FROM
THE HOT FACE SPECIMEN

NOT REPRODUCIBLE

Enthalpy is a thermodynamic quantity equal to the sum of the internal energy of a system and the product of the pressure-volume work done on the system. Measurement of this quantity is usually made by heating a material and determining the total heat transfer from it for a given temperature change. For this portion of the program, where the specimens in some cases undergo chemical change on heating, the measured enthalpy is representative of both the reaction products and the original material.

Anhydride-Cured Epoxy Novolacs

Enthalpies were measured and specific heats calculated for the following materials of this group:

DEN-438

DEN-438 + chopped glass

DEN-438 + glass microballoons.

In each case, several measurements were made on encapsulated material in the temperature range from approximately 0 C to 350 C for the epoxy specimens. Experimental enthalpy data and equation-fitted curves are shown in Figure C-2 of Appendix C. Details of encapsulation, such as vented and unvented capsules, are also given in Appendix C.

Equations were fitted to the enthalpy curves, and these in turn were differentiated to obtain the specific heats of the materials. The specific heats calculated in this fashion are presented in Figure 14. The specific-heat curves are linear, and increase with temperature.

Equations expressing enthalpy and specific heat as functions of temperature were derived from the experimental data. These are given below for each of the materials.

DEN-438

$$H_t = 0.275t + 4.11 \times 10^{-4}t^2$$

$$C_p = 0.275 + 8.22 \times 10^{-4}t$$

DEN-438 + chopped glass

$$H_t = 0.238t + 4.19 \times 10^{-4}t^2$$

$$C_p = 0.238 + 8.39 \times 10^{-4}t$$

DEN-438 + glass microballoons

$$H_t = 0.228t + 3.56 \times 10^{-4}t^2$$

$$C_p = 0.228 + 7.13 \times 10^{-4}t$$

Where

H_t = enthalpy, cal g⁻¹

C_p = specific heat, cal g⁻¹C⁻¹

t = temperature, C.

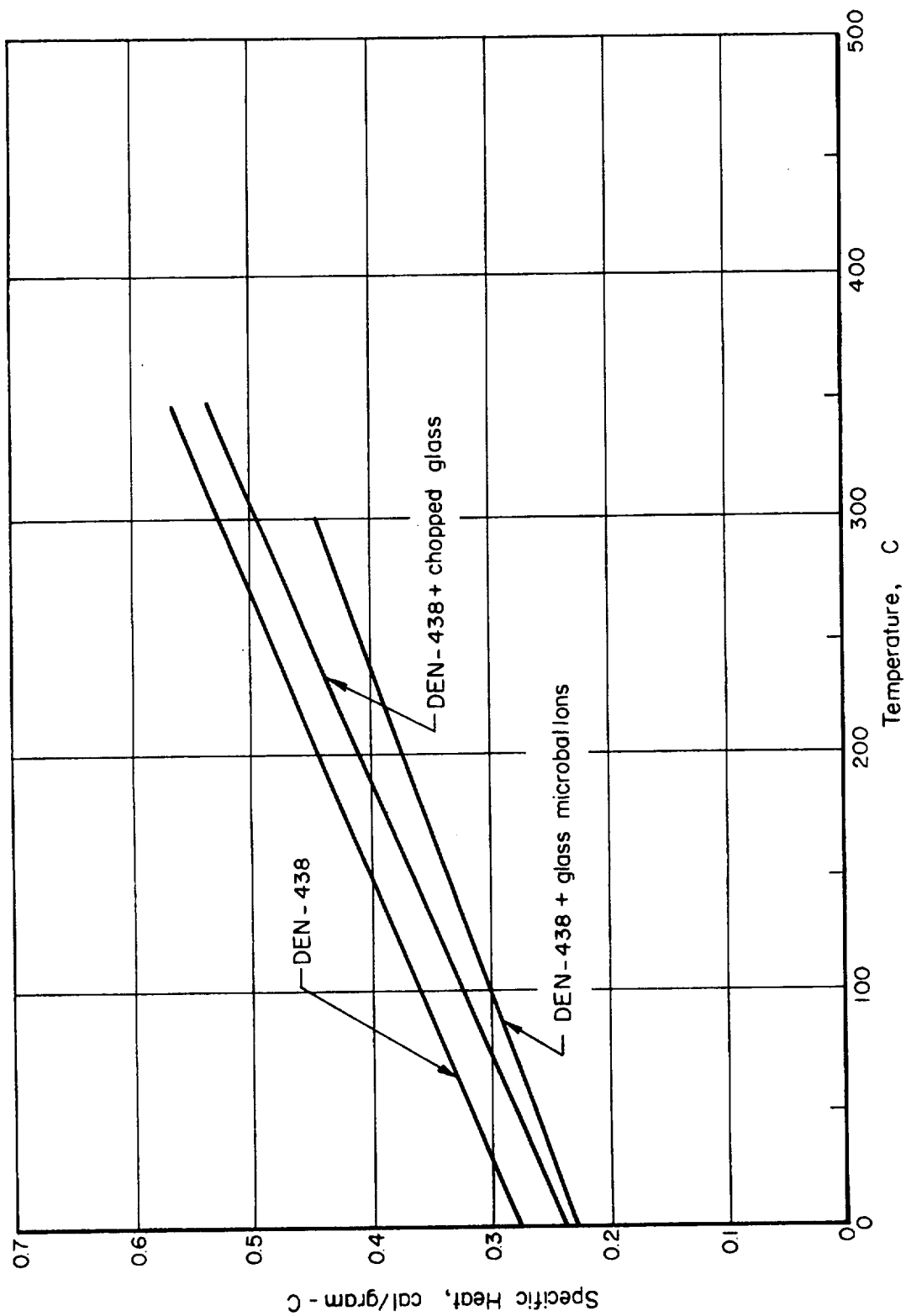


FIGURE 14. SPECIFIC HEATS OF ANHYDRIDE - CURED EPOXY NOVOLAC MATERIALS

Polybenzimidazoles

Enthalpies were measured and specific heats calculated for the following specimens of the polybenzimidazole group:

DXH-31

DXH-32, pyrolyzed at 650 C

EXEH-31.

Experimental enthalpy data and equation-fitted curves are shown in Figure C-2 of Appendix C. Figure 15 shows curves of specific heat versus temperature derived from the enthalpy relations.

Phenolic-Novolac Nylons

Enthalpies were measured and specific heats calculated for the following materials of the phenolic-novolac nylon group:

PNHD-Hughes No. 4

PNHD-Hughes No. 5

PNLD-Langley

PNHD-Hughes No. 5, charred at 400 C.

Experimental enthalpy data and equation-fitted curves are shown in Figures C-3 through C-6 in Appendix C. Figure 16 shows curves of specific heat versus temperature calculated from the specific-heat equations given below.

PNHD-Hughes No. 4

$$H_t = 0.237t + 9.44 \times 10^{-4}t^2$$

$$C_p = 0.237 + 1.89 \times 10^{-3}t$$

PNLD-Langley

$$H_t = 0.223t + 1.33 \times 10^{-3}t^2 - 1.28 \times 10^{-6}t^3$$

$$C_p = 0.223 + 2.66 \times 10^{-3}t - 3.84 \times 10^{-6}t^2$$

PNHD-Hughes No. 5, Precharred at 400 C

$$H_t = 0.258t + 4.05 \times 10^{-4}t^2 \quad (0-400 \text{ C})$$

$$C_p = 0.258 + 8.10 \times 10^{-4}t \quad (0-400 \text{ C}).$$

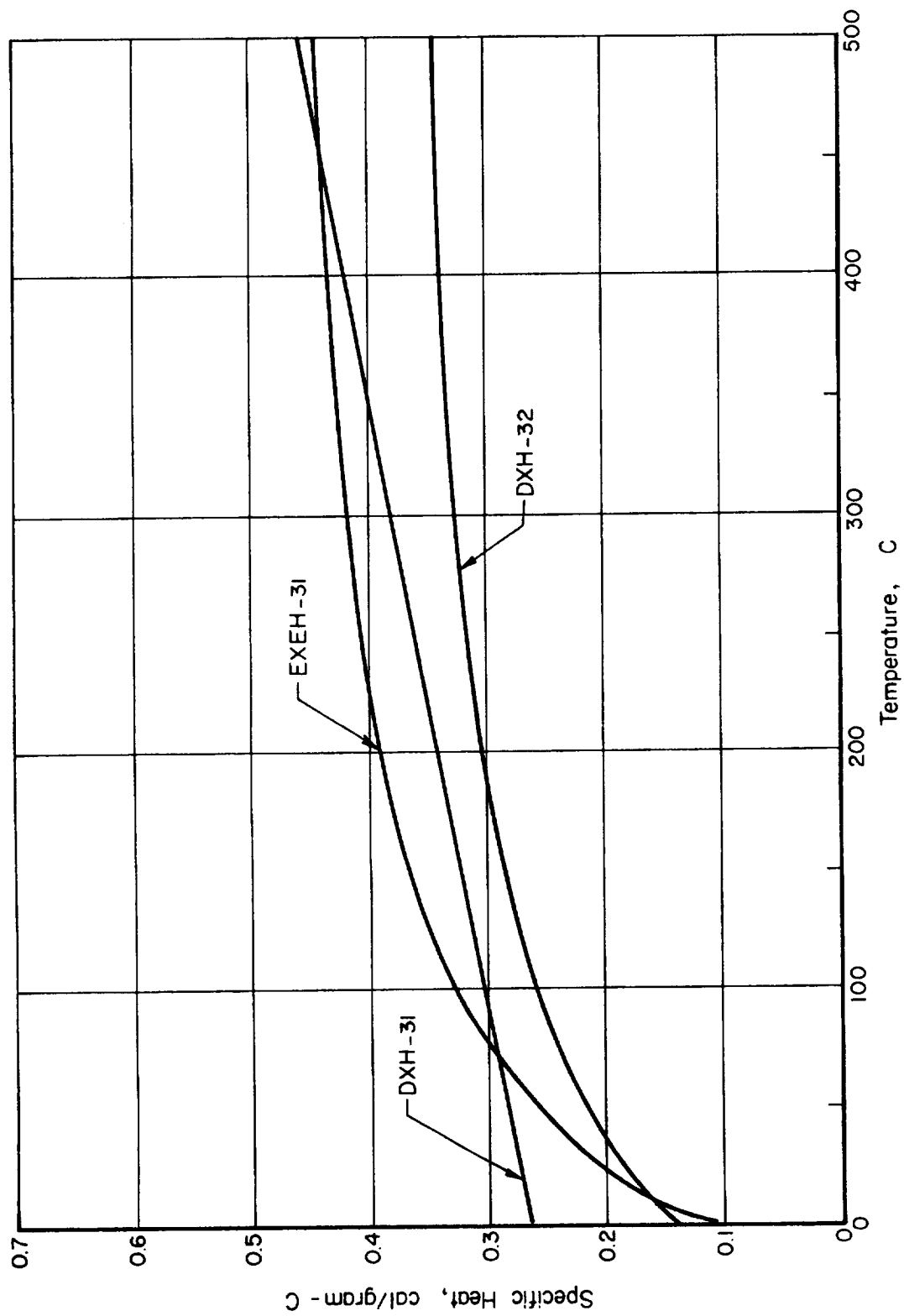


FIGURE 15. SPECIFIC HEATS OF POLYBENZIMIDAZOLE MATERIALS

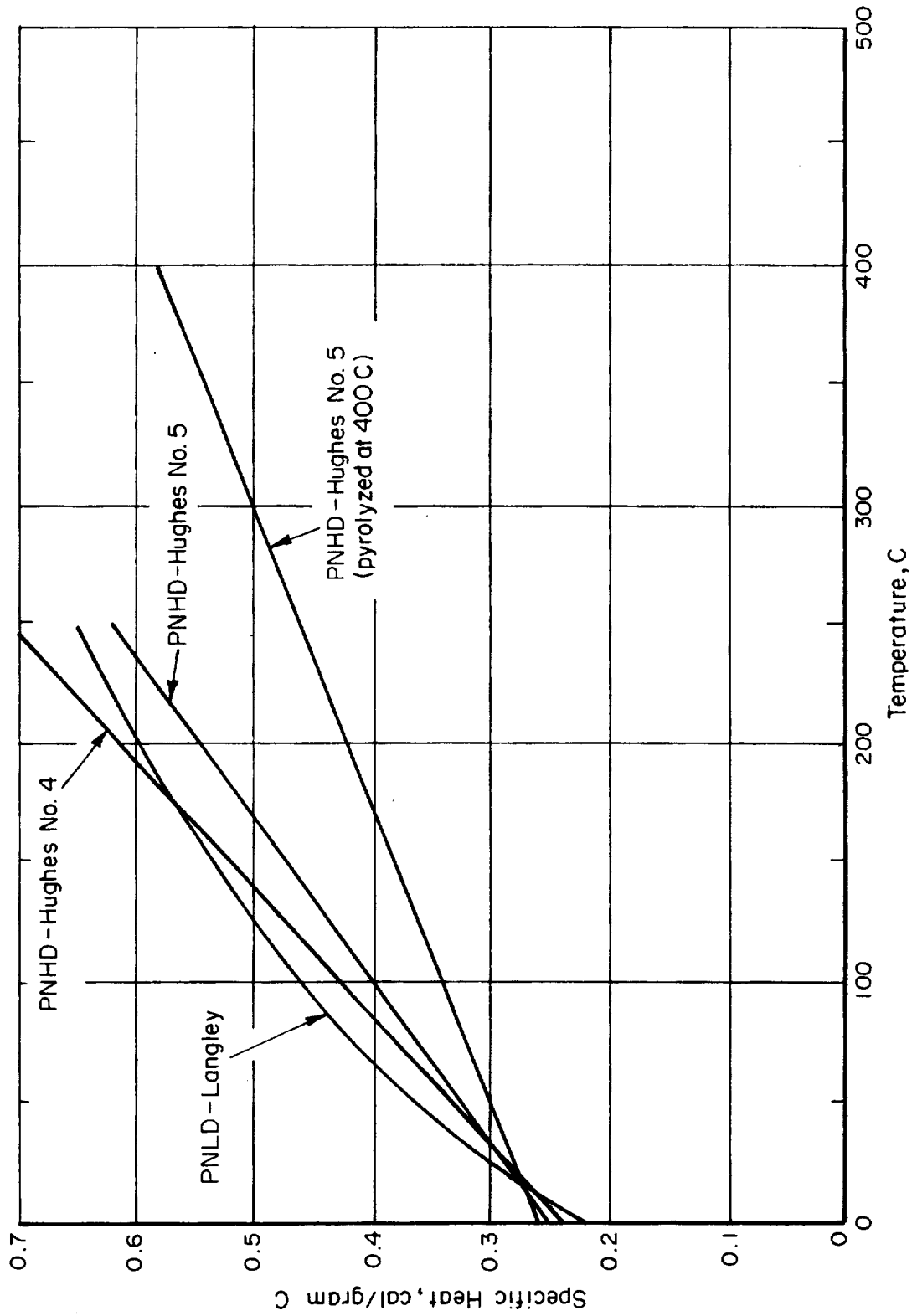


FIGURE 16. SPECIFIC HEATS OF PHENOLIC-NOVOLAC NYLON MATERIALS

Linear Thermal Expansion

E. A. Eldridge and H. W. Deem

Linear-thermal-expansion measurements were made using a clear-fused-quartz-structured manual dilatometer as described in Appendix E. The specimens were cylinders nominally 3/8 inch in diameter and 3 inches long. The weight of this quartz push-rod plus the spring loading of the dial indicator was about 140 grams. This loading is equivalent to about 6-psi compressive loading on the specimens.

Anhydride-Cured Epoxy Novolacs

Linear thermal expansions were measured for the following materials in the virgin state.

DEN-438

DEN-438 + chopped glass

DEN-438 + glass microballoons.

Experimental data points and visually fitted curves are shown in Figures D-1, D-2, and D-3 in Appendix D. Details of the individual measurements are also given in Appendix D.

These results show that for DEN-438 materials heated to about 325 C, there is no significant difference in the expansion found in air and in argon. Above that temperature, decomposition is sufficient to cause the sample to contract, and the expansion plots in air and argon diverge. In each case the sample measured in argon showed a greater net dimensional change when returned to room temperature, suggesting that surface oxidation in air may provide a slight dimensional stability.

Among the different DEN materials, both the unfilled polymer and that containing chopped glass expanded 3.5 percent. The DEN-438 with glass microballoons expanded only about 1.5 percent, however, and the contraction was only 1/5 to 1/4 as much as that of the other two DEN materials. This greater stability is probably the result of the high loading with glass.

Figure 17 shows a composite of all expansion curves, including those for the epoxy-novolac specimens measured.

Polybenzimidazoles

Linear-thermal-expansion measurements were made on the following polybenzimidazole specimens:

DXH-31

DXH-32

EXEH-31.

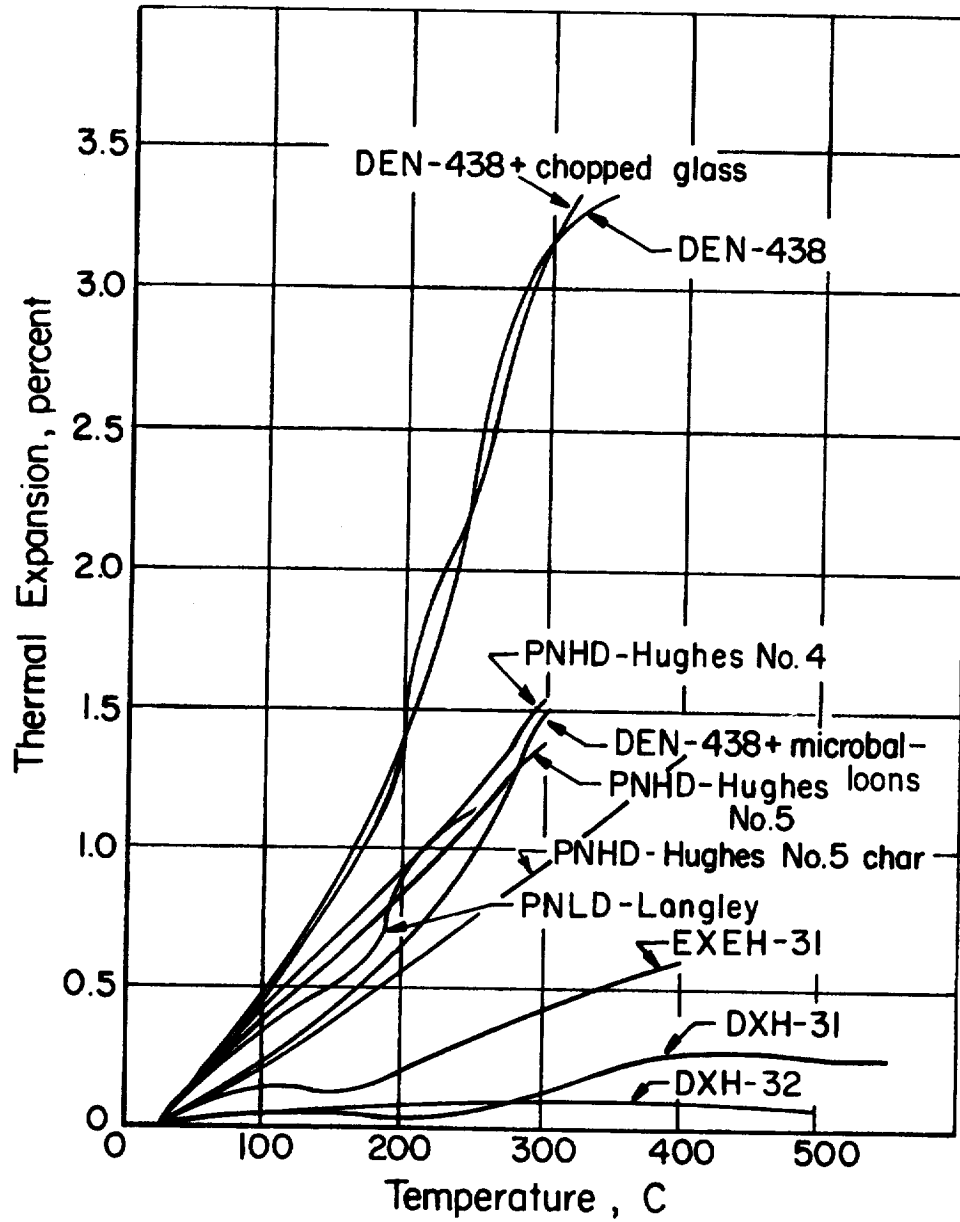


FIGURE 17. COMPARISON OF LINEAR THERMAL EXPANSIONS OF ABLATIVE POLYMER MATERIALS

(Heating Curves Only)

Figure 17 contains plots of linear thermal expansion versus temperature for the four materials. The experimental data points and visually-fitted curves are shown in Figure D-2 in Appendix D.

The DXH material appears to show effects of its hygroscopicity on heating. At about 100 C, the apparent loss of moisture interrupted the expansion. At about 200 C, expansion of the dry material resumed. The effect is more pronounced in the air-exposed specimen, as would be expected. The total linear expansion on heating to about 500 C appears to be in the range 0.25 to 0.30 percent. However, if the straight portions of the expansion curves from about 250 C upward are extrapolated back to room temperature (to compensate for the assumed moisture effect), the total expansion appears to be about 0.5 percent. In either case, the thermal expansion of the material in this temperature range is slight.

It is of interest to note that the maximum expansion of EXEH-31 is about twice that of DXH-31. The reason for this difference is not apparent, but may be related to the cross linking of the PBI.

Phenolic-Novolac Nylons

Linear-thermal-expansion measurements were made on the following phenolic-novolac nylon materials.

PNHD-Hughes No. 4

PNHD-Hughes No. 5

PNLD-Langley

PNHD-Hughes No. 5 charred at 400 C.

Details of the measurements, experimental data points and visually-fitted curves are in Figures D-3 and D-4 of Appendix D.

Figure 17 contains plots of linear thermal expansion versus temperature for the four materials.

Thermal Diffusivity

Thermal diffusivity, a transient heat-transport property, is numerically the ratio of thermal conductivity to the product of density and specific heat. Thermal diffusivities were calculated for materials for which values of thermal conductivity, specific heat, and density were measured. Densities used in the thermal-diffusivity calculations were room-temperature values adjusted for expansion or contraction with temperature change.

Calculated Thermal-Diffusivity Values

Figure 18 shows calculated (except for PNHD-Hughes No. 5 char, as discussed in next section) thermal-diffusivity values for selected DEN, DXH, PNHD, PNLD, and EXEH materials.

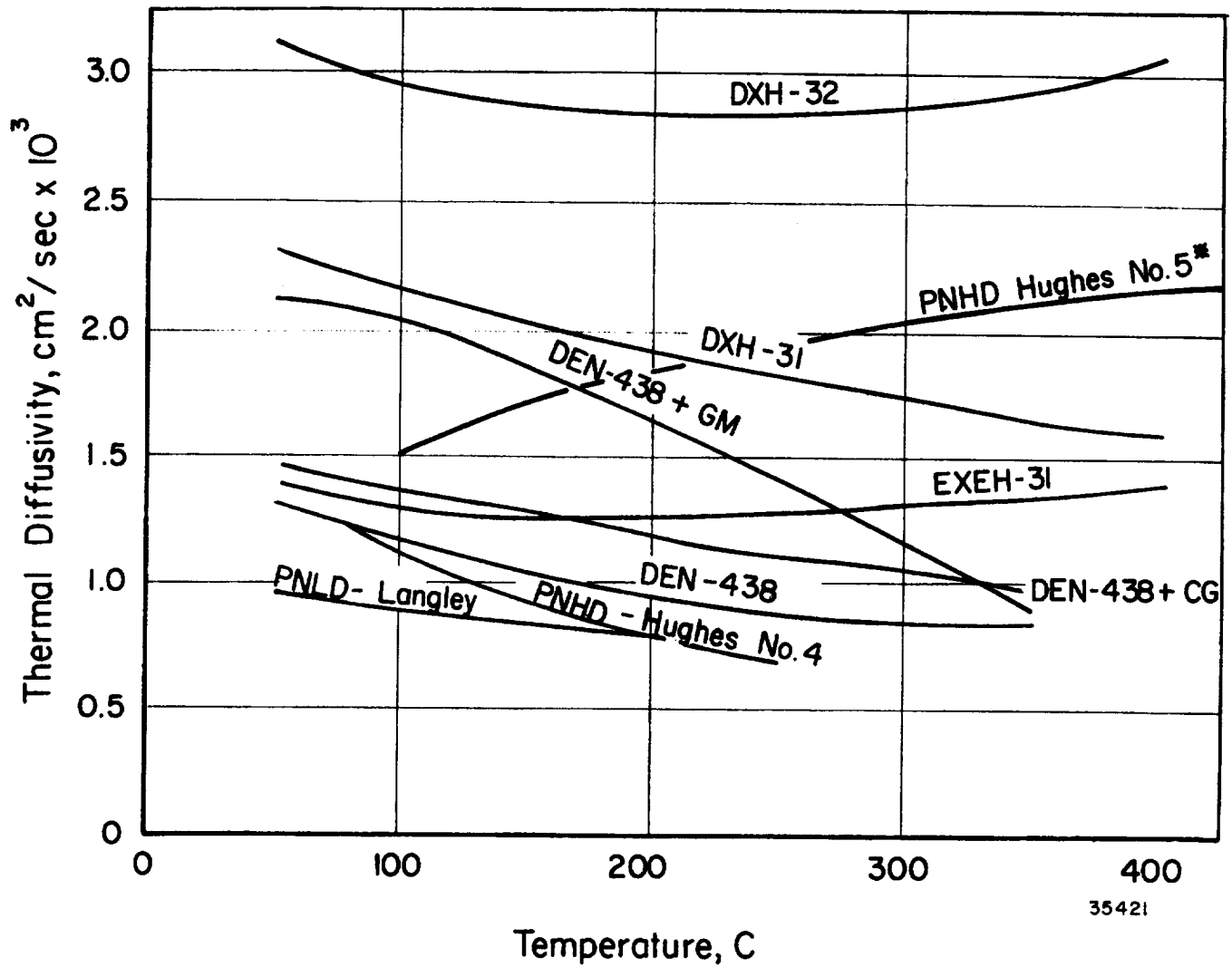


FIGURE 18. COMPARISON OF THERMAL DIFFUSIVITIES (CALCULATED) OF ABLATIVE POLYMER MATERIALS

*Measured by Laser Pulse Method

Measured Thermal Diffusivity
of PNHD-Hughes No. 5,
Precharred at 400 C

Thermal-diffusivity measurements were made on a specimen of PNHD-Hughes No. 5 precharred at 400 C.

These measurements were made using a transient, pulsed-laser method as described in Appendix E. The curve showing the results is included in Figure 18.

Table 4 shows the measured thermal-diffusivity values for Specimen PNHD-Hughes No. 5, precharred at 400 C, and thermal-conductivity values calculated as the product of thermal diffusivity, density, and specific heat. The computed conductivity values are considered somewhat questionable because the diffusivity measurements were made under conditions less than ideal for the method. The difficulty was that specimen thicknesses on the order of 0.010 inch appear to be required to achieve the favorable heat-pulse transient times called for under the boundary conditions of the pulsed-laser technique. The specimen used for these measurements was about 0.020-inch thick; thinner specimens were too fragile. In addition, the porous nature of the char introduces the possibility of some radiant-energy transfer locally, which could complicate results indicated by the technique.

TABLE 4. APPROXIMATE THERMAL DIFFUSIVITY AND THERMAL CONDUCTIVITY OF PNHD-HUGHES NO. 5 CHAR (400 C)

Temperature, C	Thermal Diffusivity, $10^3 \text{ cm}^2/\text{sec}$	Calculated Thermal Conductivity, $\text{mw}/(\text{cm})(\text{C})$
100	1.50	0.70
150	1.65	0.85
200	1.80	1.00
250	1.90	1.20
300	2.00	1.40
350	2.10	1.60
400	2.20	1.80

APPENDIX A

THERMAL-CONDUCTIVITY MEASUREMENTS

APPENDIX A

THERMAL-CONDUCTIVITY MEASUREMENTS

Thermal-conductivity measurements were made using an apparatus and method described in Appendix E, Apparatus and Methods for Making Thermophysical-Property Measurements.

Anhydride Cured, Epoxy NovolacsDEN-438

One specimen was 1 inch thick, the other, 1/2 inch thick. Each was instrumented with three thermocouples, so that it was possible to get two data points for each equilibrium condition. The thermal conductivity of the 1-inch-thick specimen was measured through the heating phase of one thermal cycle; that of the 1/2-inch-thick specimen was measured during several heating and cooling cycles. Measurements were made in the temperature range of 0 to 350 C.

Figure A-1 shows the experimental data for these specimens. Data for the 1-inch-thick specimen show slightly more scatter than those for the thinner specimen, which might be expected in measurements of this type for very-low-conductivity materials. Data on the first heating of the 1/2-inch-thick specimen (which was cut from a second 1-inch-thick piece) are considered to give the most reliable experimental data. After the first heating, the surface of the 1/2-inch-thick specimen became cracked to considerable depth. Subsequent runs were made with this specimen, with little evidence of an effect on conductivity as a result of the cracking or heat treatment.

DEN-438 + Chopped Glass

Thermal-conductivity measurements were made on one specimen of this material in the approximate temperature range 25 to 350 C. The technique is the same as that used for the 1/2-inch DEN-438 specimen. Figure A-2 shows the experimental data with a fitted curve. The addition of the glass fibers reverses the temperature dependence of this material. Instead of a gradual decrease from 2.2 to 2.0 mw (cm²) (C) as in the original polymer there is an increase from 2.20 to 2.75 over the temperature range 25 to 350 C.

DEN-438 + Glass Microballoons

The thermal conductivity of one specimen of this material was measured in the approximate temperature range 25 to 400 C. The experimental data are plotted in Figure A-3. The thermal-conductivity values for this specimen show more scatter than do those of any other specimen. The curve through these points is believed to be

the best representative of these data. The thermal conductivity of this material seems to have little temperature dependence and is significantly lower than those for the other two DEN-438 materials.

DXH-31

Thermal-conductivity measurements were made on two specimens of DXH-31 cut from a 3-inch-diameter by 1-inch disk. Each specimen was 3 inches in diameter by approximately 1/2 inch thick; both were similar, as far as is known, with regard to composition and porosity. The first specimen was measured in a helium atmosphere, the second in both helium and argon.

The first specimen of the DXH material measured was badly oxidized, especially on the hot side. The oxygen apparently came from the release of adsorbed air in fiber insulation in the apparatus as the insulation was heated. For this reason, data for this specimen are not included here. The fiber insulation was replaced by thermal radiation and convection shielding, and the specimen setup was changed before a second specimen was measured.

Figure A-4 shows the results of measurements made in helium and argon atmospheres, respectively. This second specimen showed no visible sign of oxidation after the measurements.

The significant difference in thermal conductivity of the DXH material as measured in helium and in argon reflects the large difference in thermal conductivity between the two gases. The value for helium is about 9 times as great as that for argon. Sufficient gas must have penetrated the specimen to cause the measured conductivity to be a composite of that for the DXH and for the gas.

DXH-32

The thermal conductivity of the pyrolyzed (650 C) DXH-32 specimen was measured using the ceramic heat-flow meter and an improved technique for mounting the thermocouples. The results of the measurements are shown in Figure A-5. The data-point groupings (three each) result from the measuring technique, wherein each point of a group is a calculated conductivity for the average temperature between two of three thermocouples in the specimen at one equilibrium point. The scatter in these points usually is caused by not knowing precisely enough the location of the point of contact between thermocouple junction and specimen. In this case, the locations of the curves were weighted according to the relative accuracy with which thermocouple positions were known.

Measurements of thermal conductivity were made in various atmospheres to investigate the effectiveness with which porosity in the material could be studied through these measurements. A preliminary evaluation of these data, based on the Loeb and the Maxwell-Eücken equations, gives values of porosity in reasonable qualitative agreement with microscopic examination.

Thermal-conductivity values obtained while cooling the DXH-32 specimen were in excellent agreement with those obtained during the heating cycle. This suggests that the specimen was stable throughout the measurement. In general, greater confidence is

placed in the data because it was possible to achieve a better conductivity match between the specimen and heat-flow meter, and also to make more precise measurements of thermocouple locations.

EXEH-31

Figure A-6 shows experimental thermal-conductivity data and a visually fitted curve for Specimen EXEH-31, a polybenzimidazole specimen which contains phenolic microballoons instead of silica microballoons.

Phenolic-Novolac Nylons

PNHD-Hughes No. 4

Figure A-7 is a plot showing experimental thermal-conductivity data for Specimen PNHD-Hughes No. 4 measured in argon.

PNHD-Hughes No. 5

The thermal conductivity of the PNHD Hughes No. 5 virgin polymer was measured over the temperature range 0 to 160 C, using a Pyroceram heat-flow meter. The data are presented in Figure A-8 and show the effect of vacuum, argon, and helium environments. There is essentially no difference between the sets of values measured in vacuum and in argon. However, the higher conductivity in helium indicates the effect of porosity in the material. The values measured in argon are very close to those found for the Hughes No. 4 material in the same atmosphere. The value of approximately 2.5 mw/(cm) (C) measured in helium is significantly higher than the 1.8 mw/(cm) (C) obtained with the No. 4 material, and may reflect a porosity difference between the two materials.

PNLD-Langley

Figure A-9 shows experimental data and visually fitted curves for thermal-conductivity measurements made on Specimen PNLD-Langley in argon and in helium.

NA-12 and NA-13

Figures A-10 and A-11 show experimental thermal-conductivity data and visually fitted curves for Specimens NA-12 and NA-13, respectively, over a temperature range from about 75 to 550 C. These composites were charred by the NASA-Ames laboratories by pyrolysis to 1000 C and were found to be stable to 500 and 800 C, respectively.

The reduced thermal-conductivity data, corrected for thermocouple location remeasurement after sectioning of the specimens, are presented in Figures A-10 and A-11. The numbers appearing with the set of three data points obtained at each equilibrium in the figures give the time order in which the equilibria were established. Equilibria are always established on a cooling cycle, in addition to those obtained on the heating

cycle, to check for possible material changes which may occur during the long soak periods required for the steady-state measurements. The environment during measurement was approximately 20-microns vacuum.

The data for NA-12 in Figure A-10 indicate that a reduction in the scatter about the mean of the three values in thermal conductivity obtained at each equilibrium occurs above the 250 C (nominal) Equilibrium 3. This generally indicates that a chemical reaction has either been initiated or run to completion within the specimen. The pyrolysis curve of Figure 5 (in body of report) for NA-12 indicates a steadily increasing evolution of volatiles with temperature from 25 C to about 250 C, where an inflection point occurred. This inflection point is evidence that further pyrolysis of the remaining phenolic was initiated at about 250 C, the poor definition of the inflection point indicating that the amount of material subject to pyrolysis at this temperature was relatively small. The scatter in the conductivity data for NA-12 up to 250 C can in part be attributed to the evolution of volatiles which, because of the temperature gradient through the specimen, evolve at different rates, depending on location relative to the hot face of the specimen. Since attainment of an equilibrium for measurement of the steady-state thermal conductivity requires 3 to 5 hours, Equilibrium 4 was established with less volatile production than occurred during Equilibrium 3. Also, this probably represented enough time to allow the pyrolysis reaction, begun at 250 C, to reach near-completion. The decrease in data scatter for Equilibria 4, 5, 6, and 7 suggests this interpretation. Therefore, comparison of the data obtained at Equilibria 3 and 6, with those for Equilibria 2 to 7 give a quantitative measure of the effect of the 250 C decomposition reaction on the effective thermal conductivity. The three data points each for Equilibria 6 and 7 are joined by dashed lines to aid the comparison. The 250 C reaction had the effect of lowering the thermal conductivity. This was probably due to an increase in specimen porosity caused by continued depletion of the phenolic. This could have been verified by porosity measurements performed before and after the thermal-conductivity measurements.

The pyrolysis curve of Figure 5 shows a second, more sharply defined inflection point at 530 C, with a large production of gas beyond this point. Undoubtedly, the thermal-conductivity measurements would have shown the effect of the further pyrolysis, had the measurements been extended above 530 C. However, since the NA-12 char showed such definite instability, further measurements would be of little value without recharacterizing the final char after measurement.

The data for Specimen NA-13 in Figure A-11 also present a problem in interpretation. The pyrolysis curve indicates that only a slow evolution of volatiles, much less than observed for Specimen NA-12, occurs from 25 to 1000 C, i.e., no further degradation of the material was to be expected during the thermal-conductivity measurements. The original conductivity data for NA-13 showed considerable scatter. Therefore, the specimen was inverted in the apparatus and rerun. The two sets of data are shown in Figure A-11, the three values of conductivity obtained at each equilibrium on the initial measurement cycle being joined by dashed lines in order to distinguish them from those obtained with the specimen reversed. It is seen that measurements with heat flow in opposite directions reverses the slope of the lines joining the three data points obtained at each equilibrium, and that the data for the two measurement series overlap to some extent. This reversal can be interpreted as a variation in conductivity through the thickness of the specimen. However, microstructure and general condition across the thickness appear uniform, and if the specimen was charred isothermally, it is difficult to assume a true variation.

Since NA-13 appeared to exhibit a relatively high conductivity, and because of the chance that the thermal conductivity may have varied across its thickness because of a variation in carbon crystallinity (if any crystallization occurred), this specimen was chosen for the X-ray analysis which was scheduled for one of the four phenolic-nylon specimens. Two samples, one for each face, were taken from NA-13 for this purpose. The results of these studies on NA-13 were given in Figures 10 through 13 in the body of the report. These studies indicated that the curve given in Figure A-11 best represents the material. This curve assumes that the conductivity is isotropic across the specimen, and to date, is a best representation of the property.

These results serve to illustrate the need for stable specimens and appropriate support measurements in order to gain maximum information from the steady-state thermal-conductivity measurements. The pyrolysis curve was essential in interpreting the data for Specimen NA-12. Measurement of the porosity of each specimen would allow comparison of the solid-matrix conductivities of the four composites. Also, the evolution of volatiles, as evidenced in the pyrolysis curves, illustrates a need for conditioning the specimens before measurement to eliminate the effect of the vaporization of volatiles on the thermal-conductivity measurements.

NA-14 and NA-15

Figures A-12 and A-13 show experimental data and visually fitted curves for Specimens NA-14 and NA-15. These composites were charred in the NASA-Ames laboratories to a maximum temperature of 1000 C. The environment during measurement was approximately 20-microns vacuum.

The pyrolysis curve for NA-14 shows a definite inflection point at 250 C, as was the case for NA-12. However, the overall gas production from NA-14 is relatively slight (comparable to that of NA-13 in magnitude), indicating that little of the material is available for the pyrolysis reaction initiated at 250 C. The extent of the pyrolysis was not great enough to show up in the thermal-conductivity data for NA-14 in the form of level change or pronounced data scatter as was the case for NA-12.

The pyrolysis curve for NA-15 indicates the considerable evolution of absorbed water and other volatiles with increasing temperature (comparable to that of NA-12 in magnitude). The 250 C inflection point is missing for NA-15; an inflection point is evident only at about 600 C, almost the upper limit of the thermal-conductivity measurements. The data for NA-15 exhibited a greater degree of scatter from the mean than did the data for the more stable Specimen NA-14.

Comparison of the magnitude of the pyrolysis curves for the four phenolics shows that NA-12 and NA-15 were similar in exhibiting relatively large gas evolution. This indicates that these two specimens were not well stabilized during their production. Specimens NA-13 and NA-14 produced similar pyrolysis curves which exhibited less gas evolution than observed for NA-12 and NA-15, indicating superior stability for Specimens NA-13 and NA-14.

Specimen NA-13 appears to have the highest conductivity of the four, but the data for NA-13 also exhibited the greatest degree of uncertainty of the four specimens. The conductivities of the four phenolics are seen to be quite similar throughout the temperature range of the measurements. Slight differences in specimen porosity could account for the differences among the four materials.

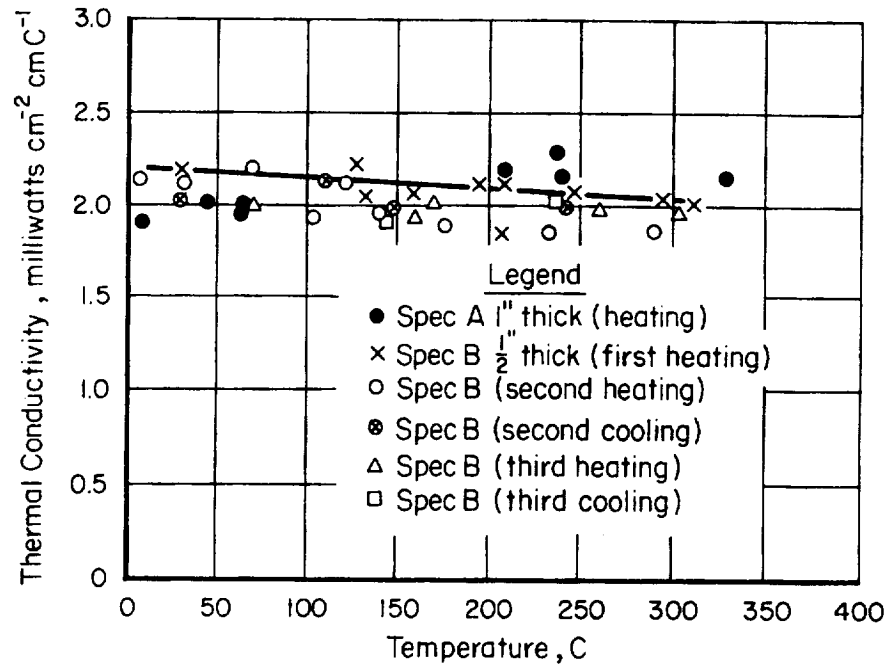


FIGURE A-1. THERMAL CONDUCTIVITY OF DEN-438

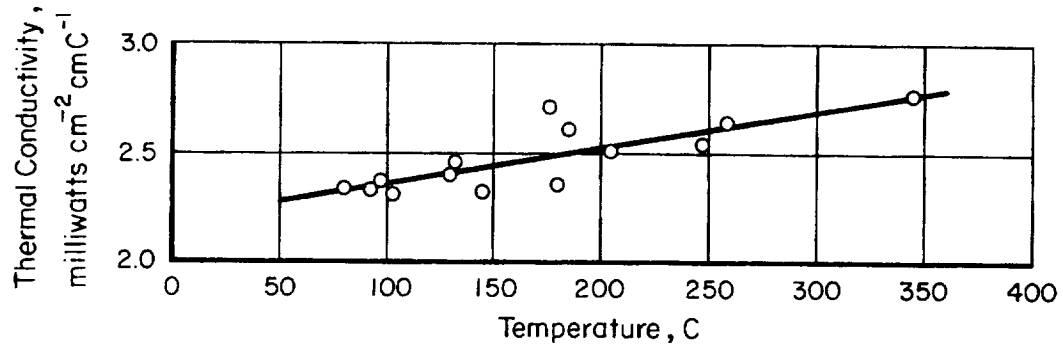


FIGURE A-2. THERMAL CONDUCTIVITY OF DEN-438 + CHOPPED GLASS

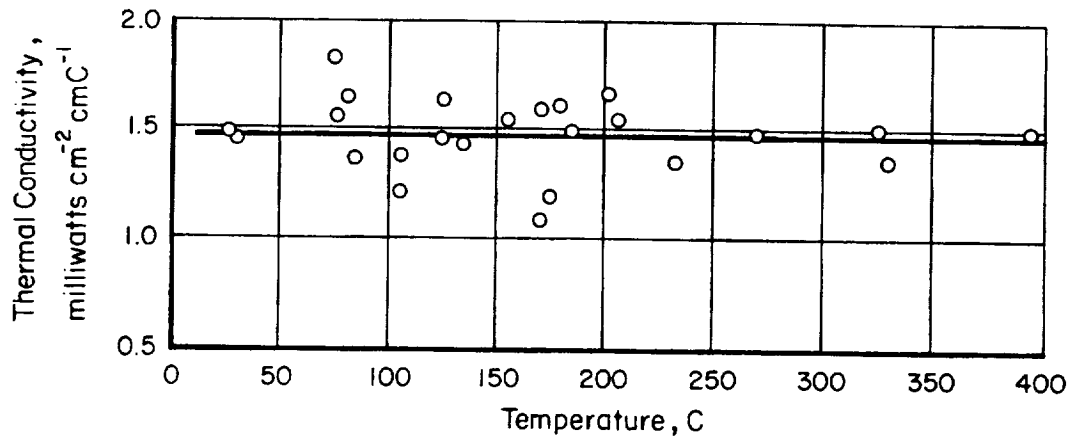


FIGURE A-3. THERMAL CONDUCTIVITY OF DEN-438 + GLASS MICROBALLOONS

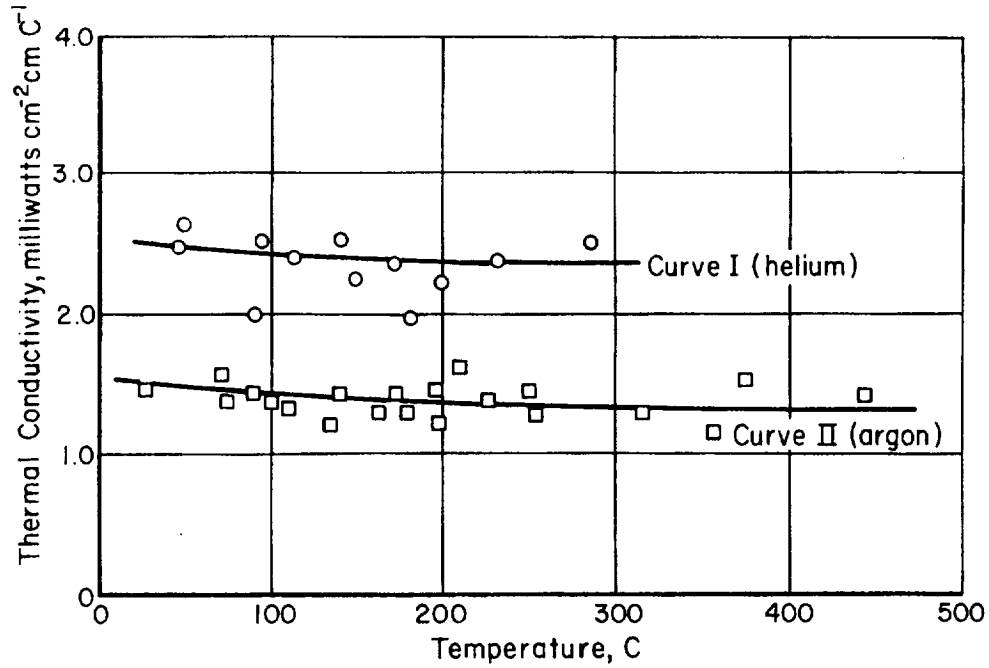


FIGURE A-4. THERMAL CONDUCTIVITY OF DXH-31

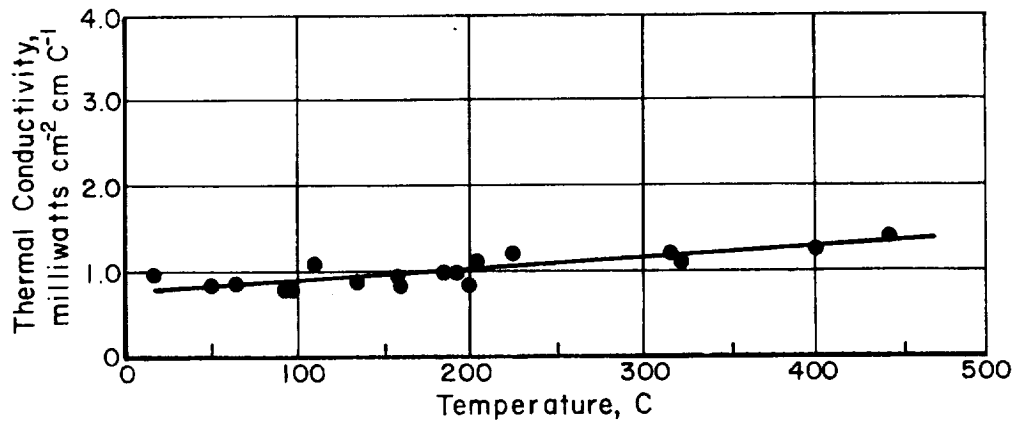


FIGURE A-5. THERMAL CONDUCTIVITY OF DXH-32 MATERIAL PYROLYZED AT 650 C

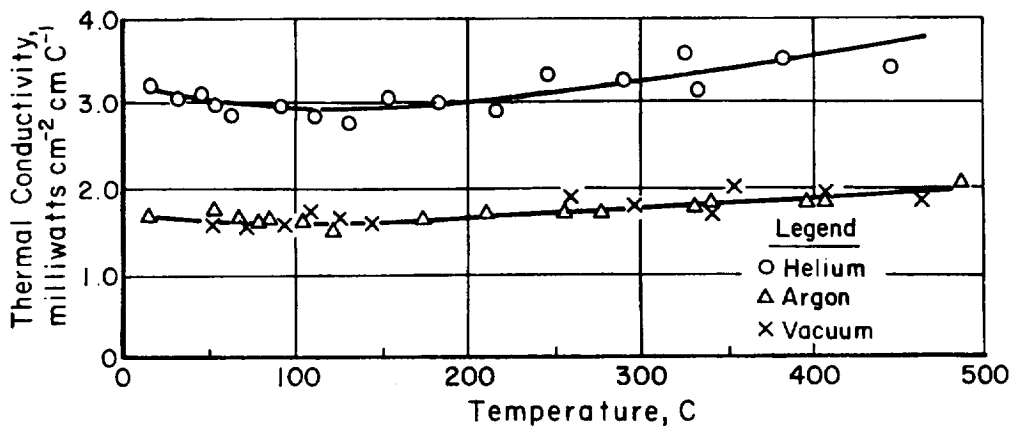


FIGURE A-6. THERMAL CONDUCTIVITY OF EXEH-31 MATERIAL

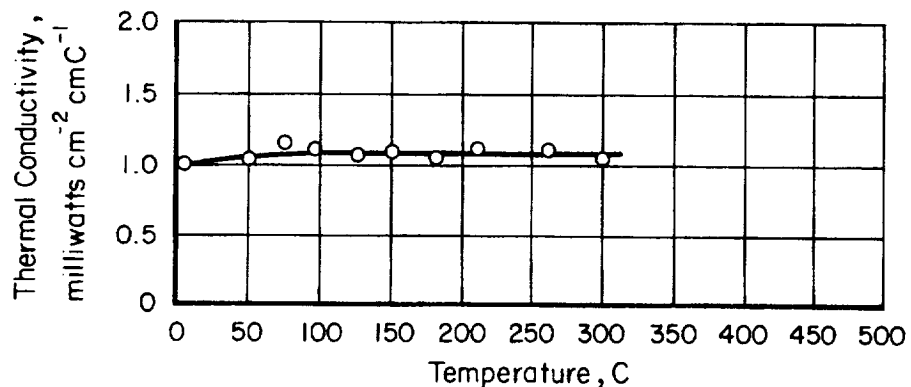


FIGURE A-7. THERMAL CONDUCTIVITY OF PNHD-HUGHES NO. 4 MATERIAL

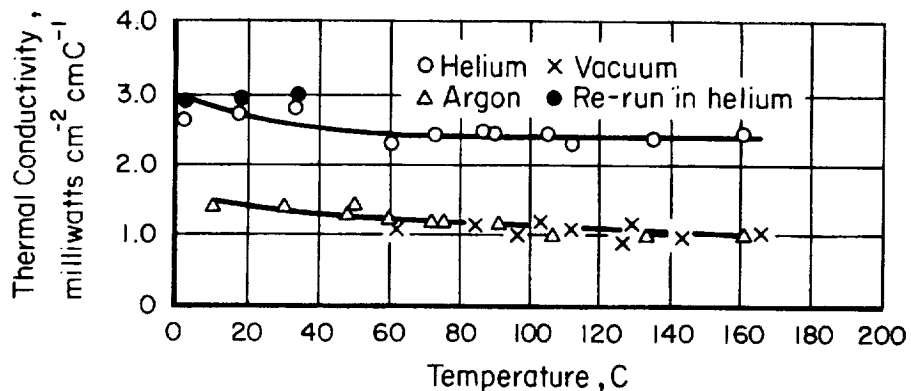


FIGURE A-8. THERMAL CONDUCTIVITY OF PNHD-HUGHES NO. 5 MATERIAL

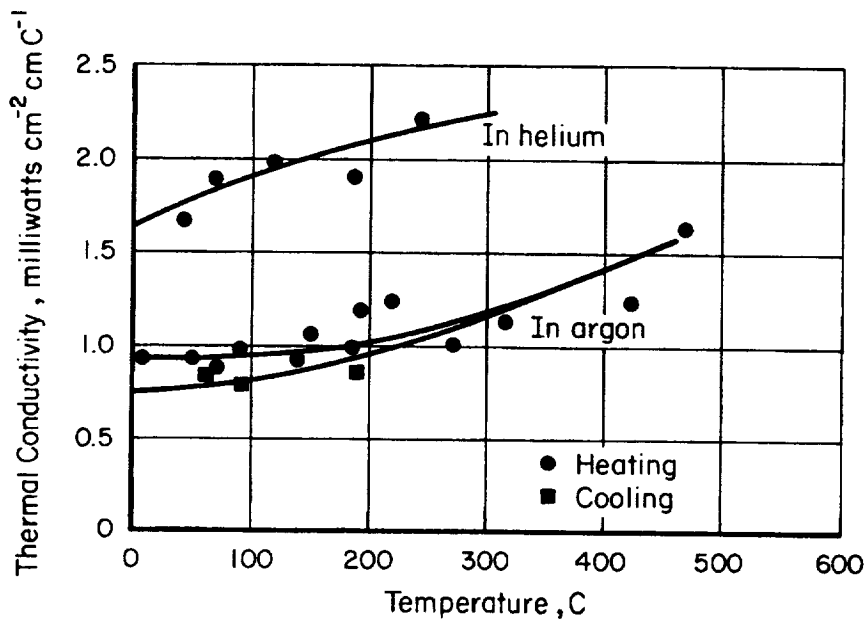


FIGURE A-9. THERMAL CONDUCTIVITY OF PNLD-LANGLEY MATERIAL

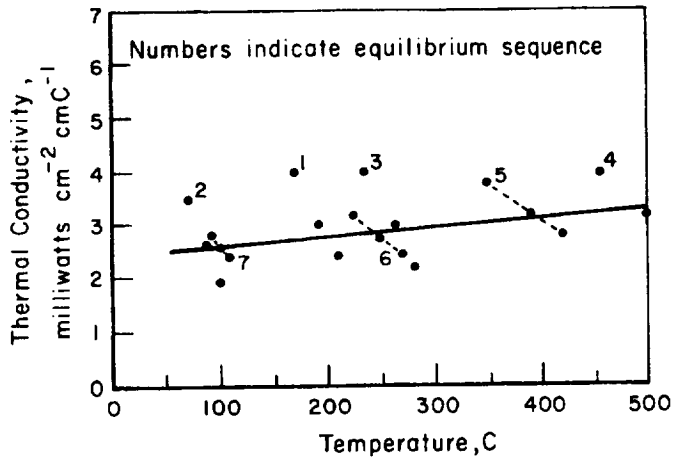


FIGURE A-10. THERMAL CONDUCTIVITY OF SPECIMEN NA-12

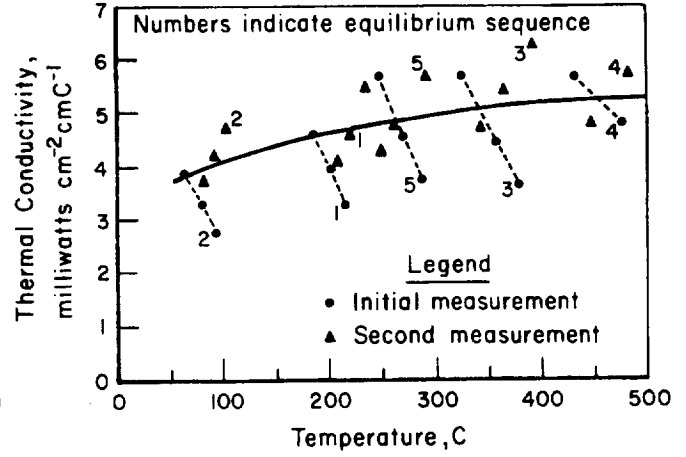


FIGURE A-11. THERMAL CONDUCTIVITY OF SPECIMEN NA-13

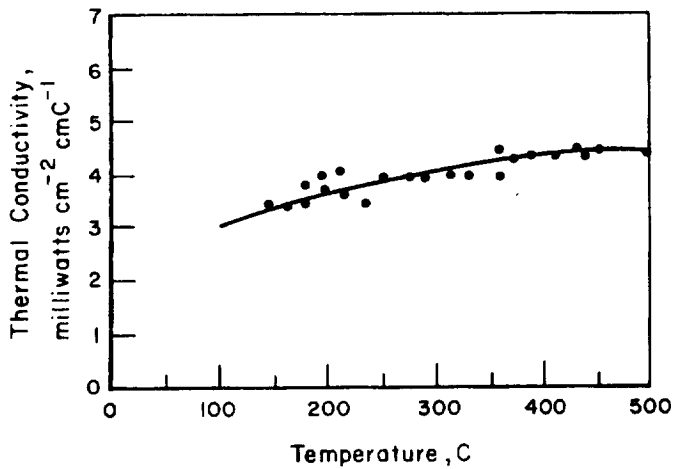


FIGURE A-12. THERMAL CONDUCTIVITY OF SPECIMEN NA-14

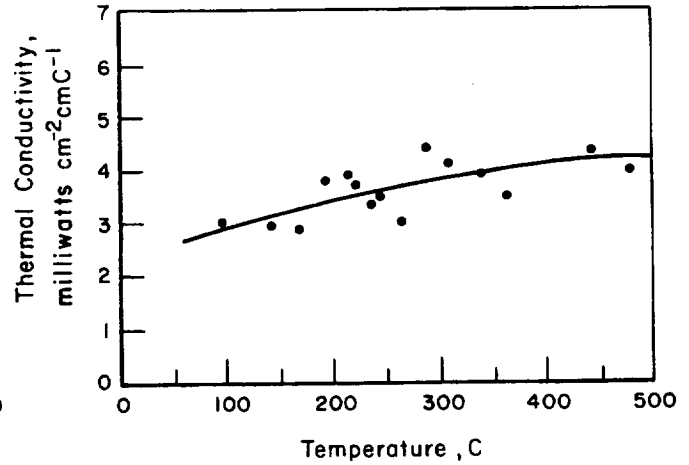


FIGURE A-13. THERMAL CONDUCTIVITY OF SPECIMEN NA-15

APPENDIX B

EFFECTS OF POROSITY ON THE THERMAL CONDUCTIVITY OF
A POLYBENZIMIDAZOLE CHAR MATERIAL

APPENDIX B

EFFECTS OF POROSITY ON THE THERMAL CONDUCTIVITY OF
A POLYBENZIMIDAZOLE CHAR MATERIALIntroduction

The fact that the thermal conductivity of an ablative material is sensitive to its porosity is well appreciated. The purpose of this study was to interpret some specific thermal-conductivity data obtained during this program in relation to the distribution of pore sizes existing in the material. The objective was twofold - firstly, to investigate the possibility of obtaining the effective porosity of the material from thermal-conductivity measurements made in different atmospheres, and secondly, to study the effect of various gases which may be present in the pores.

The material utilized in this investigation is the PBI system DXH-32 specimen which was charred at 650 C. For easy reference, the nominal composition of the virgin material is given below:

	<u>Percent</u>
Polybenzimidazole	65
Silica Microballoons	20
Alumina-Silica Fibers (Kaowool)	15

The thermal-conductivity of the DXH-32 char was measured in vacuum, argon, and helium environments.

The results of the analysis indicate that the two objectives cited above were approximately attained. However, the validity of the results rests upon the accuracy of the material model developed in the analysis, which in turn evolved from direct studies of the pore-size distribution. The data do not provide a broad enough basis from which to evaluate the rather voluminous number of theoretical models which may in fact be considered appropriate to this problem, and additional appropriate experimental data were not known to be available in the proper form. If appropriate, a comprehensive investigation of the problem is suggested which would provide the experimental data required to evaluate properly the various models.

Background

A porous material, such as DXH-32, can be looked upon as a composite of individual components, or phases, with the dense material representing a solid phase and the voids a second phase with its own peculiar properties. In order to evaluate the effect of variations in the properties of the separate phases on the overall, apparent conductivity of the conglomerate, a relation must be established between it and the conductivities of the individual phases through measurable material parameters. Many theories exist which accomplish this with varied degrees of success. Most were developed out of the

need to predict the conductivity of packed pebble beds, dispersions, porous rocks, and insulations, and for which considerable experimental data have been accumulated. (See Gorrington and Churchill^{(1)*} for a summary discussion of these problems.)

A material such as DXH-32 does not obviously fall into one of these categories, and a great deal of effort would be required to investigate all of the available theories which could perhaps be appropriate to this special case. Therefore, only two representative theories have been utilized in the analysis of the DXH-32 data. The first is the Maxwell-Eücken⁽²⁾ theory which represents a straightforward interrelation of the constituent phases and does not require a detailed model of the material for its interpretation, because of its neglect of interactions between individual pores comprising the void phase. The second is the Loeb⁽³⁾ theory which does require a detailed structural model of the material for its interpretation in terms of measurable quantities.

The two theories are outlined briefly here to provide some familiarity with the concepts involved. Since, as is found later, interpretation of the DXH-32 data requires the separation of the void fraction into two groups, the required relation will be written for a three-phase system. The Maxwell-Eücken relation will be seen to be linear with respect to the pore fractions and so represents one of the simplest approaches to relating the apparent conductivity to the conductivities of the three constituent phases. The Loeb relation will be seen to depend upon the particular arrangement of the three phases in a model of the material.

Maxwell-Eücken Relation for Three-Phase Material Spherical Pores

Consider a distribution of two groups of pores with radii a_1 and a_2 , with the number of pores of each radius in a sphere of radius b being denoted by n_1 and n_2 . This arrangement is illustrated in Figure B-1.

It is assumed that the volume with radius b is large compared with the dimension of the pore groups, but macroscopically small compared with typical specimen dimensions. That is, $a_1, a_2 \ll b \ll \text{specimen}$.

Assuming a constant temperature gradient throughout the sample, and that the spheres do not interact, the temperature at r , where $r \gg b$, due to the n_1 spheres of conductivity K^{P1} imbedded in a solid matrix of conductivity K^S , is given by:**

$$T_{n_1 a_1}(r) \propto \frac{ka_1^3 n_1}{r^3} \frac{K^S - K^{P1}}{(2K^S + K^{P1})} Z; Z = r \cos \theta \quad (1)$$

A similar equation holds for the n_2 spheres of radius a_2 of conductivity K^{P2} and the two temperatures are additive.

*References at end of Appendix.

**In the notation, a superscript on the conductivity denotes reference to a constituent phase.

Considering the entire volume b to be imbedded in a solid matrix of conductivity K^S and having an average conductivity, K , the temperature at r due to the sphere b will be given by:

$$T_b(r) = k Z + \frac{kb^3}{r^3} \frac{(K^S - K)}{2K^S + K} Z \quad (2)$$

We require that the temperature at r calculated by both methods be the same. Equating (1) and (2) thus gives:

$$\frac{K^S - K}{2K^S + K} = \xi_1 \frac{(K^S - K^{P1})}{(2K^S + K^{P1})} + \xi_2 \frac{(K^S - K^{P2})}{(2K^S + K^{P2})} \quad (3)$$

Where the pore fractions ξ_1 , ξ_2 are defined as volume fractions of the two porous phases by:

$$\xi_1 = \frac{n_1 a_1^3}{b^3} ; \xi_2 = \frac{n_2 a_2^3}{b^3} \quad (4)$$

Equation (3) relates the thermal conductivity of the solid phase K^S , to the measurable conductivity, K , and the conductivity of the porous phases, K^{P1} , K^{P2} , through the volume pore fractions, ξ_1 , ξ_2 . This equation neglects mutual influence of the pores upon each other. A higher order approximation which includes consideration of the mutual influence of the pores is considered later in the discussion. It is seen that in this case, the structure of the material must be considered in detail.

Loeb Relation for a Three-Phase Material

In this case, the one set of pores will be considered to be of much smaller dimension than the other: $a_2 \ll a_1$.

Consider a tube of material whose diameter is about the same as that of the large pores. This is illustrated in Figure B-2.

The conductivity, \bar{K} , of Section A in Figure B-2 can be evaluated as a parallel arrangement of small-diameter pores and solid material. This gives:

$$\bar{K} = K^S (1 - \xi_2^C) + K^{P2} \xi_2^C \quad (5)$$

where

K^S = conductivity of the solid phase.

ξ_2^C = area porosity fraction of the small pores in the cross section normal to the heat flux.

K^{P2} = conductivity of the small pores.

Next, the conductivity of the tube in Figure B-2 is calculated as a series arrangement of Sections A and B as:

$$\frac{1}{\bar{K}} = \frac{(1 - \xi_1^t)}{\bar{K}} + \frac{\xi_1^t}{K^{Pl}} \quad , \quad (6)$$

where

ξ_1^t = length porosity fraction of the large pores in the cross section of the tube parallel to the heat flow.

Finally, a parallel arrangement of the tubes of Figure B-2 with similar tubes composed entirely of the small pore - solid matrix composite of Section A completes this model of the material. The conductivity of this arrangement of tubes results in the apparent conductivity of the material parallel to the heat flow as follows:

$$K = \bar{K} (1 - \xi_1^C) + \frac{\xi_1^C}{\frac{(1 - \xi_1^t)}{\bar{K}} + \frac{\xi_1^t}{K^{Pl}}} \quad , \quad (7)$$

where

ξ_1^C = area porosity fraction of the large pores in a cross section normal to the heat flux

K = average (measurable) conductivity of the porous material.

For the special cases of evacuated pores and pores filled with helium, the three-phase formulas can be simplified if spherical pores* are assumed for both pore phases. The temperature limit is considered to be below that at which radiation transport across pores would become significant. Specifically:

In Vacuum, ($K^{Pl} = K^{P2} = 0$, $K = K(V)$).

$$\text{Maxwell-Eücken:} \quad \frac{K^S - K(V)}{2K^S + K(V)} = \frac{\xi_1}{2} + \frac{\xi_2}{2} = \frac{\xi}{2}$$

or

$$K^S = \frac{1 + \frac{\xi}{2}}{1 - \frac{\xi}{2}} K(V) \quad . \quad (8)$$

$$\text{Loeb:} \quad K(V) = \bar{K} (1 - \xi_1) \text{ and } \bar{K} = K^S (1 - \xi_2)$$

or

$$K^S = \frac{K(V)}{(1 - \xi + \xi_1 \xi_2)} \quad . \quad (9)$$

*Microscopic examination of Specimen DXH-32 revealed all of the observable pores to be spherical in shape. Therefore, this shape is used in the equations required for analysis of these measurements.

In Helium, $K = K(\text{He})$

$$\text{Maxwell-Eücken: } \frac{K^S - K(\text{He})}{2K^S + K(\text{He})} = \xi_1 \frac{K^S - K^{P1}}{2K^S + K^{P1}} + \xi_2 \frac{K^S - K^{P2}}{2K^S + K^{P2}} \quad (10)$$

$$\text{Loeb: } K(\text{He}) = \bar{K} (1 - \xi_1) + \frac{\xi_1}{\frac{\bar{K}}{K^{P1}}} \quad (11)$$

and

$$\bar{K} = K^S (1 - \xi_2) + K^{P2} \xi_2$$

Porosity Determination - Specimen DXH-32

In this section the porosity is calculated from the thermal-conductivity data. The results are then compared with the measured pore distribution.

Calculation of Specimen Porosity From Thermal-Conductivity Data

For the case of a single pore phase, Equations (9) and (11) can be combined, as can Equations (8) and (10), to allow calculation of the total porosity of the specimen from the thermal-conductivity data obtained in the vacuum and helium environments. Each theory gives a quadratic equation for total porosity in terms of the apparent conductivities in vacuum and helium, and the conductivity of the pores. The mode of energy transport across the pores was assumed to be ordinary gas conduction. Therefore, the conductivity of helium was used for the pore conductance in the helium environment, and zero in vacuum.

Table B-1 gives the results of the calculation of porosity utilizing the original-data curve in Figure B-3. The table shows that the calculated porosity varies with temperature, the variation being greater with the Maxwell-Eücken theory. Also, the porosity calculated at the lowest temperature is unrealistic.

To test the possibility that the variation of calculated porosity with temperature was due to data inaccuracy, the data curves were adjusted in the direction required to reduce the value of calculated porosity at the lower temperatures and to raise the value at the higher temperatures. Figure B-3 shows the initial and secondary curve adjustments, and Table B-1 gives the calculated porosities resulting from the two curve adjustments. The curve adjustments were kept within the ± 8 percent error band which applies to the original data curve. Table B-1 shows that adjustment of the data curves within the error of the data reduces the variation in the calculated porosity with temperature, the Loeb variation being less, but does not eliminate it altogether.

TABLE B-1. CALCULATED TOTAL PORE FRACTIONS FOR SPECIMEN DXH-32

Temperature, C	Thermal Conductivity, mw/(cm)(C)			Pore Fraction(a)		Pore Fraction(c)		Pore Fraction(d)	
	K(V)(a)	K(He)(a)	KHe(b)	M-E	Loeb	M-E	Loeb	M-E	Loeb
12.5	1.68	3.19	1.44	1.366	0.98	0.836	0.739	0.836	0.739
25	1.66	3.13	1.50	0.947	0.862	0.770	0.693	0.770	0.693
50	1.63	3.04	1.59	0.761	0.697	0.732	0.676	0.732	0.676
75	1.61	2.97	1.68	0.656	0.624	0.679	0.645	0.719	0.677
100	1.60	2.94	1.77	0.598	0.587	0.630	0.614	0.687	0.662
125	1.60	2.93	1.86	0.557	0.562	0.591	0.591	0.674	0.655
200	1.67	3.08	2.11	0.515	0.540	0.561	0.577	0.634	0.635
300	1.79	3.35	2.43	0.494	0.533	0.550	0.580	0.611	0.626
400	1.90	3.63	2.73	0.489	0.534	0.550	0.587	0.594	0.621

(a) Original data curves used, Figure B-3.

(b) Conductivity of helium as obtained from Peterson and Bonilla(4).

(c) Initial adjusted data curves used, Figure B-3.

(d) Secondary adjusted data curves used, Figure B-3.

Helium-Displacement Measurements of Total Porosity

In this measurement, the displacement of a volume of helium in a closed system containing a thoroughly outgassed sample of the material is recorded as a function of time. Since helium is inert and penetrates easily into almost all pores, the final value of helium displaced by the sample gives a measure of the volume occupied by the solid phase. A corresponding outgassed sample weight then gives the solid density.

A sample of DXH-32 was outgassed for 16 hours in a vacuum which ultimately reached 3.5×10^{-7} microns, and then exposed to helium. Figure B-7 gives the helium displacement-time history of the specimen. It is seen that an approach to equilibrium occurs only after 8 hours of exposure to the helium. The curve for time greater than 20 minutes or so approximates a first-order diffusion process, indicating that a portion of the void fraction of this material is made up of closed pores.

With the final value of displaced volume of 0.72 cc and a sample of weight 1.500 g, the solid density obtained from this measurement was 2.08 ± 0.04 g/cc.

Determination of total porosity was completed by measuring the apparent density of the material. This was done by measuring the weight of mercury displaced by a known weight of sample. A value of apparent density of 0.582 g/cc was obtained; this could be as much as 0.05 g/cc high owing to the hygroscopic nature of the material. The total porosity obtained was 0.72.

Mercury-Porosimeter Measurement of Pore-Size Distribution

In this measurement, a measured volume of mercury is forced under known pressure into the voids of the outgassed specimen. Assumptions of a contact angle for the mercury (140 degrees in this case), and that the mercury does not wet the material, allow relation of the pressure to the linear dimension for mercury flow at pressure. The result is specific cumulative pore volume versus a dimension representative of the pore size. If the pores are interconnected, the mercury pressure equilibrates across pore membranes and the membranes do not rupture. In the case that the mercury does not penetrate the closed pores, the mercury porosimeter test results in a measurement of open, or interconnected, porosity of the material. However, if the membranes of the closed pores are not strong enough to withstand the differential pressure attained in the measurement, the walls can crack and allow the mercury to enter. In this event, the dimension associated with the pressure at which the walls broke would not necessarily be representative of the size of the closed pore, although the total cumulative pore volume would in this case be a measure of the total porosity of the material. It is clear that mercury-porosimeter results require careful interpretation.

The results of mercury-porosimeter measurements performed on Specimen DXH-32 are given in Figure B-4. Microscopic examination of samples before and after the test showed that the silica microballoons, which were originally intact after the thermal-conductivity measurements, had been shattered, and that these spaces were filled by the mercury during the porosimeter test.* The microballoons were fragile and shattered easily upon the touch of a probe, so it was evident that the first plateau in Figure B-4, occurring at about 10^{-3} centimeter, included the breaking and filling of the microballoons. Microscopic examination indicated the microballoons to actually be about 10^{-2} centimeter in diameter. In order to verify the pore-size distribution below 10^{-3} centimeter, the porosimeter test was rerun on another specimen (the lower curve in Figure B-4), with much finer pressure increments being used in the 10^{-4} to 10^{-5} -centimeter region. The shape of the two curves agreed. This indicates the existence of real porosity down to at least 10^{-6} centimeter.

The highest total porosity obtained in the porosimeter measurements was $\epsilon = 0.757$. This is higher than the value obtained in the helium-displacement measurement. However, the helium-displacement data (see Figure B-7) indicate that the helium penetration was not quite complete at eight hours and the value of 0.72 from this measurement is probably low. Since the crushing experiment described next showed that the microballoons were filled with residual gases, and since microscopic examinations indicated complete filling of the pores by the mercury, it was felt that the value of total porosity obtained in the porosimeter test was most representative of the material. However, it must be noted that the compression of the residual gas released upon the crushing of the microballoons would show up as a continuously increasing and fictitious small pore distribution at the high-pressure limit.

*It should be noted that microscopic examination showed all visible pores to be highly spherical. This material could be expected to be isotropic in its thermal properties.

Residual Gas

Owing to the slow penetration of the helium into the pores of the DXH-32 specimen in the helium-displacement measurement, it was felt that any residual gases were probably trapped in the production of the microballoons. Samples of these gases were obtained by first outgassing a sample of DXH-32 and then, in a sealed system, crushing the sample and collecting part of the gas in a liquid-nitrogen-cooled condensing tube. A thermistor sealed into the glass system gave an indication of the pressure obtained as the sample was crushed. A sample was crushed by repeatedly lifting a glass-covered steel weight by means of a magnet and dropping it on the sample. The pressure increase indicated by the thermistor after each drop showed that the gas release was indeed due to the crushing action of the weight, and although the sample compacted so that only a small percentage of the microballoons were broken, enough gas was collected to allow a mass-spectrographic analysis.

The response of the thermistor after removal of the liquid-nitrogen cold trap indicated that at least two gas components were present. However, analysis of the gas was not performed since it would not have aided significantly the primary objective of interpretation of the thermal-conductivity data.

This experiment was useful in proving that the microballoons represented pores closed to some types of gases.

Interpretation of Direct Porosity Measurements

Direct measurements of porosity reveal, most importantly, the existence of a "large"-diameter pore fraction due in large part to the microballoons (the first plateau in Figure B-4 corresponding to a diameter of about 10^{-2} centimeter), followed by a distribution of smaller pores beginning at about 3×10^{-5} centimeter and continuing down to a diameter of at least 10^{-6} centimeter.

The mean free paths of helium and argon at 20 C are shown in Figure B-4 in relation to the distribution of pore diameters. In Figure B-4, it is seen that 51 percent of the cumulative specific pore volume lies in the region of pore diameters which are smaller than the mean free path of helium, and 33 percent lies below the mean free path of argon. It is reasonable that ordinary gas conduction within the pores is the primary mode of heat transfer for the pores of diameter larger than the mean free path. For the "smaller" pores, i. e., pores of diameter much less than the mean free path of helium molecules, heat transfer would occur by a different mode, free molecular interaction, which is a much less efficient process than ordinary gas conduction. Utilizing the formula of Schotte⁽⁵⁾ for the conductivity of helium as a function of the gas' specific-heat ratio, Prandtl number, mean free path, and accommodation coefficient of the pore surface, it is found that at the pressure and temperature range of these measurements, the mode of molecular energy transport within the pores becomes predominantly that of free molecular interaction for pore diameters of 10^{-4} to 10^{-5} centimeter, the former corresponding to an accommodation coefficient of 0.1 and the latter, 1.0. In this event, a significant percentage, about 33 percent of the total pore volume, could be unavailable for ordinary helium-gas conduction. For the case of argon, the smaller mean free path of argon lowers the pore-diameter limit for the onset of free molecular interaction by an order of magnitude to 10^{-5} to 10^{-6} centimeter.

Thus, at least in the case of helium, there seems to be a reasonable division of the pore-size distribution into two classes; one where ordinary gas conduction can occur, and the other where the pores are too small to allow ordinary gas conduction. The above discussion suggests that, as a first approximation, the division between the "large" and "small" diameter pore phases appropriate to helium can be made at about 10^{-5} centimeters. Figure B-4 shows that the cumulative specific pore volume down to 10^{-5} centimeter represents a pore fraction of 0.51. This pore fraction represents the fraction of the total pore volume that could support ordinary helium gas conduction.

Comparison of Calculated and Measured Pore Fractions

The equations used to calculate porosity from the conductivity data allowed for only a single value of porosity, i.e., all the pores were assumed to support ordinary helium-gas conduction. Therefore, the meaning of the values of porosity calculated from these equations must be examined in light of the established existence of two distinct pore phases.

The original equations [(8), through (11)] were written for a three-phase system. In the Loeb equation, the assumption was made that the small pores were much smaller than the large pores. That this is so is verified by the size division made above. The large-diameter pores were distributed over the range 10^{-2} to 10^{-5} centimeter, with a large fraction of these being due to the microballoons at about 10^{-2} centimeter, and the small-diameter pores were distributed over the range 10^{-5} centimeter on down. Thus, the picture of the tube utilized in the derivation of the Loeb equation is a reasonable one. No assumptions as to the pore group sizes were needed for the first order Maxwell-Eücken relations.

In the Maxwell-Eücken equations [(8) and (10)], three unknowns appear, namely the solid-phase conductivity and the two pore fractions. With the apparent conductivities in helium and vacuum known from the measurements and appropriate assumptions made to give the two pore conductivities, it is seen that there is not enough information available to permit the use of Equations (8) and (10) in the calculation of a pore fraction which is composed of two phases. Therefore, the porosities in Table 1 which were calculated from the first-order Maxwell-Eücken relation for a single pore phase have no obvious basis for interpretation. However, the Loeb equations [(9) and (11)] contain only two unknowns, the conductivity of the small pore-solid phase material and the large-diameter pore fraction. Therefore, a meaningful result is obtained when porosity is calculated as in Table B-1, that is, the pore fraction which is composed of pores that are of sufficient diameter to support ordinary helium gas conduction.

In Table B-1, the original and initial adjusted data used in the Loeb equations resulted in values of calculated porosity in helium which approached 0.53 and 0.58, respectively, in the high-temperature range of the measurements (above 100 C). These values are to be compared with the value of large-diameter pore fraction of 0.51 arrived at, in the section above, through consideration of the mode of molecular energy transport within the helium-filled pores. It is seen that fair agreement is attained between the two values. The greater temperature dependence of the calculated porosity below 100 C could not be satisfactorily explained. It could be due in part to the complicating influence of the residual gas present in the microballoons, or inadequacy of the theory. It should also be noted that, during measurement, only one equilibrium was obtained in the argon and vacuum environments below 50 C. This made definition of

conductivity versus temperature for these environments more difficult in the region below the apparent minimum, at about 100 C, than above (see Figure B-5).

It is obvious from Equations (9) and (11) that the calculation of effective porosity depends upon the existence of a measurable difference in apparent conductivity in two different environments. Since the conductivity measurements in an argon environment showed no discernible difference from those in vacuum, a porosity cannot be arrived at in the same manner as was done with a helium environment. On the other hand, the results of the previous section suggest that the total porosity of the material (corresponding to pore diameters down to 10^{-6} centimeter) may be available for ordinary argon-gas conduction. This question will be discussed later in terms of the material model.

Solid-Phase Conductivity of Specimen DXH-32

Equations (8) through (11) can be used to calculate the solid-phase conductivity of the specimen from both the thermal conductivity in vacuum and in helium.

In line with the division of the pores into two separate phases, "large" where ordinary gas conduction occurs and "small" where a less efficient mode of heat transfer predominates, the pore conductivity for the large pores will be assumed to be that of helium gas in the helium measurements, and zero in the vacuum measurements. For the small pores, the conductivity is assumed to be zero in both environments. Thus, the small pores are assumed to affect the apparent conductivity of the material only through the defects they cause in the lattice structure of the dense solid.

With these assumptions, Equations (8) and (10) give linear and quadratic equations, respectively, for the solid-phase conductivity, as do Equations (9) and (11). In each pair of equations, the large-diameter pore fraction can be regarded as a parameter in the determination of the solid-phase conductivity.

Calculations based on both theories showed that the agreement between the solid-phase conductivities as calculated from the helium and vacuum data depended upon the choice of the large-diameter pore fraction, total porosity being a fixed known quantity. A parametric study showed that the two values of solid-phase conductivity obtained from the two independent sets of data converged, on the basis of the average at four temperature points, at unique values of the large-diameter pore fraction.

Figure B-6 shows the results of these calculations. In all cases, the initial adjusted-data curves were used. It is seen that the values of the solid-phase conductivities calculated from the helium and vacuum data utilizing the Loeb theory became identical at $\xi_1 = 0.61$, and those calculated utilizing the Maxwell-Eücken theory, at $\xi_1 = 0.67$. These large-diameter pore fractions are shown in perspective with the pore-size distribution in Figure B-4.

Table B-1 shows that the Loeb value of $\xi_1 = 0.61$ obtained from Figure B-6 corresponds closely to the porosity calculated from the Loeb theory from 100 to 400 C utilizing the initial adjusted helium and vacuum data curves. This was to be expected since the same data were used in both calculations, and three of the four temperature points used in calculating the average deviations displayed in Figure B-6 were at 100 C and above. Similar correlation of the Maxwell-Eücken value of $\xi_1 = 0.67$ from

Figure B-6 with the calculated porosities of Table B-1 is not expected, since the porosities obtained from the first-order Maxwell-Eücken relation bore no relation to a two-phase pore model.

The solid-phase conductivities for Specimen DXH-32 obtained from the two theories at the respective values of large-diameter pore fractions where convergence was obtained are presented in Table B-2. The data and porosity values used in the calculations are listed in the table. It is obvious from Table B-2 that the two theories do not give comparable values for the solid-phase conductivity, the Maxwell-Eücken values being greater than the Loeb values by almost a factor of 2. It may be noted in Figure B-6 that the difference between the solid-phase conductivities calculated from the conductivity data obtained in helium and vacuum became identical for the two theories at a large-diameter pore fraction of about 0.71. At this point, the solid-phase conductivities obtained from the Maxwell-Eücken theory are still larger than those from the Loeb theory by the same factor.

TABLE B-2. SOLID-PHASE CONDUCTIVITY FOR SPECIMEN DXH-32

Temperature, C	Thermal Conductivity, mw/(cm)(C)						
	KHe	K(He) ^(a)	K(V) ^(a)	Loeb ($1 = 0.61$)		M-E ($1 = 0.67$)	
				KS ^(b)	KS ^(c)	KS ^(b)	KS ^(c)
12.5	1.44	3.11	1.77	5.71	5.33	11.29	10.04
25	1.50	3.07	1.73	5.49	5.21	10.81	9.81
50	1.59	3.01	1.63	5.16	4.91	10.08	9.25
75	1.68	2.96	1.57	4.88	4.73	9.42	8.91
100	1.77	2.95	1.56	4.72	4.70	9.00	8.85
125	1.86	2.95	1.56	4.59	4.70	8.64	8.85
150	1.94	3.00	1.59	4.59	4.79	8.57	9.02
200	2.11	3.16	1.65	4.74	4.97	8.77	9.36
250	2.27	3.30	1.69	4.86	5.09	8.88	9.59
300	2.43	3.43	1.73	4.97	5.21	8.95	9.81
400	2.73	3.71	1.81	5.24	5.45	9.26	10.27

(a) From initial adjusted curves of Figure B-3.

(b) Calculated from helium data with $\zeta = 0.76$.

(c) Calculated from vacuum data with $\zeta = 0.76$.

Effect of a Gas on the Apparent Thermal Conductivity

The crushing experiment showed that the microballoons contained residual gas which remained within the microballoons after 20 hours in a high-vacuum environment. The curve of helium displacement versus time in Figure B-7 indicates a relatively rapid filling of the open pores by the helium, followed by a slow diffusion of helium into the closed pores. Apparently, the microballoons represented closed pores which certain gases could not easily penetrate. The presence of such a selective structure as the microballoons requires that the particular gas comprising the environment be given individual consideration as to its ability to enter the closed pores.

Two cases are possible. One arises when the gas can enter the closed pores. Here, the large-diameter pore fraction representing pores large enough to support ordinary gas conduction increases as the density of the closed pores is increased, and a concurrent increase in apparent conductivity might be expected. The other case arises if the gas cannot penetrate the closed pores. In this event, the large-diameter pore fraction might be decreased by an increase in closed-pore density, and the apparent conductivity of the material could be expected to also decrease. Both cases will be examined.

Case A: Large Diameter Pores Open to the Environmental Gas. In this case, the gas, given enough time, can enter the closed pores. Figure B-7 indicates that helium certainly penetrated the microballoons in DXH-32. It is likely that the argon did also since it is monatomic and inert.* The Loeb and Maxwell-Eücken theories will be used to predict the apparent conductivity for a given total (open plus closed) porosity, with the pore fraction open to the gas being of sufficient dimension to support ordinary gas conduction as a parameter. The residual gas actually present in the closed pores is neglected. For these calculations, Equation (10) and (11) are used, with the conductivity of argon as the large-diameter pore conductance. The appropriate solid-phase conductivities were obtained from the data of Table B-2. Equations (10) and (11) are repeated for convenience:

$$\text{Maxwell-Eücken, argon: } \frac{K^S - K(A)}{2K^S + K(A)} = \xi_1 \frac{K^S - K^A}{2K^S + K^A} + \frac{\xi_2}{2} \quad (12)$$

$$\text{Loeb, argon: } K(A) = \bar{K} (1 - \xi_1) + \frac{\xi_1}{\frac{(1 - \xi_1) \xi_1}{\bar{K}} + \frac{\xi_1}{K^A}} \quad (13)$$

$$\bar{K} = K^S (1 - \xi_2)$$

where

K^S = solid-phase conductivity obtained from the vacuum and helium data in Table B-2

$K(A)$ = apparent conductivity of the porous specimen in argon

K^A = conductivity of argon gas [Reference (4)]

ξ_1 = large-diameter pore fraction which is open to argon and can support ordinary gas conduction.

ξ_2 = small-diameter pore fraction which has zero conductivity in the presence of the argon; $\xi_2 = \xi - \xi_1$.

*The measurement represented in Figure B-7 shows that almost complete helium penetration of the microballoons required about 8 hours. It is reasonable that argon penetration would require more time. However, the total time in environment during the conductivity measurements was in excess of 48 hours.

Figure B-8 shows the thermal conductivity calculated on the basis of the conductivities of the three constituent phases at the extreme temperatures attained in the actual measurements, 25 and 400 C. The ordinate is the difference between the conductivities calculated from Equations (12) and (13) and the measured values from the initial adjusted vacuum-data curve, which appear in Table B-2. The total porosity is fixed at 0.76, the approximate measured value for DXH-32.

Since the error in the conductivity measurements must be considered in relation to the predicted conductivities, the error band of ± 8 percent is indicated in Figure B-8.

The conductivity measurement in argon provides the only available experimental point of comparison for the two material models considered in this analysis. The two argon curves of Figure B-8 arising from the Loeb model show that the difference between the predicted argon and measured vacuum conductivities becomes zero at large-diameter pore fractions of about 0.70 and 0.72 for the two temperatures. This prediction is to be compared with the following two results discussed earlier. The first is that no difference between the conductivity measured in argon and vacuum was discernible. Second, molecular theory produced the estimate of the pore-diameter lower limit (below which free molecular interaction dominates) of 10^{-5} to 10^{-6} centimeter, the latter value corresponding to the total pore fraction of 0.76. Therefore, there is agreement between the Loeb theory prediction of zero difference at a large-diameter pore fraction close to 0.72 with experiment and the estimate from molecular theory. On the other hand, it is seen that the Maxwell-Eücken theory predicts an apparent conductivity in argon about 11 percent higher at 25 C and about 22 percent higher at 400 C at the large-diameter pore fraction of 0.66 than that in vacuum. These differences would have been detected in the ± 8 percent accurate conductivity measurements.

The form of the Maxwell-Eücken relation given in Equation (3) was obtained by neglecting the influence of the pores upon each other. Intuitively, this would seem to become a poor assumption as the porosity increases. The DXH-32 specimen was a highly porous specimen with closely spaced, spherical pores of various diameters. In order to observe the effect on the Maxwell-Eücken predicted solid-phase conductivity when pore-pore interactions are considered, the Rayleigh⁽⁷⁾ formulation is considered here. In this model, the spherical pores are arranged in a specified pattern and the average, measurable conductivity of the pore-solid composite is obtained in terms of a series of sums giving, in increasing orders of approximation, the influence of the pores on the average conductivity. The first approximation is just the Maxwell-Eücken relation. The second approximation, applicable for a single pore phase is:

$$\frac{K}{K^S} = 1 - \frac{3\xi}{\frac{2K^S + K^{P1}}{K^S - K^{P1}} + \xi - 0.523 \frac{K^S - K^{P1}}{4/3K^S + K^{P1}} \xi^{10/3}} \quad (14)$$

The value of the numerical coefficient of $\xi^{10/3}$ in Equation (14) depends upon the structural arrangement assumed for the pores. The contribution of this term is small relative to the first term in the denominator, however, and the value used in equation (14) will show the trend to be expected.

To apply this second approximation to the DXH-32 data for comparison with the previous first-order results for the three-phase model, the same approach will be used as for the Loeb equation. Consider Equation (14) to give the measurable conductivity K in terms of the large diameter pore fraction ξ_1 with large pore conductivity K^{P1} , and a

small-pore/solid-phase conductivity \bar{K} . The latter quantity will be related to the solid-phase conductivity K^S and the small-diameter pore fraction ξ_2 with zero conductivity as in Equation (15). Since ξ_2 is small, the first-order approximation of Rayleigh, i. e., the Maxwell-Eücken relation, is valid for the relation between \bar{K} and K^S . That is:

$$\frac{\bar{K}}{K^S} = 1 - \frac{3\xi_2}{\frac{2K^S + K^{Pl}}{K^S - K^{Pl}} + \xi_2} = \frac{1 - \xi_2}{1 + \xi_2/2} \quad (15)$$

To use Equation (14) with the conductivity data of the specimen obtained in helium, the following substitutions are required:

- $K = K(\text{He})$ = measured apparent conductivity in helium
- $K^{Pl} = K^{\text{He}}$ = conductivity of helium
- $\xi = \xi_1$ = large-diameter pore fraction
- $K^S = \bar{K}$ = small pore/solid phase conductivity

In this case, Equation (14) gives a cubic for the small-pore/solid-phase conductivity \bar{K} . At a temperature of 25 C, with the conductivities of the specimen and helium from the data of Table B-2, Equation (14) gives: $\bar{K} = 7.84$. With the small-diameter pore fraction of 0.09 ($\xi = 0.76$, $\xi_1 = 0.67$), Equation (15) gives $K^S = 9.01$. This value of solid-phase conductivity is to be compared with that obtained in Table B-2 from the Maxwell-Eücken relation, utilizing the helium-environment conductivity data, $K^S = 10.81$.

Equation (14) reduces to a quadratic in \bar{K} when the conductivity data obtained in vacuum is utilized. With the data of Table B-2 providing the specimen conductivity in vacuum at 25 C, Equation (14) gives $\bar{K} = 7.22$. With the pore fractions as given above, Equation (15) gives $K^S = 8.29$. The latter value is to be compared with that obtained in Table B-2 from the Maxwell-Eücken relation utilizing the vacuum-environment conductivity data, $K^S = 9.81$.

It is seen that the second approximation which includes the first-order effect of pore-pore interactions lowers the value of solid-phase conductivity below that given by the Maxwell-Eücken relation. As with Equation (7), a model had to be assumed in applying Equation (14) to a three-phase model.

For the sake of comparison, the Rayleigh theory was applied to predict the apparent conductivity in argon at 25 C. The result is also shown in Figure B-8. Since a series arrangement of large-diameter pores and a parallel arrangement of small-diameter pores is used as in the Loeb theory, the results are similar: a maximum in apparent conductivity for a large-diameter pore fraction of about 0.4, and a difference between predicted and measured conductivities of zero at about 0.73. The Maxwell-Eücken values of solid-phase conductivity from Table B-2 were used in the Rayleigh formula. These are somewhat higher than the values which would have been obtained from the helium and vacuum data as was done in the single calculation, but the trend as obtained in Figure B-8 would have been the same.

The model upon which Equation (13) is based, (Figure B-2), depends upon the presence of a significant number of small-diameter pores to produce a well-defined small-pore/solid-phase volume of material in series with each large-diameter pore.

For values of large-diameter pore fraction near 0.76, the few small-diameter pores remaining invalidate the tube geometry of Figure B-2 and thus Equation (13). In order to estimate the lower limit for the small-diameter pore fraction below which Equation (13) is invalid, the apparent conductivity for a two-phase, parallel arrangement of dense solid and large-diameter pores was calculated at 25 C and 400 C. The Loeb values of solid-phase conductivities from Table B-2 and the conductivities of argon and helium for the pores were used. These four curves are also shown in Figure B-8. Each curve corresponds to a Loeb curve at the same temperature and with the same gas, and represents the maximum apparent conductivity which could be obtained in the three-phase model as the large-diameter pore fraction proceeds to become the total pore fraction* (see, e. g., Woodside and Messmer⁽⁶⁾).

The difference between the predicted apparent conductivity with helium present in the pores as given by Equation (13) and the measured conductivity in vacuum is also given in Figure B-8. It is apparent that the two-phase maximum curves limit the applicability of these two curves to large-diameter pore fractions below about 0.61. Likewise, the Maxwell-Eücken curves are limited to values below about 0.66, and the Loeb, argon curves to below about 0.72.

Figure B-8 shows that the Loeb relation predicts a maximum in the apparent conductivity in argon which is 37 percent above that in vacuum. This suggests that a gas with a conductivity of the order of argon could significantly raise the apparent conductivity if the pore fraction supporting ordinary gas conduction is a suitable percentage of the total porosity. These predictions cannot be tested by experimental results at present, since sufficient data are not available.

Another feature of the data which is illustrated in Figure B-8 is the difference between the predicted conductivity in vacuum as given by Equation (13) and the measured value for the two temperatures, 25 and 400 C. The large-diameter pore fraction at which they become equal is seen to be 0.61, which is the same as that previously found to be effective in supporting ordinary helium-gas conduction. This is expected, since this value was originally obtained by using the large-diameter pore fraction as a parameter in obtaining agreement between the solid-phase conductivities calculated independently from the helium and vacuum data. The same theory requires the large-diameter pore fraction for the case of argon to be close in value to the total specimen porosity. It is reasonable that the effective large-diameter pore fraction should depend on the mean free path of the particular gas present in the pores, but the value of this fraction found above for the case of a vacuum environment does not have an obvious interpretation. The confusion possibly is due to overuse of the limited amount of experimental data.

Case B: Large-Diameter Pores Closed to the Environmental Gas. In this case, the large-diameter pores are closed to the gas comprising the environment. For example, microballoons free of residual gas could conceivably accomplish this for an environment of heavy, polyatomic gases. For the Maxwell-Eücken relation, zero conductivity for the large-diameter pores and the conductivity of the gas for the remaining small-diameter fraction change Equation (10) to (16) which is given below. Since the large-diameter pores are in series with the small-pore/solid-phase material in the Loeb equation, the macroscopic tubes of material pictured in Figure B-2 containing large-diameter pores will not contribute to the apparent conductivity, and Equation (11) is changed to Equation (17) below.

*The maximum apparent conductivity is given by the equation:

$$K(\text{max}) = \zeta K(\text{gas}) + (1 - \zeta) K(\text{solid}).$$

Maxwell-Eücken, argon

$$\frac{K^S - K(A)}{2K^S + K(A)} = \frac{\xi_1}{2} + \xi_2 \frac{K^S - K^A}{2K^S + K^A} \quad (16)$$

Loeb, argon $K(A) = \bar{K} (1 - \xi_1)$ and $\bar{K} = K^S (1 - \xi_2) + K^A \xi_2$,

so that

$$K(A) = (1 - \xi_1) [K^S (1 - \xi_2) + K^A \xi_2] \quad (17)$$

where

K^S = solid-phase conductivity obtained from the vacuum and helium data in Table B-2

$K(A)$ = apparent conductivity of the porous specimen in argon environment under the assumption that argon represents the gas excluded from the large-diameter pores

K^A = conductivity of argon, representative of real, excludable gas

ξ_1 = large-diameter pore fraction which is closed to the gas; the conductivity of these pores is zero

ξ_2 = small-diameter pore fraction which is open to the gas and can support ordinary gas conduction; $\xi_2 = \xi - \xi_1$; the conductivity of these pores is that of argon.

The conductivity for the gas is assumed to be that of argon to allow calculations comparable to Case A. Since the heavy gases have small mean free paths, the small-diameter pore fraction will be assumed to support ordinary gas conduction. This assumption is supported by the argon results of Case A.

Equations (16) and (17) are plotted in Figure B-9. The ordinate is the difference between the predicted apparent conductivity in argon and that measured in vacuum. The abscissa is the large-diameter pore fraction from which the argon is excluded.

Also appearing in Figure B-9 are the limiting, maximum differences in conductivity prescribed by a two-phase system of small-diameter pores in parallel with the dense material. As in Case A, these curves represent the maximum values attainable when the large-diameter pore fraction is near zero so that the material is close to being a two-phase system. The appropriate equation for this system is:

$$K(\text{max}) = (\xi - \xi_1) K(\text{gas}) + \left(1 - (\xi - \xi_1)\right) K(\text{solid}) \quad .$$

It is seen in Figure B-9 that the Maxwell-Eücken curves predict a linear decrease of apparent conductivity with increasing large-diameter pore fraction. As the figure indicates, the applicability of these curves is limited to large-diameter pore fractions above 0.1 by the maximum two-phase curves. The Loeb equation predicts a maximum associated with the series-parallel arrangement of large- and small-diameter pores. The maxima for two temperatures are indicated on the curves and were found by differentiating Equation (6).

It may be noticed that the Loeb equation predicts a difference of zero for a large-diameter pore fraction of about 0.1 and again at about 0.62. However, the zero occurring at 0.1 in Figure B-9 cannot apply to the actual argon measurement of DXH-32. This is evident from the data of Figure B-4 where it was shown that microballoons represent the first plateaus in the pore distributions and, therefore, correspond to a large-diameter pore fraction of at least 0.20. Likewise, the zero at 0.62 is ruled out for the argon measurement since it is certain that this percentage of the total porosity is not unavailable to argon. These calculations, therefore, support the assumption in Case A that the argon did indeed penetrate the microballoons.

The Loeb curves of Figure B-9 may represent the case of a heavy, polyatomic gas which cannot penetrate the closed pores and which has a conductivity of the order of that of argon. In this event, Figure B-9 shows that the effect of the complex gas is minimal if the fraction of the large-diameter pores which excludes the gas is near either 0.1 or 0.62. If a light gas such as hydrogen or helium is present along with the polyatomic gas, and the large-diameter pores are open to the light gas while the remaining fraction of small-diameter pores are unable to support ordinary light-gas conduction, the results of Case A can be applied concurrently to estimate the effect of the gas mixture. The Loeb curves of Figure B-8 for helium show that the light-gas contribution to the apparent conductivity is also minimized at a large-diameter pore fraction of 0.1 but not at 0.62. Therefore, the present calculations based on the Loeb formulation correctly predict that the gas-conduction contribution to the apparent conductivity is negligible when the large-diameter pore fraction is kept to a small fraction of the total porosity - less than 13 percent. This may be compared to the actual DXH-32 specimen where the large-diameter pore fraction for helium-filled voids was 80 percent of the total porosity and which resulted in a doubling of the apparent conductivity in helium over that in vacuum. For other values of pore-fraction ratios, the model allows for the possibility of a significant increase in the apparent conductivity due to light or complex gases within the pores.

Conclusions

The first objective of this study was to determine whether effective porosity can be calculated from thermal conductivity measured on char materials in various environments. The analysis shows that such calculations require the formulation of a structural model for the materials. This necessitates direct measurement of the pore size, shape, and distribution. Since these measurements, along with molecular theory, provide an estimate of the effective pore fraction appropriate to the environmental gas, calculation of porosity from conductivity data is somewhat redundant. Furthermore, a significant difference between the conductivities measured in the various environments is necessary to allow the porosity calculation. In this study, comparative conductivity measurements on a PBI char, Specimen DXH-32, in helium and vacuum environments led to a calculated porosity which, when interpreted in consideration of the measured pore-size distribution, could be related to the fraction of the total porosity capable of supporting ordinary helium conduction. However, comparative measurements in argon and vacuum were not sufficiently different to allow a similar calculation.

On the other hand, when the conductivity data allow, calculation of effective porosity presents the possibility of defining the pore fraction capable of supporting ordinary gas conduction with greater accuracy than can be done by means of molecular theory. Also, the calculation provides one check on the theory used to relate the constituent phase conductivities to the net apparent conductivity.

The three-phase model (solid matrix and two sizes of pores) suggested by results of the direct porosity measurements was also used to accomplish the second objective of this study: to investigate the general effect on conductivity of gas-filled voids in porous chars. The two pore phases are distinguished as one containing only pores large enough to support ordinary gas conduction and the other containing the remainder of the total pore volume. Thus, the relative magnitude of the two depends on the physical structure of the material and the mean free path of the gas in the voids.

Of the many theories which have been developed on thermal conductivity in porous media, two (Leob and Maxwell-Eücken) were tailored to this three-phase model. The total porosity was fixed at the value of the DXH-32 char found by direct measurement. The conductivity measurement in an argon atmosphere, representing a heavy gas, presented a point of comparison for the two theories. The Leob theory gave results in agreement with those of the conductivity and pore-size-distribution measurements, whereas the Maxwell-Eücken did not. The Leob theory also correctly predicted a maximum conductivity for a specific ratio of pore/phase fractions in the case of argon-filled pores. For a mixture of helium and argon, whose conductivities were taken as representative of arbitrary light and complex gases, respectively, a minimal increase in apparent conductivity due to the gas was predicted by the Leob theory at a reasonable ratio of two pore/phase fractions.

To summarize, the successful attainment of the objectives set forth for this analysis rests upon the development of a meaningful model for the given material and establishment of an accurate theory relating the measurable apparent conductivity to the conductivities of the constituent phases defined in the model. The amount of experimental data appropriate to this analysis was not extensive enough to allow these objectives to be satisfactorily realized for the PBI-type char studied.

Recommendations

The present analysis of the thermal-conductivity data for DXH-32 made clear the need for a reliable model of the material before thorough interpretation of conductivity data can be accomplished. It is felt that future effort would best be spent in establishing an appropriate theory relating the apparent conductivity to the conductivities of the constituent phases; i. e., modeling studies.

The required experimental program which would produce the necessary data would be based upon a series of specimens of the same base material but with different pore-size distributions. This could be accomplished by using a density-controlling additive such as microballoons in varying proportions in the base material. Hopefully, the total porosity could be kept reasonably constant while the microballoon fraction could be used to vary the large-diameter to small-diameter pore-fraction ratio between specimens. When desired, the microballoons could probably be crushed under an appropriate high-pressure gas to eliminate the possibility of residual gases in the microballoons influencing the conductivity measurements. These specimens, possibly four in number, would be measured in helium, argon, vacuum, and possibly another complex gas representative of a stable pyrolysis gas. Appropriate characterization of the structure similar to that done for DXH-32 would be made. The measurements would be made at temperatures low enough to keep radiation transport across the pores an insignificant fraction of that due to conduction.

The results expected from such a program would be a reliable theory relating the apparent conductivity to that of its constituent phases through measurable material parameters. The model of the material might have the restriction that all experimental specimens would have been basically the same. However, appropriate parameters which might be generalized to other systems would be recognized.

The characterization of the significant phases of the material and the relations between them would allow the calculation of solid-phase conductivity and gas-conduction effects in cases where only certain material parameters may be known, along with the measured apparent conductivity. Removal of the effects of macroscopic pores on the apparent conductivity would allow study of the effects of ablative processes which change the microstructure and chemistry of the dense material, e.g., graphitization.

References

- (1) Gorring, R. L., and Churchill, S. W., "Thermal Conductivity of Heterogeneous Materials", Chemical Engineering Progress, 57, 53-59 (1961).
- (2) Eücken, A., "The Heat Conductivities of Ceramic-Refractory. Calculations of Heat Conductivity From the Constituents", Forsch. Gebiete Ingenieurw., 3 (353), 1-16 (1932).
- (3) Loeb, A. L., "Thermal Conductivity: VIII, A Theory of Thermal Conductivity of Porous Materials", Journal of American Ceramic Society, 37, 96-99 (1954).
- (4) Peterson, J. R., and Bouilla, C. F., "Advances in Thermoproperties at Extreme Temperatures and Pressure", ASME, Third Symposium on Thermophysical Properties, p 264 (1965).
- (5) Schotte, W., "Thermal Conductivity of Packed Beds", AIChE J., 6, 63-67 (1960).
- (6) Woodside, W., and Messmer, J. H., "Thermal Conductivity of Porous Media I. Unconsolidated Sands", Journal of Applied Physics, 32, 1688-1698 (1961).
- (7) Rayleigh, L., "On the Influence of Obstacles Arranged in Rectangular Order Upon the Properties of a Medium", Philosophical Magazine, 34, 481-503 (1892).

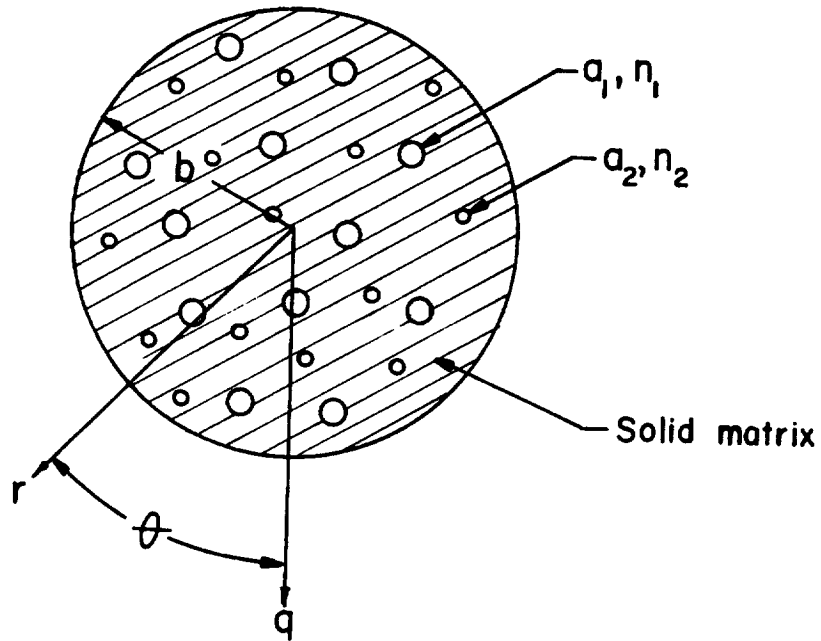


FIGURE B-1. REFERENCE UNIT FOR MAXWELL-EUCKEN EQUATION
(DEFINES SYMBOLS)

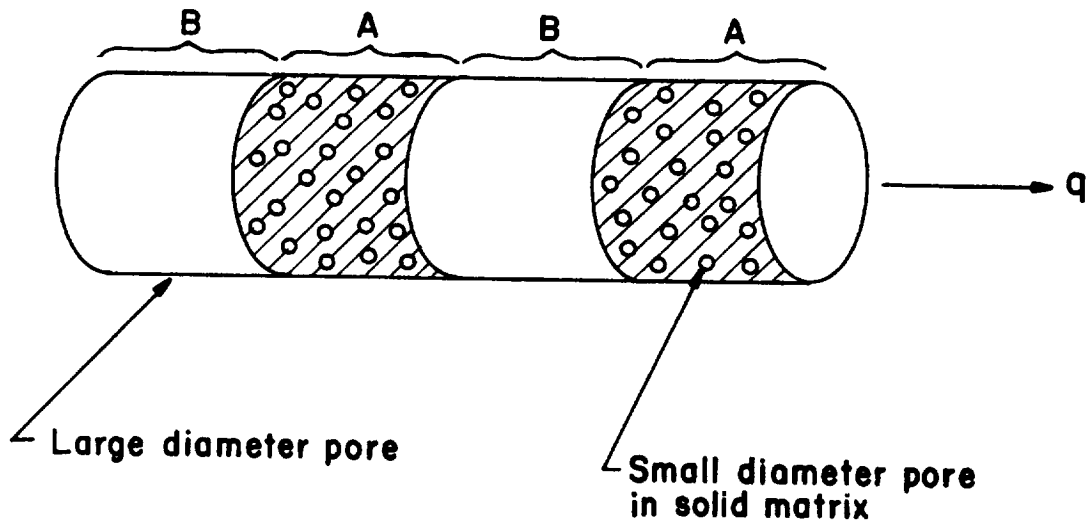


FIGURE B-2. TUBE GEOMETRY FOR LOEB ANALYSIS

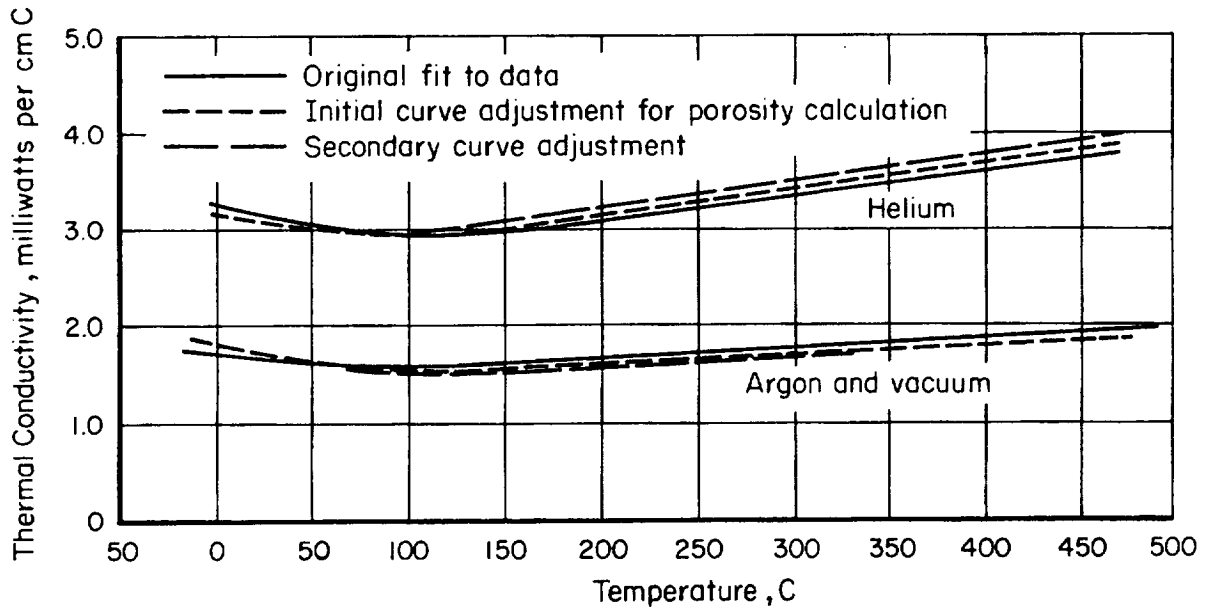


FIGURE B-3. CURVES FOR SPECIMEN DXH-32 USED IN CALCULATION OF SPECIMEN POROSITY FROM THERMAL CONDUCTIVITY MEASUREMENTS IN VACUUM, ARGON, AND HELIUM

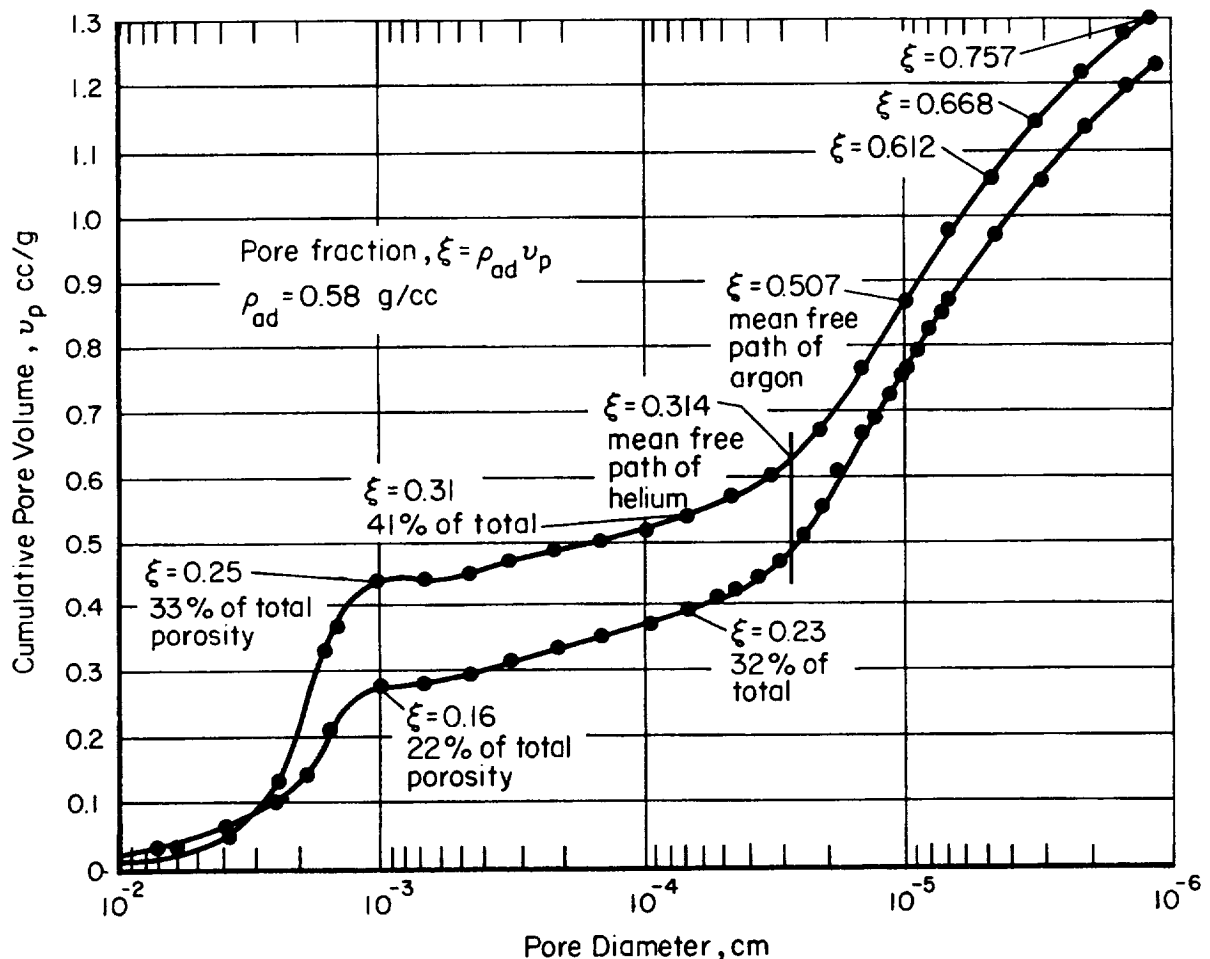


FIGURE B-4. MERCURY POROSIMETER TESTS ON DUPLICATE SAMPLES OF SPECIMEN DXH-32

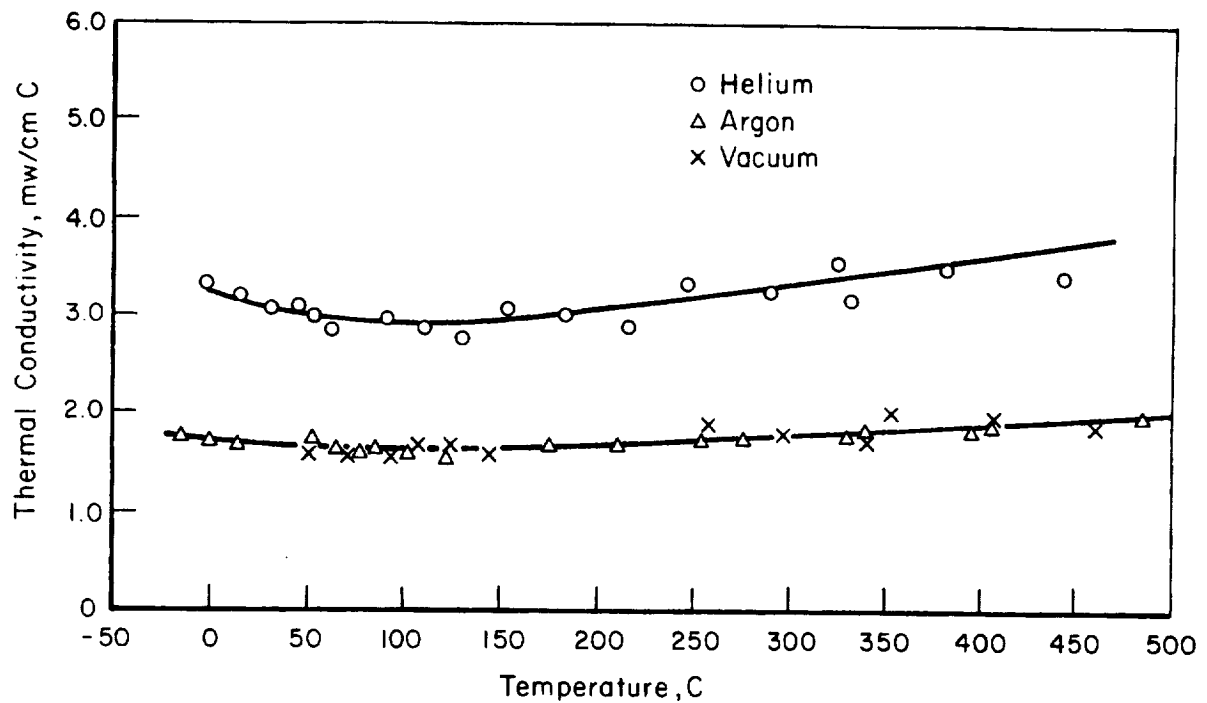


FIGURE B-5. THERMAL CONDUCTIVITY OF SPECIMEN DXH-32

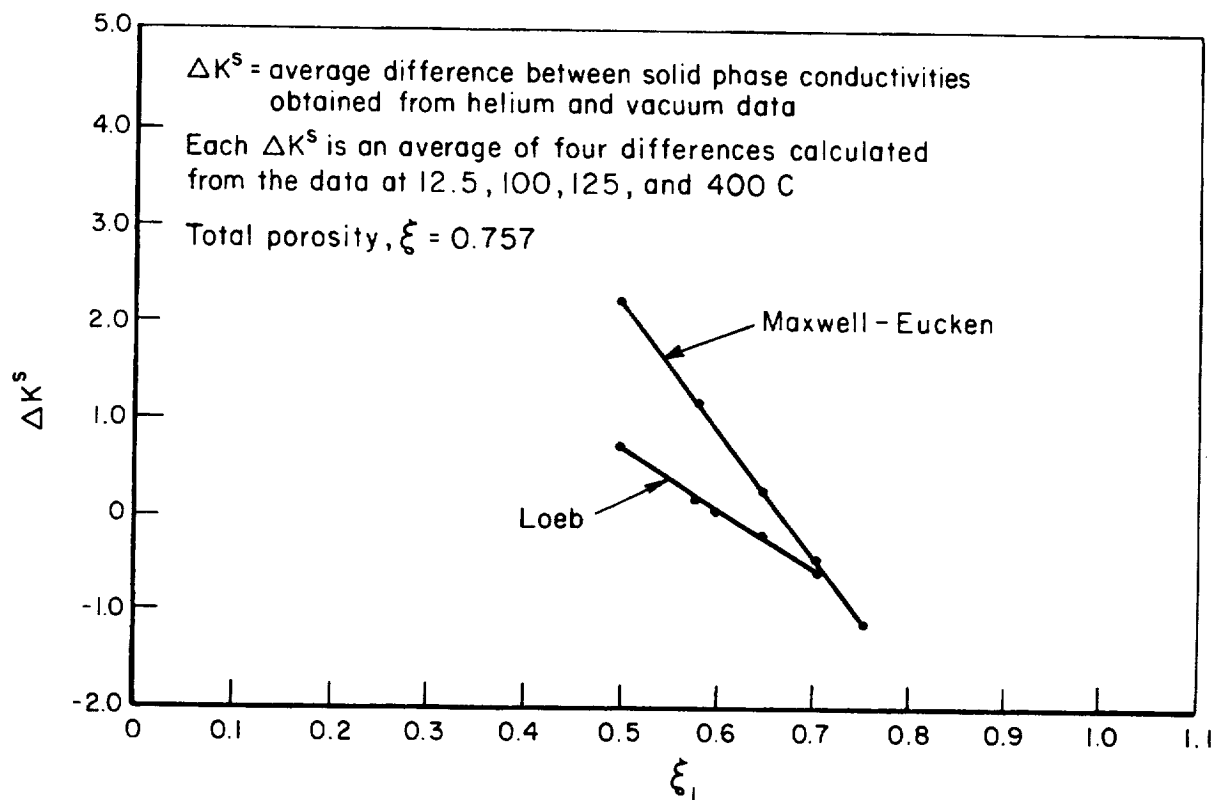


FIGURE B-6. CONVERGENCE OF THE SOLID PHASE CONDUCTIVITIES OBTAINED FROM THERMAL CONDUCTIVITY DATA IN HELIUM AND VACUUM ENVIRONMENTS

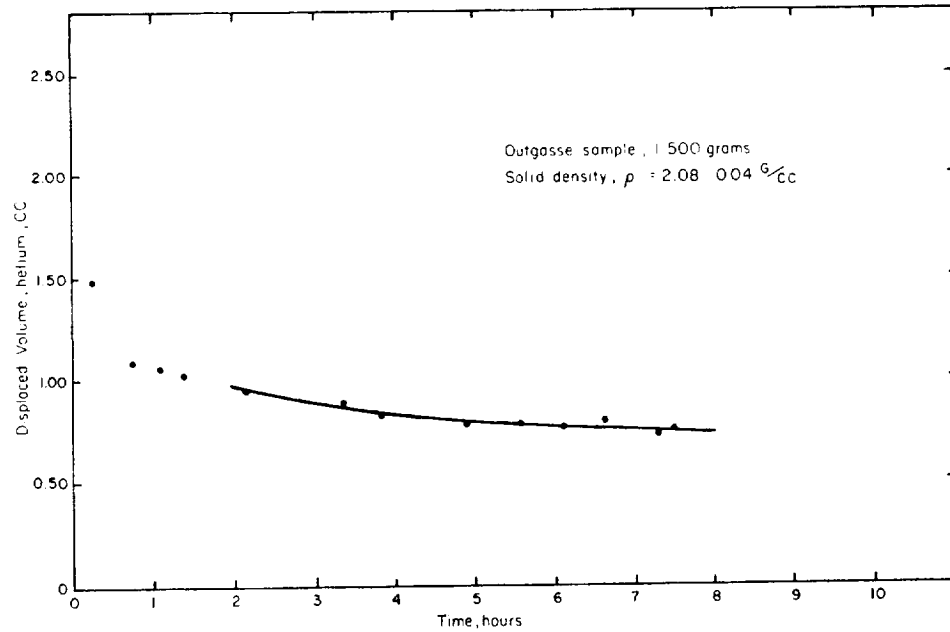


FIGURE B-7. HELIUM DISPLACEMENT MEASUREMENT OF TOTAL POROSITY, SPECIMEN DXH-32

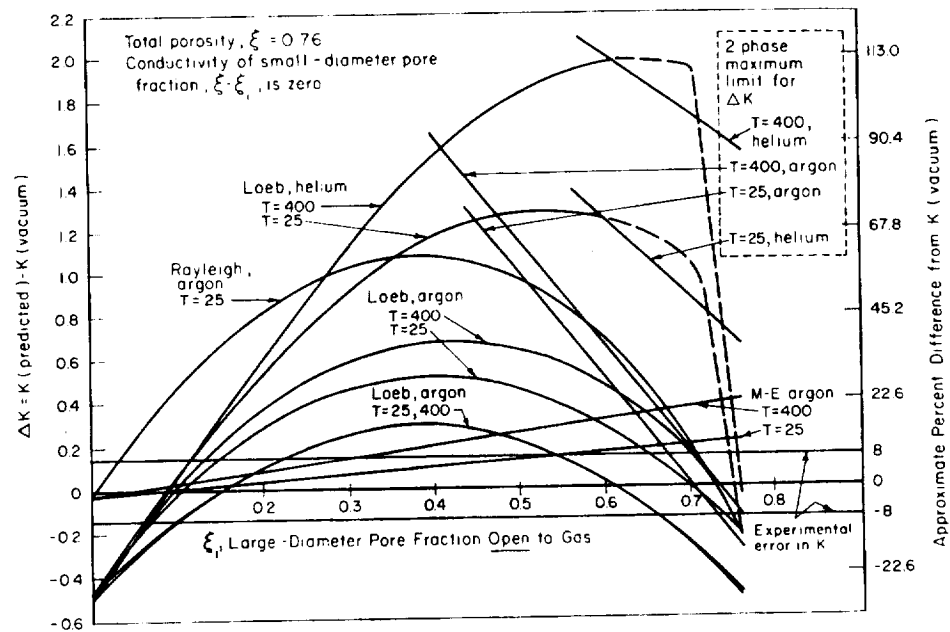


FIGURE B-8. PREDICTED APPARENT CONDUCTIVITIES WITH LARGE-DIAMETER PORE FRACTION FOR MAXWELL-EUCKEN AND LOEB RELATIONS (LARGE-DIAMETER PORES OPEN TO GAS)

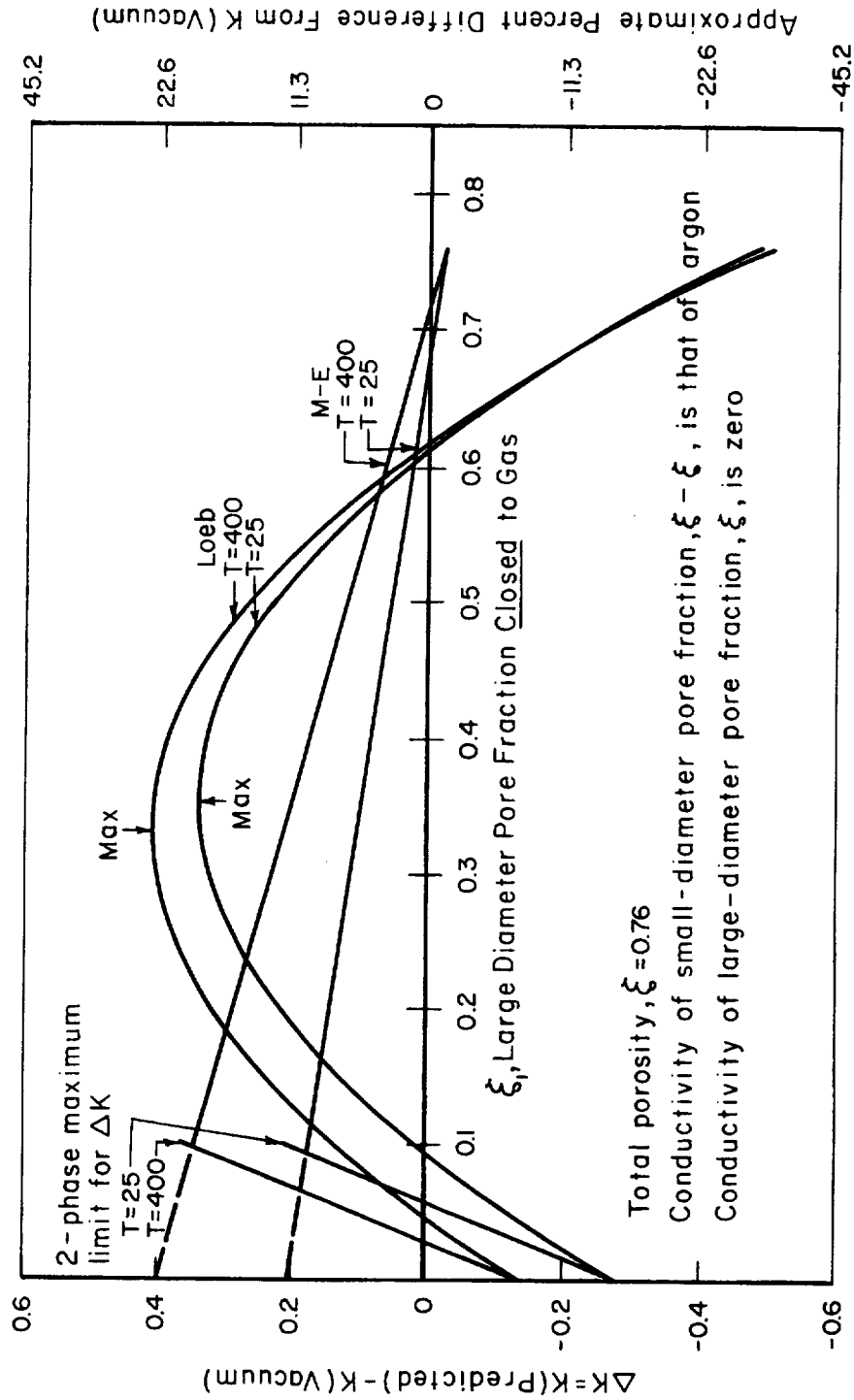


FIGURE B-9. PREDICTED APPARENT CONDUCTIVITIES WITH LARGE-DIAMETER PORE FRACTION FOR MAXWELL-EUCKEN AND LOEB RELATIONS (LARGE-DIAMETER PORES CLOSED TO GAS)

APPENDIX C

ENTHALPY MEASUREMENTS FOR USE IN CALCULATING SPECIFIC HEAT

APPENDIX C

ENTHALPY MEASUREMENTS FOR USE
IN CALCULATING SPECIFIC HEAT

Enthalpy measurements were made using a Bunsen ice calorimeter as described in Appendix E, Apparatus and Methods for Thermophysical Property Measurements.

Specimens were contained in stainless steel capsules for the measurements. The rate of gas evolution and pressure buildup were measured for several of the materials prior to enthalpy measurements. This information was required to prevent reaching unsafe capsule pressures while in the calorimeter furnace. The sealed capsules retained all products of decomposition and the maximum internal capsule pressure was a function of the measuring temperature.

Some materials were measured in vented capsules. These capsules were pre-heated in an external furnace to the temperature of the next calorimeter drop. This permitted the release of decomposition products before each calorimeter drop; hence, the enthalpy of decomposition up to the temperature of measurement was not included in the measured quantity.

Anhydride-Cured Epoxy NovolacsDEN-438DEN-438 + Chopped GlassDEN-438 + Glass Microballons

The specimens were encapsulated in thin-walled Type 347 stainless steel capsules. Drops of the specimen capsule, empty capsule, and NBS-grade Al_2O_3 were made at various temperatures, following the usual technique for operating a Bunsen ice calorimeter.

The capsules, originally sealed by welding, were vented by drilling a small hole through the wall for drops above 248 C to prevent a pressure buildup inside the capsule. The vented specimen capsule was heated in a separate furnace to drive off degradation products that otherwise might be driven off and condensed in the calorimeter furnace. This pretreatment was carried on in a clear, fused-quartz tube so that the capsule could be observed for the release of visible degradation products. It should be remembered that each enthalpy measurement made on the specimen, after it was pretreated in the vented capsule, was made on a chemically different material.

Figure C-1 shows experimental enthalpy-versus-temperature data points and equation-derived curves to fit the data. Enthalpy of the material decreases as some of the polymer is replaced with inert material.

PolybenzimidazolesDXH-31DXH-32, Pyrolyzed at 650 CEXEH-31

Enthalpy and specific-heat measurements on a DXH-31 specimen were made with the specimen encapsulated in a thin-walled, stainless steel capsule. The specimen capsule was not vented to release decomposition products as was necessary with the DEN-438 capsule because the pressure-versus-temperature curve showed negligible pressure at 550 C.

Figure C-2 shows experimental enthalpy-versus-temperature data points and equation-derived curves to fit the data.

Phenolic-Novolac NylonsPNHD-Hughes No. 4PNHD-Hughes No. 5PNLD-LangleyPNHD-Hughes No. 5 Charred at 400 C

Enthalpy measurements were made on the three phenolic-nylon materials (PNLD-Langley, PNHD-Hughes No. 4, and PNHD-Hughes No. 5) in the virgin state. The specimens were sealed in Type 347 stainless steel capsules for measurement in the Bunsen ice calorimeter.

Enthalpy values were determined initially between 0 C and 500 C. It became obvious from these data, however, that there was a discontinuity in the enthalpy-temperature curve between 250 and 375 C for all three materials. Additional enthalpy measurements on the same encapsulated specimens were made between 500 C and 50 C to investigate this region.

Figures C-3, C-4, and C-5 show the enthalpy-temperature relation for these three virgin materials. It is obvious that a nonreversible change occurred at some temperature above about 250 C in each case. Opening of the capsules revealed that the specimens were extensively pyrolyzed. Because of this, and the fact that pyrolysis apparently begins near 250 C, the enthalpy data recorded after the materials had exceeded this temperature should not be considered representative of virgin material, but rather of the products resulting from the 500 C exposure.

Figure C-6 shows the enthalpy relation for Specimen PNHD-Hughes No. 5 pre-charred at 400 C.

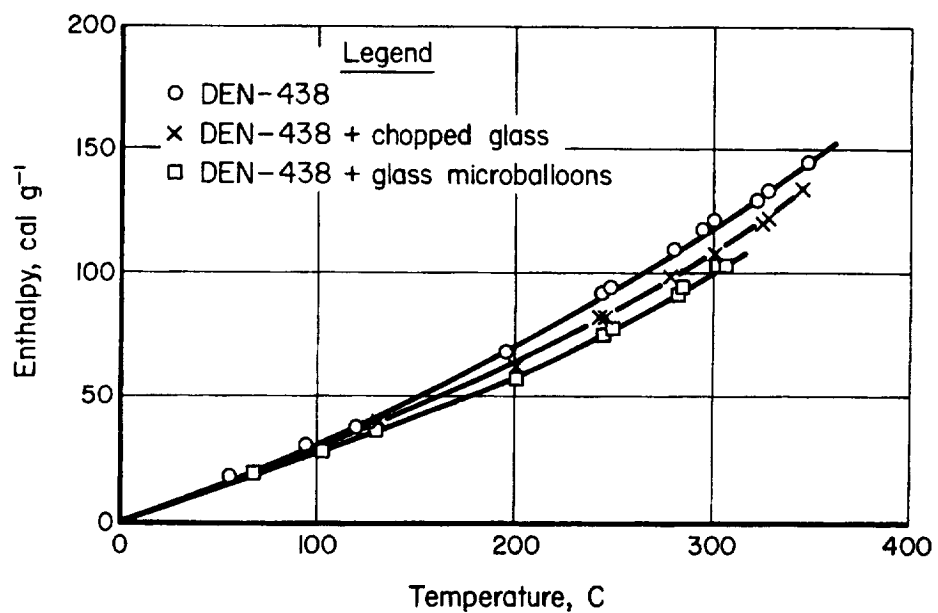


FIGURE C-1. ENTHALPIES OF ANHYDRIDE-CURED EPOXY-NOVOLAC MATERIALS

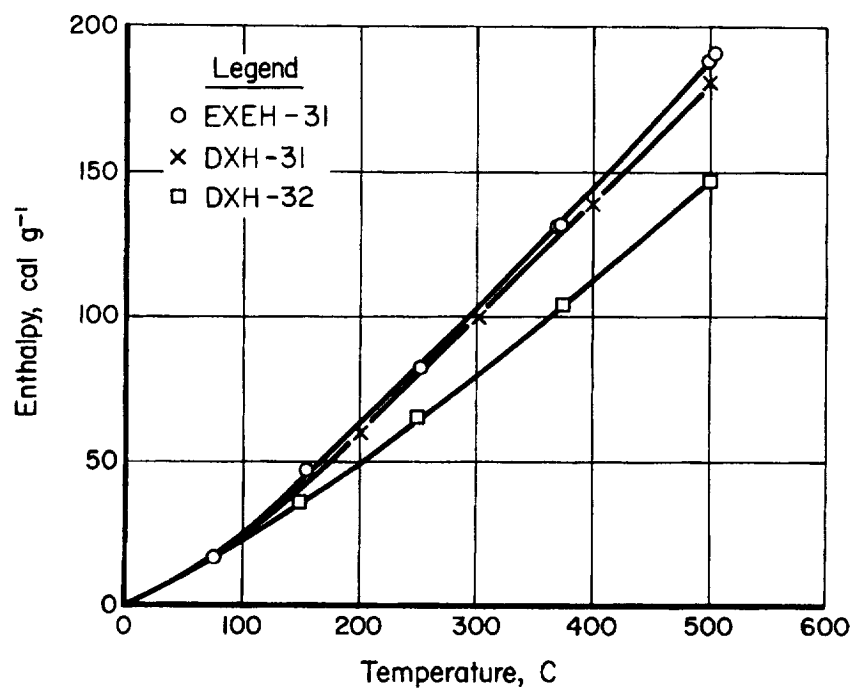


FIGURE C-2. ENTHALPIES OF POLYBENZIMIDAZOLE MATERIALS

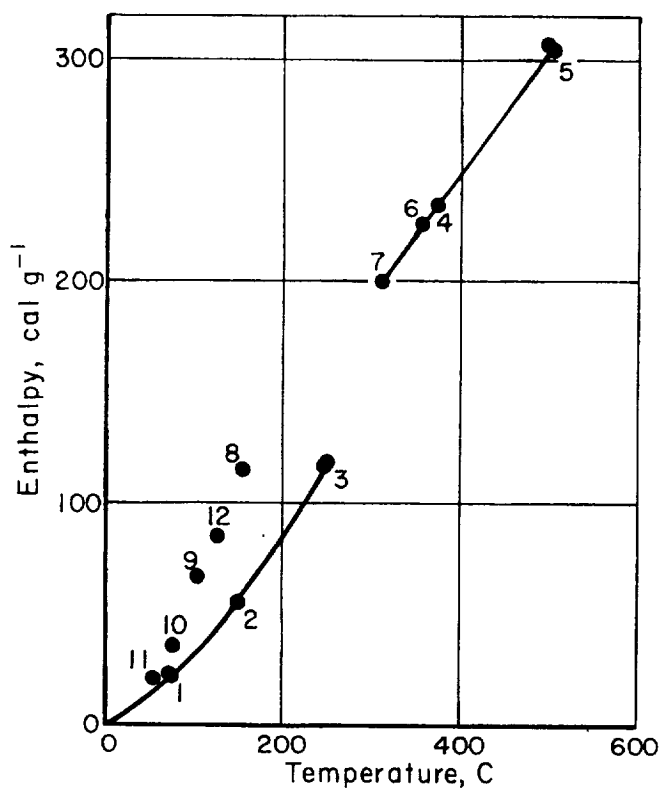


FIGURE C-3. ENTHALPY OF PNHD-HUGHES NO. 4 MATERIAL

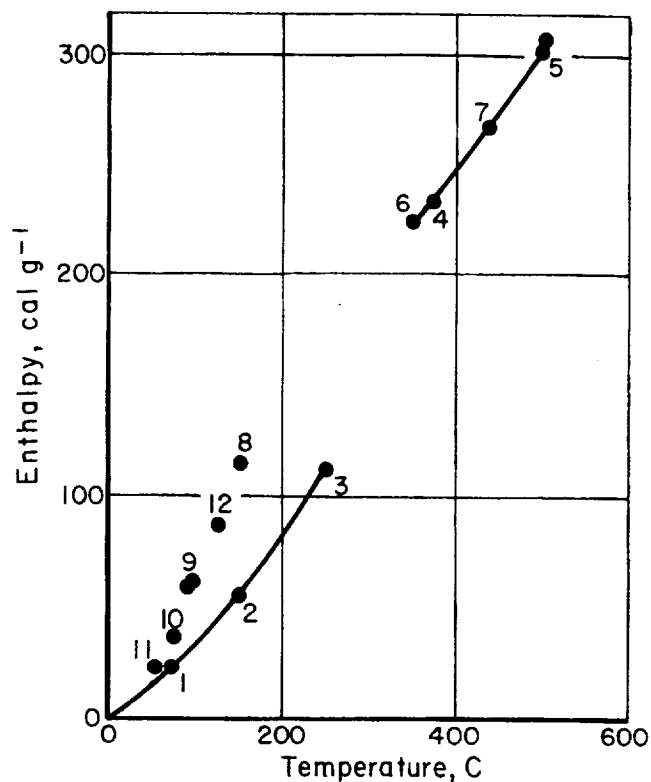


FIGURE C-4. ENTHALPY OF PNHD-HUGHES NO. 5 MATERIAL

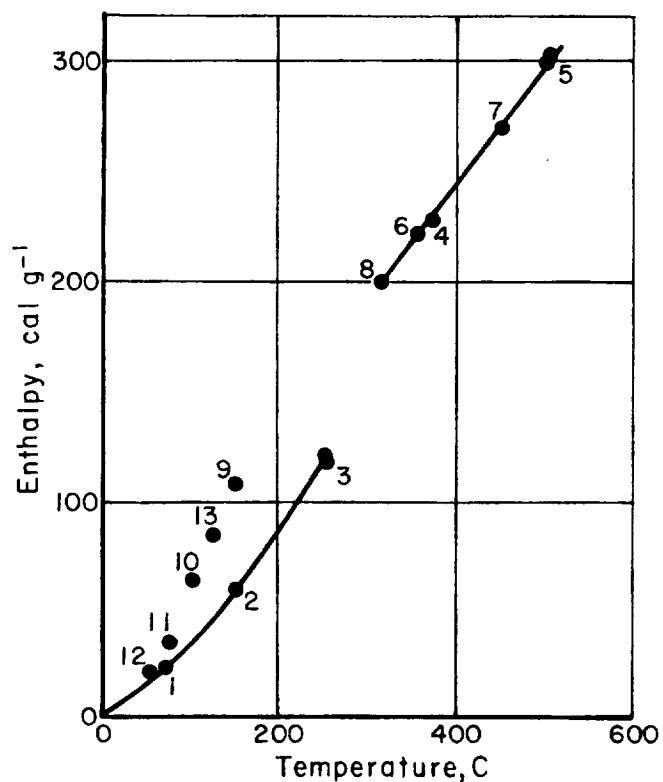


FIGURE C-5. ENTHALPY OF PNLD-LANGLEY MATERIAL

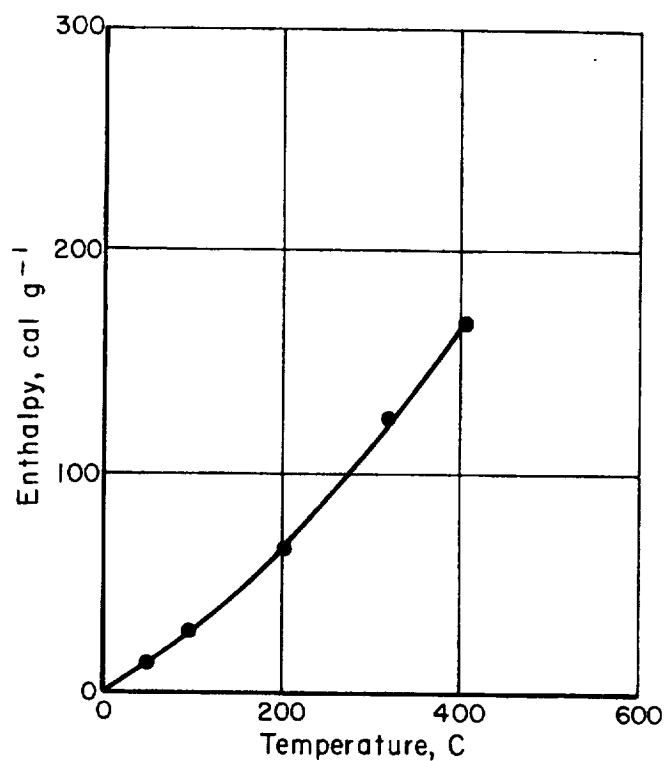


FIGURE C-6. ENTHALPY OF PYROLYZED (400 C) PNHD-HUGHES NO. 5 MATERIAL

APPENDIX D

LINEAR-THERMAL-EXPANSION MEASUREMENTS

APPENDIX D

LINEAR-THERMAL-EXPANSION MEASUREMENTS

Linear-thermal-expansion measurements were made using a clear-fused-quartz-structured manual dilatometer, as described in Appendix E. The specimens were cylinders nominally 3/8 inch in diameter and 3 inches long. The specimens were under a compressive load of about 6 psi during the measurements from the weight of the pushrod and the spring loading from the dial indicator.

Anhydride Cured Epoxy Novolacs

Preliminary expansion measurements were made on a specimen of DEN-438 in an air atmosphere.

The temperature of the specimen was measured by a small Chromel-Alumel thermocouple imbedded in a small hole in the specimen at its longitudinal center. The output of the thermocouple (with an ice-bath cold junction) was measured with a semiprecision potentiometer. The temperature of the system was regulated by manual adjustment of an autotransformer controlling the input power to the electric heater. The dial indicator, used to measure dilation, was graduated in 0.001-inch divisions with a 1-inch travel.

During the operation, the furnace was heated at a rate of approximately 3-1/2 C/min. At 1 to 5-minute intervals, depending on the rate of change, the temperature and the dial indicator reading were observed and recorded. The measurement was made in air, although the specimen had been stored in a desiccator filled with dry nitrogen until approximately 1 hour before the operation was begun. The annular space between the quartz tube and the push rod was open to room air to allow release of gaseous decomposition products.

After the run was completed and the apparatus was disassembled, the specimen was observed to have undergone severe degradation. The push-rod guide tube, which extended approximately halfway down the specimen, was firmly cemented to the specimen by viscous decomposition products. This tube was broken away from the specimen. During this operation, the specimen broke transversely. The surface of the specimen appeared gnarled and contained several deep cracks. The top of the specimen had been indented by the push rod and the bottom had conformed to the convex surface of the quartz tube. The distortion of the specimen ends prevented any posttest length measurements and showed that the results of the dilation measurements could not be used as precise length changes.

Table D-1 shows the change in specimen weight from time of receiving until operation.

TABLE D-1. SPECIMEN WEIGHT

Date	Weight, grams
3-22-65	6.7067
3-24-65	6.7033
3-28-65	6.7010
4-6-65	6.6999
6-30-65	6.6941
Posttest	4.9618

There was a drastic change in specimen length during the run. From room temperature to approximately 300 C, a rather normal expansion occurred. From 300 to 350 C an inflection in the curve shows a transition where it appears specimen degradation began to affect the normal thermal expansion. At approximately 350 C, the degradation was accompanied by a rapid specimen contraction which continued through the heating period to 400 C and until the specimen had cooled to approximately 350 C. When cooled to approximately 300 C, the rate of length change resumed a rate similar to the initial rate during heating.

Another specimen of DEN-438, along with specimens of DEN-438 + chopped glass and DEN-438 + glass microballoons, was measured in an argon atmosphere. Figure D-1 shows the results of the measurements.

Polybenzimidazoles

Measurements of linear thermal expansion versus temperature were made on the following polybenzimidazole specimens:

DXH-30

DXH-31

DXH-32

EXEH-31.

The specimens had been stored in dry nitrogen in a desiccator. Figure D-2 shows the relations of linear thermal expansion to temperature for the four polybenzimidazole specimens measured.

The curves show normal expansion on heating to 100 C, whereupon it appears that the release of water from the material caused a contraction. Following this, expansion proceeded to about 400 C. Contraction on cooling is normal.

Good dimensional stability is evident in the PBI materials, as represented by the DXH specimens. After the loss of water below 200 C, expansion amounted to only a few tenths of 1 percent, and the contraction was small compared with that of other polymeric materials, even though the temperature was raised to 550 C.

Specimen DXH-32 has a very low expansion. This value was checked by measuring a duplicate specimen of the same material. This material did not deteriorate to any noticeable degree.

The linear thermal expansion of the EXEH-31 was greater than that of the DXH materials. The change in slope near 100 C is similar to that observed with the DXH-31, and has been attributed to loss of moisture. At 400 C the specimen began to shorten, apparently as a result of decomposition effects. After the run the specimen was discolored but gave no indication of having been softened during the experiment.

Phenolic-Novolac Nylons

Measurements of linear thermal expansion versus temperature were made on the following phenolic-novolac nylon materials:

PNHD-Hughes No. 4
PNHD-Hughes No. 5
PNLD-Langley
PNHD-Hughes No. 5
precharred at 400 C.

Measurements were made first on the PNHD materials.

The data for the Hughes No. 4 and No. 5 specimens are presented in Figure D-3. Values above 250 C were not considered representative of the virgin state of these materials, as decomposition began at this point. Data for the PNLD-Langley and pyrolyzed PNHD-Hughes No. 5 specimen are shown in Figure D-4. As would be expected, the pyrolyzed material was very stable as compared with the virgin materials. The expansion at 400 C was 1.32 percent, the same value reached by the virgin material at about 290 C.

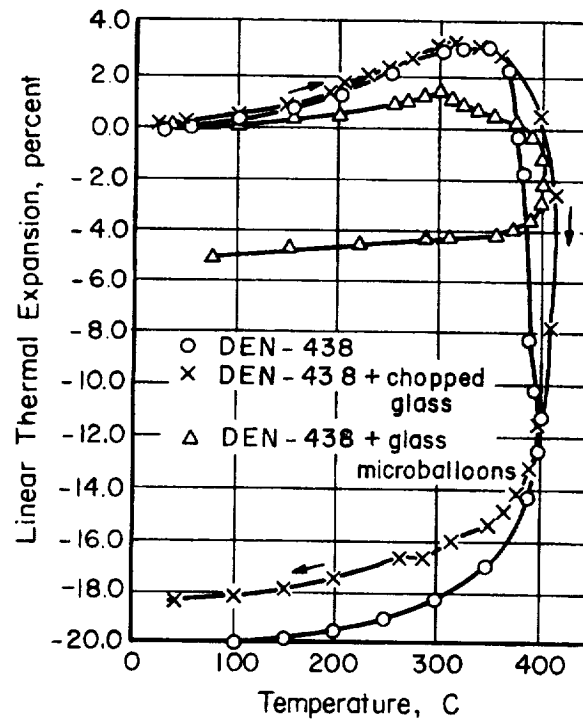


FIGURE D-1. LINEAR-THERMAL-EXPANSION CURVES FOR ANHYDRIDE-CURED EPOXY-NOVOLAC MATERIALS

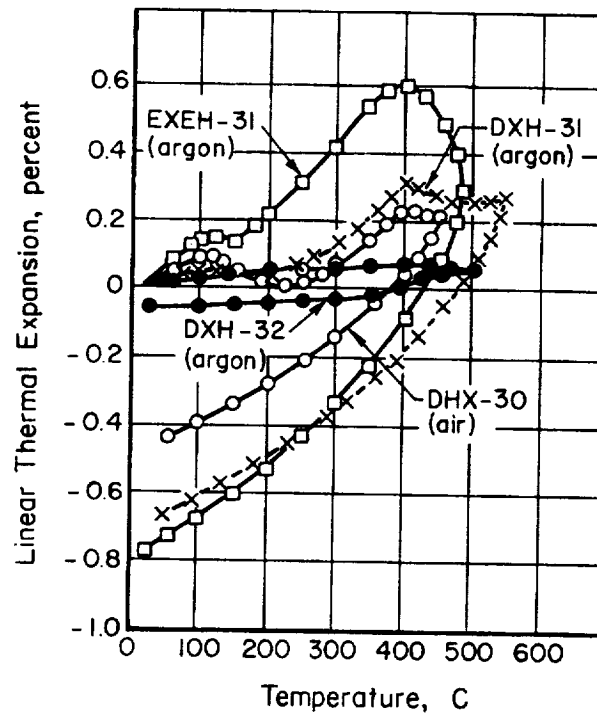


FIGURE D-2. LINEAR-THERMAL-EXPANSION CURVES FOR POLYBENZIMIDAZOLE MATERIALS

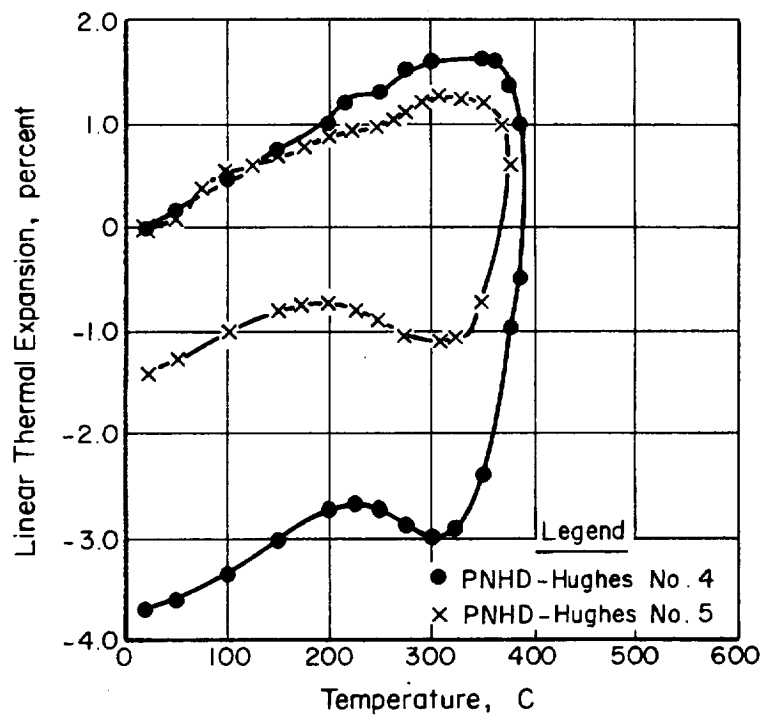


FIGURE D-3. LINEAR-THERMAL-EXPANSION CURVES FOR PNHD-HUGHES NO. 4 AND NO. 5 MATERIALS

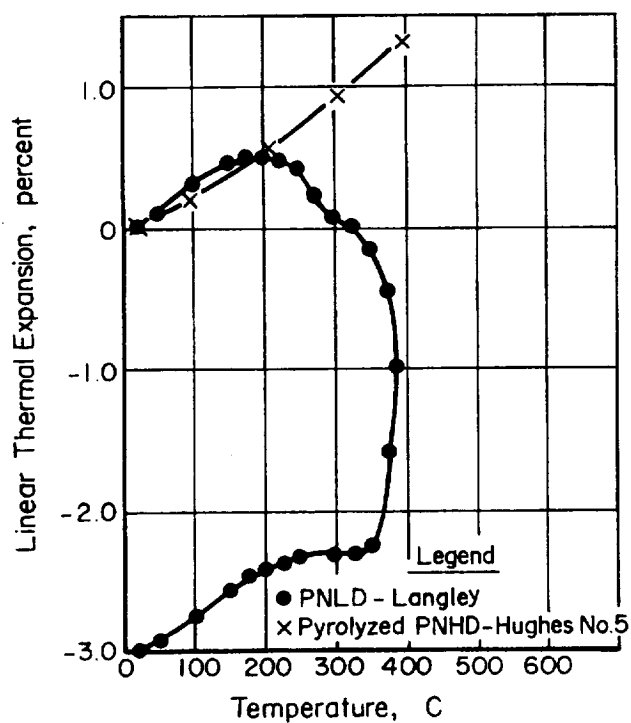


FIGURE D-4. LINEAR-THERMAL-EXPANSION CURVES FOR PNLD-LANGLEY AND PYROLYZED PNHD-HUGHES NO. 5 MATERIALS

APPENDIX E

APPARATUS AND METHODS FOR MAKING THERMOPHYSICAL- PROPERTY MEASUREMENTS

APPENDIX E

APPARATUS AND METHODS FOR MAKING THERMOPHYSICAL
PROPERTY MEASUREMENTSThermal-Conductivity Apparatus

Thermal-conductivity measurements on the polymer materials in this program were made in a self-guarding disk-type apparatus.

Figure E-1 is a schematic drawing of this apparatus. The disk-shaped specimen is nominally 3 inches in diameter and 1/2 inch thick. Three thermocouples are placed in the specimen. One is placed in a radial hole near the center of the specimen, and the other two are cemented, one on each surface, into shallow diametral grooves with the beads near the axis of the specimen. With three thermocouples in the specimen, each thermal equilibrium gives two thermal-conductivity values, each at a different mean specimen temperature.

During operation of the apparatus, a resistance heater imbedded in a heater block introduces a downward heat flow through the specimen. A radiation-type heater (not shown in Figure E-1) is used for higher specimen temperatures. The quantity of heat flow through the specimen is measured by a cylindrical heat-flow meter or reference material surrounded by three concentric guard cylinders of the same material. Battelle uses calibrated Armco iron, Type 347 stainless steel, or Pyroceram, for reference materials when making comparative, steady-state, longitudinal-heat-flow, thermal-conductivity measurements. The self-guarding feature of the specimen/heat-flow meter/guard-cylinder assembly should be noted. The heat-flow meter measures only the heat passing through the specimen over an area equal to that of the heat-flow meter, plus half the area of the annular space between the heat-flow meter and the first guard cylinder. The heat passing through the specimen outside this measuring area flows down through the guard cylinders and is not measured. Any heat lost from the edge of the specimen does not enter into the calculations and does not introduce an error into the results.

Past experience has shown that it is impossible to have low-resistance, uniform, thermal contact between the specimen and the heat-flow meter/guard-cylinder assembly. To overcome this difficulty, Battelle uses a resilient layer of carbon wool or similar material between the specimen and the heat-flow meter/guard-cylinder assembly to make a uniform thermal contact. This procedure, although not ideal, yields a reasonably good thermal contact, but, more importantly, it yields a uniform contact.

The heat sink is cooled by gas or liquid flow and serves to take the heat introduced into the specimen out of the system. The apparatus is enclosed in a vacuum or atmosphere shell with a vacuum connection. Thermal-radiation or -convection shielding is used as needed.

The error in thermal-conductivity measurements made with the apparatus is usually estimated not to exceed ± 5 percent, the chief source of possible error being the thermal conductivity of the reference material. Comparative errors of two materials measured using the same reference material are usually estimated not to exceed ± 2 percent.

Enthalpy Apparatus

Enthalpy measurements on the polymer specimens were made in a Bunsen ice calorimeter of the type described by Ginnings and Corruccini(E-1). In this instrument, heat from a specimen melts ice that is in equilibrium with water in a closed system. The resulting volume change of the ice-water system is determined by weighing mercury (in contact with the water) displaced as the system expands and contracts. The ratio of heat input to the mass of mercury displaced is a constant for the apparatus. There is no temperature change in the calorimeter during specimen cooling because all heat transfer occurs at the ice point.

Figure E-2 shows schematically the calorimeter used for this program, which is described in greater detail by Deem and Lucks(E-2). As the previously heated, encapsulated specimen (L) is dropped into the central chamber of a double-wall stainless steel vessel, it gives up heat to the ice-covered finned section (J) which is enclosed in water in equilibrium. The portion of heat given up by the specimen only is determined by subtracting from the total that contribution made by the capsule. This latter amount is evaluated by a separate drop of an empty capsule. As the ice melts, mercury from the reservoir (B) and, in turn, from an external accounting system enters the inner vessel through Tube C to make up the volume difference of ice melting to water. The total volume of mercury displaced while the specimen cools from its drop temperature to the ice point is measured accurately by this system, and, by weight, related to the heat quantity transferred. This relationship was measured by Ginnings, et al.(E-3-E-5) and by Battelle to be 270.48 J/g of mercury. Frequent checks of the calorimeter operation, using NBS-calibrated Al_2O_3 as the specimen standard, demonstrated that the error of enthalpy measurements is less than ± 1 percent.

Linear-Thermal-Expansion Apparatus

Linear-thermal-expansion measurements of the polymer materials were made in a manual dilatometer. Figure E-3 is a schematic of this apparatus. The cylindrical specimen, with thermocouple attached, is centered in a quartz tube inside the furnace. A quartz push rod transmits specimen expansion or contraction to a dial-indicator gage.

During operation the furnace was heated at a rate of approximately 3.5 C/min. At 1 to 5-minute intervals, depending on the rate of length change, the temperature and the dial-indicator reading were observed and recorded. Measurements were made in air and in argon. The annular space between the quartz tube and the push rod was open to allow release of gaseous decomposition products.

Thermal Diffusivity Apparatus

Thermal-diffusivity measurements were made by the flash-diffusivity technique using the apparatus shown in Figure E-4. A thin disk-shaped specimen is held in a compatible holder inside a folded-tube tantalum furnace. The specimen and furnace are protected by either a vacuum or an atmosphere of inert gas. Specimen temperatures are measured using a thermocouple with the bead placed near the specimen.

For the measurement, the front face of the specimen is heated with a short-duration pulse from the laser. As the heat pulse travels through the specimen, its back-face temperature rise is recorded as a function of time by means of the infrared detector-oscilloscope-camera system. The thermal diffusivity is calculated on the basis of this time function.

REFERENCES

- E-1. Ginnings, D. C., and Corruccini, R. J., "An Improved Calorimeter - The Determination of Its Calibration Factor and Density of Ice at 0 C", J. Res. Natl. Bur. Stds., 38, 583-591 (1947).
- E-2. Deem, H. W., and Lucks, C. F., "An Improved All-Metal Bunsen-Type Ice Calorimeter", Instr. Soc. Am., PPT-4, 1-9 (1958).
- E-3. Ginnings, D. C., Douglas, T. B., and Ball, A. F., "Heat Capacity of Sodium Between 0 and 900 C, The Triple Point and Heat of Fusion", J. Res. Natl. Bur. Stds., RP 2110, 45, 23-33 (1950).
- E-4. Ginnings, D. C., and Corruccini, R. J., "Enthalpy, Specific Heat, and Entropy of Aluminum Oxide From 0 to 900 C", J. Res. Natl. Bur. Stds., RP 1797, 38, 593-600 (1947).
- E-5. Ginnings, D. C., and Furukawa, G. T., "Heat Capacity Standards for the Range 14 to 1200 K", J. Am. Chem. Soc., 75, 525 (1953).

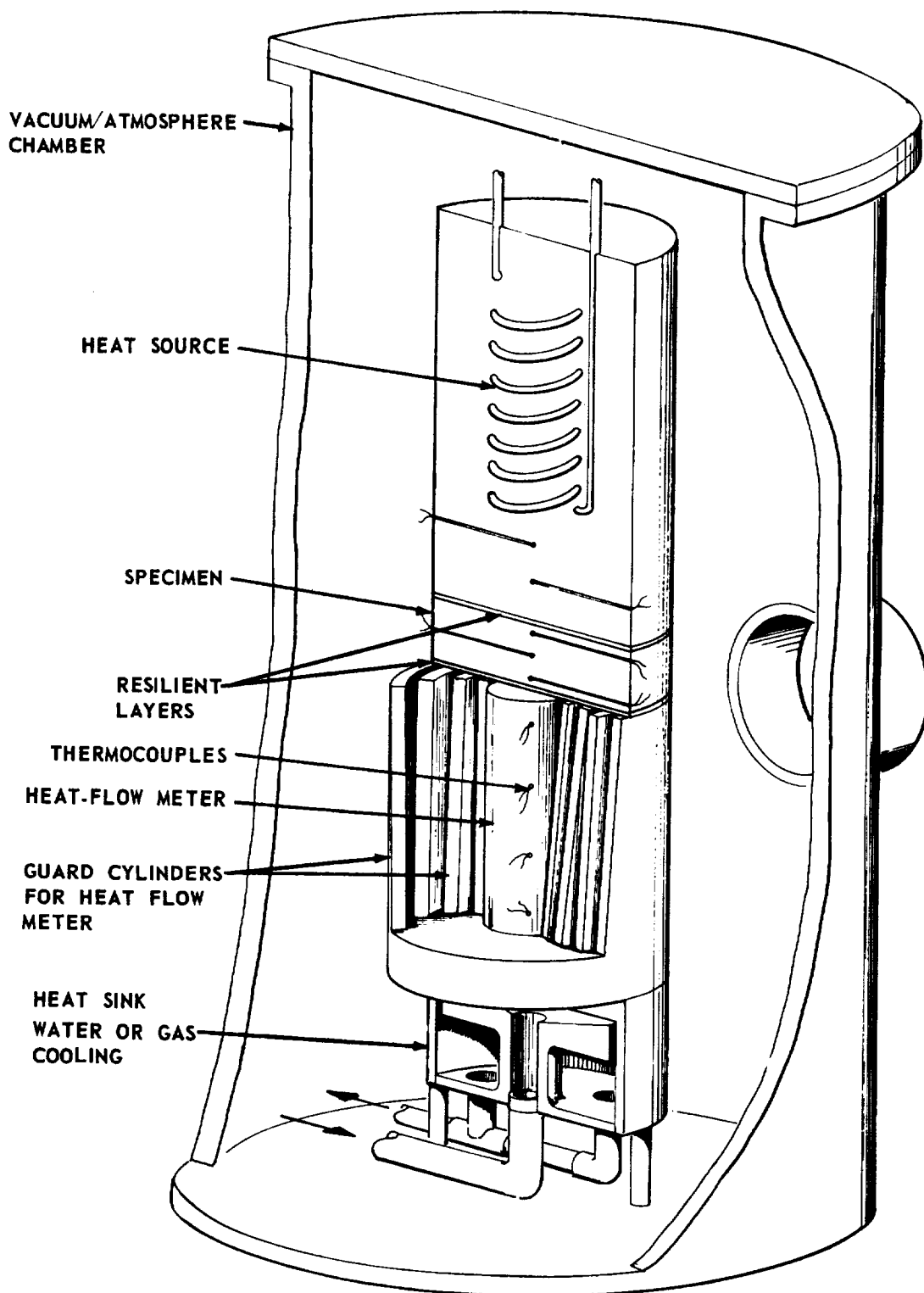


FIGURE E-1. SELF-GUARDING DISK APPARATUS FOR THERMAL-CONDUCTIVITY MEASUREMENTS

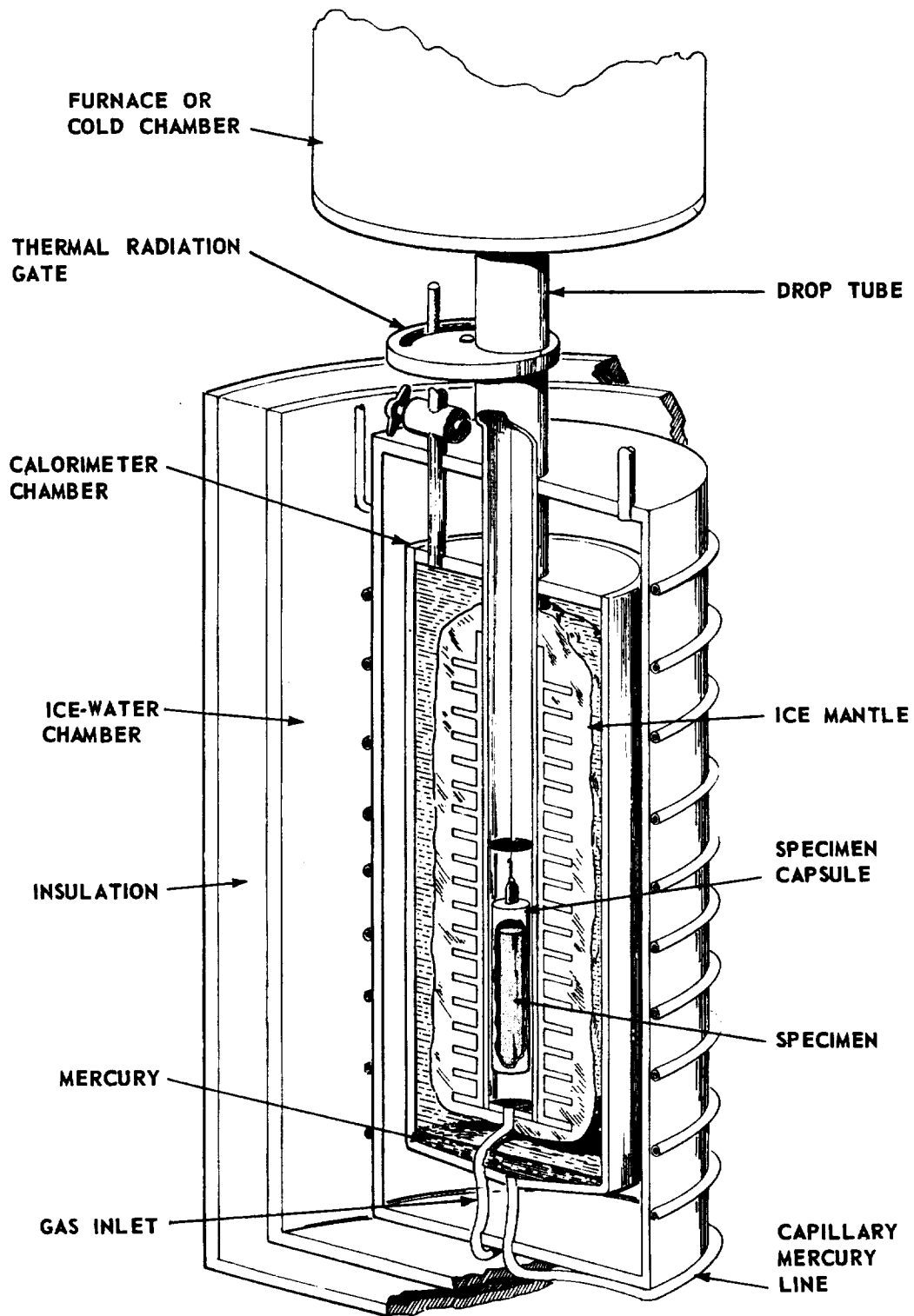


FIGURE E-2. STAINLESS STEEL BUNSEN
ICE CALORIMETER

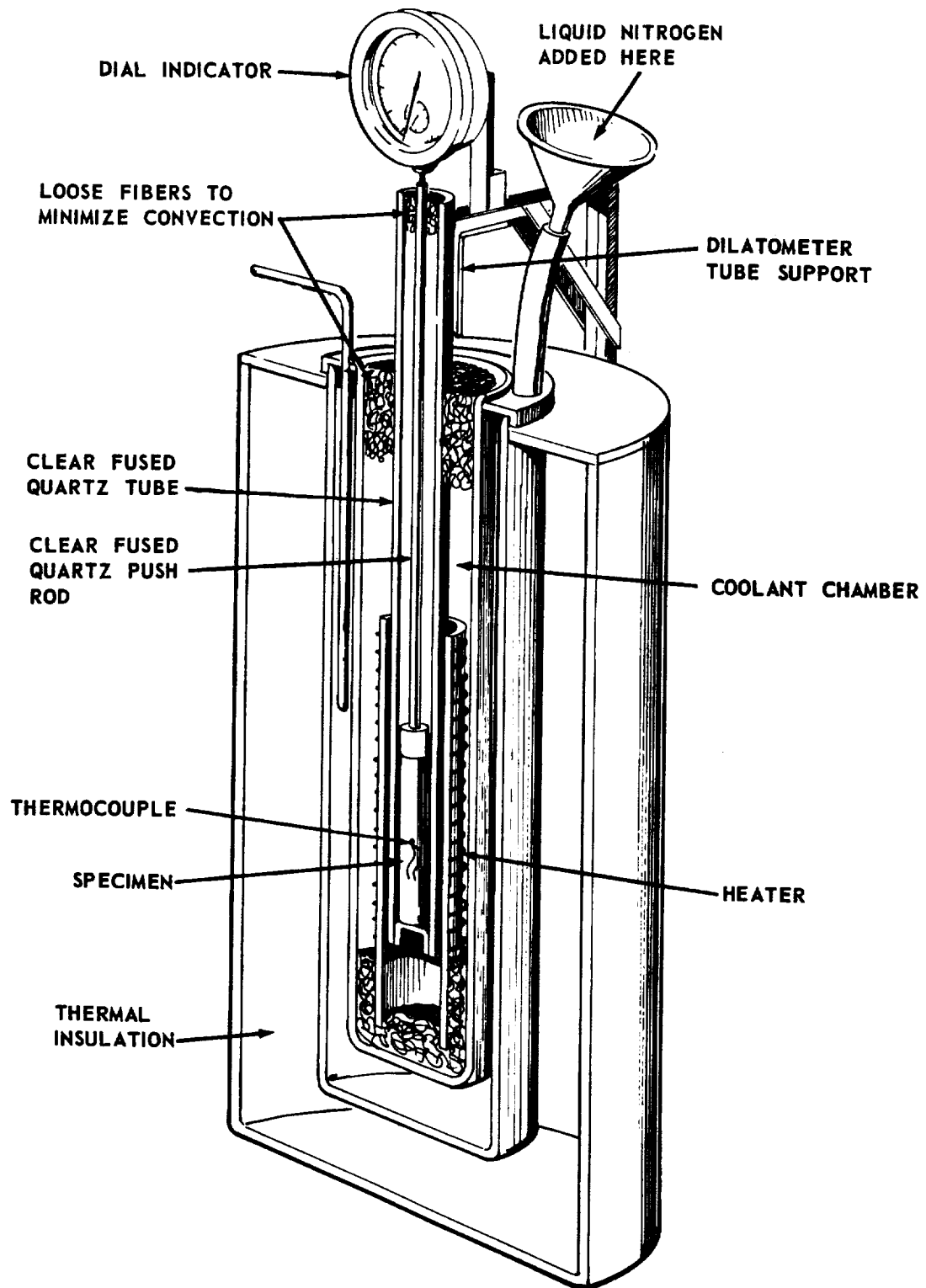


FIGURE E-3. MANUAL DILATOMETER

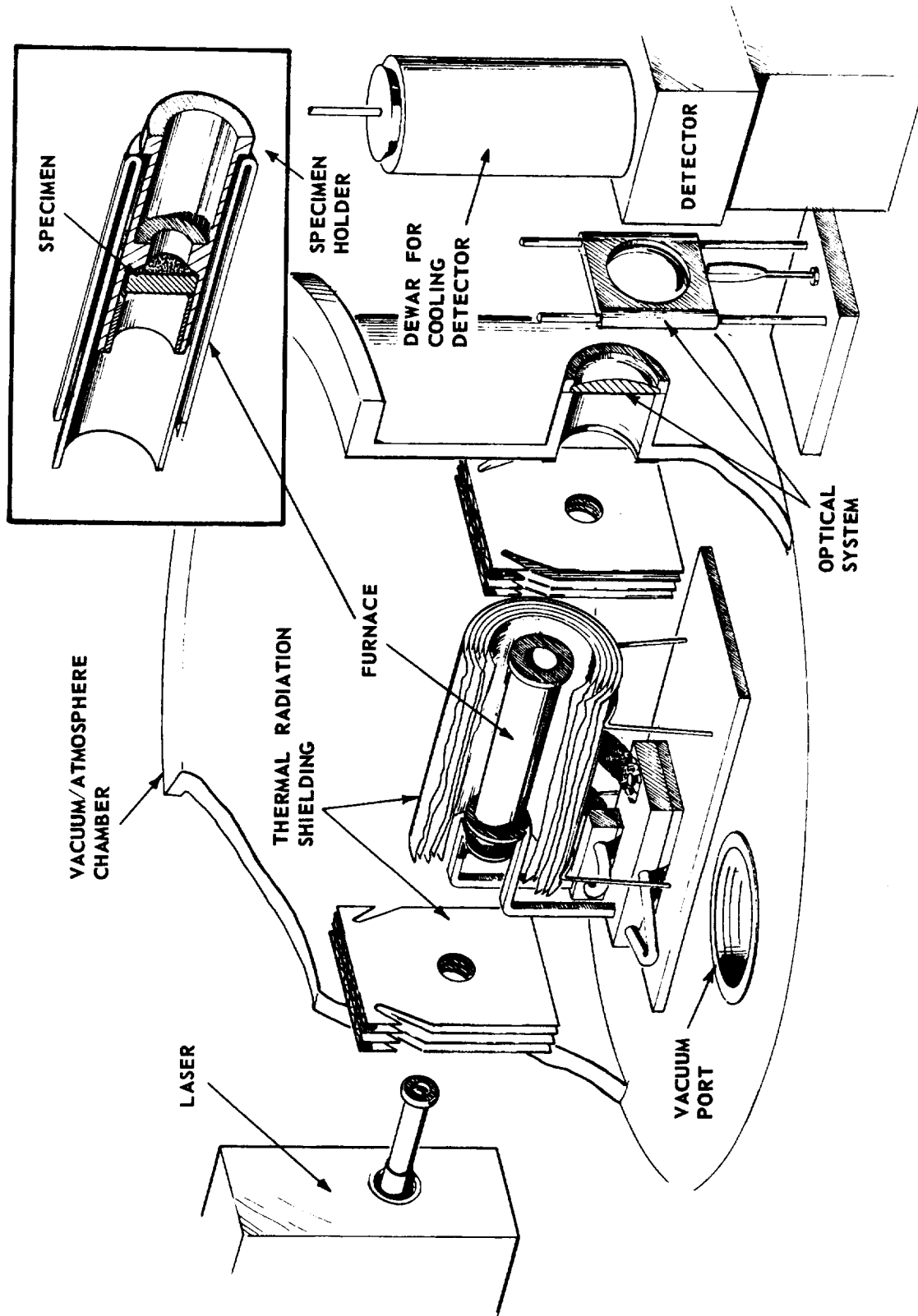


FIGURE E-4. THERMAL DIFFUSIVITY APPARATUS

